Networks of Izhikevich Neurons
Synchronization and Network Inference

IFT - UNESP
INSTITUTO DE FÍSICA TEÓRICA

Raul de Palma Aristides

IFT-T.001/2024

Aristides, Raul de Palma
A715n Networks of Izhikevich neurons: synchronization and network inference / Raul de Palma Aristides. – São Paulo, 2024
105 f.: il.

Tese (doutorado) – Universidade Estadual Paulista (Unesp), Instituto de Física Teórica (IFT), São Paulo
Orientador: Hilda Alicia Cerdeira

1. Sistemas não lineares. 2. Sincronização. 3. Análise de séries temporais. I. Título

Sistema de geração automática de fichas catalográficas da Unesp. Biblioteca do Instituto de Física Teórica (IFT), São Paulo. Dados fornecidos pelo autor(a).

NETWORKS OF IZHIKEVICH NEURONS SYNCHRONIZATION AND NETWORK INFERENCE

Tese de Doutorado apresentada ao Instituto de Física Teórica do Câmpus de São Paulo, da Universidade Estadual Paulista "Júlio de Mesquita Filho", como parte dos requisitos para obtenção do título de Doutor em Física, Especialidade Física Teórica.

Comissão Examinadora:

Profa. Dra. HILDA ALICIA CERDEIRA (Orientadora)
Instituto de Física Teórica/UNESP

Profa. Dra. ANA AMADOR
Universidad de Buenos Aires & CONICET

Prof. Dr. ANTONIO MARCOS BATISTA
UEPG/Universidade Estadual de Ponta Grossa

Prof. Dr. ANTONIO CARLOS ROQUE
FFCLRP/Universidade de São Paulo

Prof. Dr. NICOLAS RUBIDO
School of Natural and Computing Sciences /University of Aberdeen

Conceito: Aprovado

São Paulo, 30 de janeiro de 2024.

Networks of Izhikevich Neurons
Synchronization and Network Inference

Networks of Izhikevich Neurons
Synchronization and Network Inference

This thesis has received financial support from CAPES (Brasil)

Networks of Izhikevich Neurons
Synchronization and Network Inference

THESIS

submitted to the Institute of Theoretical Physics
São Paulo State University, Brazil

as a partial fulfillment of the requirements for the degree of

Doctor of Science

January 30th 2024

Raul de Palma Aristides

Hilda Alicia Cerdeira (supervisor)

Examination Committee

Titulars:
Prof. Dr. Hilda Alicia Cerdeira (Supervisor)
Instituto de Física Teórica, Universidade Estadual de São Paulo

Prof. Dr. Ana Amador
Departamento de Física, Universidad de Buenos Aires & CONICET

Prof. Dr. Antonio Marcos Batista
Departamento de Física, Universidade Estadual de Ponta Grossa

Prof. Dr. Antonio Carlos Roque
Faculdade de Filosofia, Ciências e Letras de Ribeirão Preto,
Universidade de São Paulo

Prof. Dr. Nicolas Rubido
School of Natural and Computing Sciences, University of Aberdeen

Substitutes:
Prof. Dr. Antonio Pons
Departament de Física, Universidad Politécnica de Cataluña · Barcelona Tech

Prof. Dr. Johann H. Martínez
Departamento de Análisis Matemático y Matemática Aplicada ,
Universidad Complutense de Madrid

Prof. Dr. Roberto Kraenkel
Instituto de Física Teórica, Universidade Estadual de São Paulo

Instituto de Física Teórica - UNESP
R. Dr. Bento Teobaldo Ferraz 271, Bloco II
01140-070 São Paulo, Brasil

“ ¿Qué duda cabe que el mundo que conocemos es el resultado del reflejo de la parte de cosmos del horizonte sensible en nuestro cerebro? Este reflejo unido, contrastado, con las imágenes reflejadas en los cerebros de los demás hombres que han vivido y que viven, es nuestro conocimiento del mundo, es nuestro mundo. ”

Pio Baroja

Acknowlegments

The first person to thank is my mother, Rosa Maria, for always supporting me in my academic career and setting a great example for me.

Secondly, my Ph.D. advisor, Hilda Cerdeira, for accepting me as a student and always being kind and encouraging. Although I feel like I did not answer the majority of Hilda's questions, I am sure I have learned a lot by pursuing the answers. This thesis is the result of some of these attempts.

I would also like to express my gratitude to Cristina Masoller, who hosted me during my secondment at the Universitat Politècnica de Catalunya in Terrassa and has always been very kind and helpful. Trying to keep up with Cristina's sharp mind was not easy, but I have grown a lot as a researcher in the process.

Another person who must be remembered is Giulio Tirabassi, whose patience and kindness made my learning journey in time series analysis much easier. I cannot count how many times I entered his office, eager to discuss a new result or a doubt, and he was always willing to help. Likewise, I am thankful to Antonio Pons, who has an endless enthusiasm for research.

A special thanks to all my colleagues at IFT, UPC, and the friends that I have made during my Ph.D.: Antonio, Cassiano, Dennis, Eggon, Enzo, Isabela, Lucas, Luis, Maria, Madhu, Pol, Rafael, and Sophie. You guys made me feel at home even when I was far from it. I also extend my appreciation to my dear friends Aron, Bárbara, Enrique, Edson, and Vitor. Altogether, their company made this journey much easier. Similarly, my gratitude goes to my brothers Giancarllo and Vinícius. Last but not least, I am very thankful to my partner, Mônica, for her endless support and love.

Finally, I would like to express my gratitude to the examination committee, especially Prof. Nicolas Rubido. I would also like to thank IFT for providing great physical infrastructure and Coordenação de Aperfeiçoamento de Pessoal de Nível Superior - Brasil (CAPES) for financing it under Finance Code 001.

Abstract

In this thesis, we delve into two interconnected realms: the stability of synchronized states in networks of Izhikevich neurons and the challenge of network inference within complex systems. The motivation stems from the ubiquity of complex networks in nature, where synchronization often occurs, presenting an intricacy when the underlying network structure is unknown.

The analytical foundation of our investigation lies in the application of the Master Stability Function (MSF) formalism to study the stability of synchronized states in networks of Izhikevich neurons. Despite the Izhikevich model's widespread use, this study represents the first application of the MSF to the Izhikevich model, which was made possible by using the Saltation Matrices approach.

Through this analytical framework, we explore total synchronized states and cluster synchronized states in networks with electrical and chemical couplings. Notably, the study reveals the nuanced behavior of synchronization, with the presence of a riddled basin of attraction near synchronization thresholds. The MSF, while a valuable tool, is shown to be susceptible to discrepancies, emphasizing the need for a cautious interpretation.

Transitioning to the second part of the thesis, we address the problem of network inference using the Unscented Kalman filter (UKF). The UKF is first tested on an isolated Izhikevich neuron, demonstrating remarkable accuracy in inferring parameters even under the influence of varying input currents. Extending the application to networks, the UKF successfully infers both electrical and electrical-chemical coupling structures.

In a novel approach, we employ the UKF for network inference based on event timing data. Associating a phase with timing events, we assimilate this information into the Kuramoto model, revealing in some cases, superior performance compared to mutual information and cross-correlation on synthetic data. However, computational costs make the approach impractical for large networks.

Keywords: Synchronization; Izhikevich Neuron; Master Stability Function; Kalman Filter; Complex Networks; Network Inference.
Knowledge Area: Physics; Non-linear Dynamics; Complex Networks; Time Series Analysis.

Resumo

Nesta tese, exploramos dois domínios interconectados: a estabilidade de estados sincronizados em redes de neurônios Izhikevich e o desafio da inferência de redes em sistemas complexos. A motivação advém da ubiquidade de redes complexas na natureza, onde a sincronização frequentemente ocorre, apresentando uma complexidade quando a estrutura subjacente da rede é desconhecida.

A base analítica de nossa investigação reside na aplicação do formalismo da *Função de Estabilidade Mestra* (MSF) para estudar a estabilidade de estados sincronizados em redes de neurônios Izhikevich. Apesar do uso generalizado do modelo Izhikevich, este estudo representa a primeira aplicação da MSF ao modelo Izhikevich, tornada possível pelo uso da abordagem de matrizes de saltos.

Através deste arcabouço analítico, exploramos estados totalmente sincronizados e estados sincronizados em aglomerados em redes com acoplamentos elétricos e químicos. Notavelmente, o estudo revela o comportamento sutil da sincronização, com a presença de uma bacia de atração *riddled* próxima aos limiares de sincronização. A MSF, embora uma ferramenta valiosa, mostra-se suscetível a discrepâncias, enfatizando a necessidade de uma interpretação cuidadosa.

Transitando para a segunda parte da tese, abordamos o problema da inferência de redes usando o filtro de Kalman *Unscented* (UKF). O UKF é primeiro testado em um neurônio Izhikevich isolado, demonstrando uma precisão notável na inferência de parâmetros mesmo sob a influência de correntes de entrada variáveis. Estendendo a aplicação para redes, o UKF infere com sucesso as estruturas de acoplamento elétrico e elétrico-químico.

Em uma abordagem inovadora, empregamos o UKF para inferência de redes com base em dados de temporização de eventos. Associando uma fase a eventos de temporização, assimilamos essa informação no modelo de Kuramoto, revelando em alguns casos, desempenho superior em comparação com informações mútuas e correlação cruzada em dados sintéticos. No entanto, os custos computacionais tornam a abordagem impraticável para grandes redes.

Palavras Chaves: Sincronização; Neurônios de Izhikevich; Função de Estabilidade Mestra; Filtro de Kalman; Redes Complexas; Inferência de redes.
Áreas do Conhecimento: Física; Dinâmica Não-Linear; Redes Complexas; Análise de Séries Temporais.

Contents

List of Figures

List of Tables

Part I

Introduction

1 Introduction

1.1 Izhikevich Model

Neurons are the building blocks of the brain. These structures can display a rich variety of dynamics depending on their type and the inputs that it receives from other neurons [1]. Although many features of neurons remain unclear, models are capable of reproducing their observed dynamics. The seminal work of Hodgkin-Huxley (HH) introduced a neuron model based on the giant axon of the squid [2]. As it is biophysically accurate, this model has become a standard for ordinary differential equation (ODE)-based neuron models. Naturally, the collective dynamics of neurons are also of interest, and unfortunately, networks of complex models like the HH can be difficult to deal with both, analytically and computationally. With this in mind, E. M. Izhikevich proposed a neuron model that combines biological features of complex models, like the HH, with computational efficiency [3].

The equations of the model are the following:

$$\begin{bmatrix} x(t) \\ y(t) \end{bmatrix} = \begin{bmatrix} 0.04x^2 + 5x + 140 - y + I(t) \\ a(bx - y) \end{bmatrix} \tag{1.1}$$

with the after-spike reset given by

$$\text{if} \quad x \geq 30, \quad \text{then} \begin{cases} x \to c \\ y \to y + d \end{cases} \tag{1.2}$$

Where the variables x and y represent the membrane potential and a membrane recovery variable respectively. a is associated with the time scale of y while b describes the sensibility of x to subthreshold oscillations of y. The parameters c and d are related to the after-spike dynamics of the variables x and y. The parameter I takes into account synaptic currents or injected dc-currents [3]. The different types of neuronal activity that the Izhikevich model (IM) can emulate are shown in Fig. 1.1.

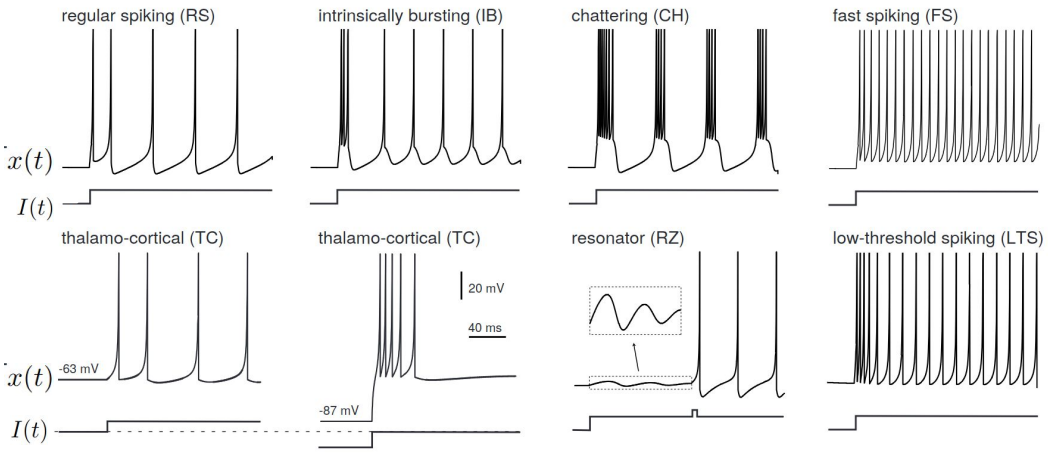

Figure 1.1: Some of the neuronal activity types that the IM (1.1) is capable of displaying for different values of (a, b, c, d) in response to a step of current $I(t)$. Adapted from [3].

Due to these characteristics, the IM has been implemented in the study of networks of spiking neurons, including large-scale models [4, 5]. Such models can be used to deepen our understanding of how the interplay between synaptic and neuronal processes produces collective behaviors. Of great interest is the emergence of rhythms and synchronization of neural activity, as it suggests that the high-dimensional dynamics of neuronal networks can collapse into low-dimensional oscillatory modes [6].

1.2 Synchronization

Synchronization occurs when a set of oscillators, interacting with each other (coupled) in some way, adjust their rhythms due to this interaction. As an example, we can mention the story of the Dutch researcher Christiaan Huygens, who observed and described the phenomenon of synchronization in the 17th century. What fascinated Huygens was the fact that the pendulum swings of two clocks fixed on the same wooden beam, reached a state of complete agreement, so much so that their sounds were heard simultaneously. This state was disrupted by interference, but after a short period, it was restored. As he pointed out, the explanation for this phenomenon is that the movement of one clock's pendulum transmitted vibrations through the beam to which it was attached and consequently to the case of the other clock, affecting the other pendulum's motion [7].

However, synchronization goes far beyond the clocks observed by Huygens, probably being the first non-linear effect studied scientifically [8]. It occurs daily in our bodies and nature. This is because biochemical and biophysical rhythms are omnipresent features in living beings, from rapid oscillations in cell membranes to the slow cycles of ovulation in mammals and circadian cycles [9].

Since Huygens' studies on synchronization, many other researchers have tackled this problem and nowadays synchronization is an established field of research in nonlinear

sciences. From the analytical part, we highlight the work of Winfree, who saw synchronization as the result of a cooperative phenomenon. Drawing an analogy between synchronization and order from statistical physics, he described the transition to synchronization as a phase transition [10, 11]. Likewise, the work of Kuramoto, who is responsible for the first mathematically tractable model for synchronization [12, 13]. Finally, Pecora and Carroll's work summarizes the efforts to study the stability of synchronized states [14]. While the latter is commonly employed in studying synchronized states, in this thesis we present the first attempt to apply it to networks of Izhikevich neurons.

This holds significance as synchronization plays a crucial role in neuroscience, with studies suggesting its importance for communication between cortical areas and information processing [15–18]. However, synchronization is also associated with various brain pathologies such as Parkinson's disease, Alzheimer's, schizophrenia, and epilepsy [19, 20]. The case of epilepsy may be related to the presence of domains of synchronized activity coexisting with domains of asynchronous brain activity, known as chimeras [21, 22]. Since the observed patterns of synchronization in nature are far from being fully understood, their study is of great relevance.

But, to bridge the gap between synchronization in models and nature, unavoidably, we have to delve into the data from experiments and measurements, as time series analysis allows us to learn many characteristics of a system. We can identify, for example, whether the system in question is periodic, stochastic, or chaotic, and also the interaction and synchronization between elements [23–25]. And, more importantly, as we will study in this thesis, the analysis can also help us to have a better understanding of the underlying structure of these systems, i.e., the networks that encode the interactions between the elements of the system under study.

1.3 Network inference

Unraveling the structure of a network from observed data is a crucial open challenge in complexity science and, mathematically, an undetermined problem [26], implying that a singular solution does not exist [27]. The inherent significance of this problem is inevitable, given that many natural systems can be perceived as complex networks. Consequently, the interactions dictated by these networks impact the data obtained from such systems [28].

Among the many applications of network inference [29], like epidemiology [30], ecology [31], and social networks [32], one of the most famous is computational biology - which elucidates interactions between genes and cellular processes [33]. In this framework networks can help when describing processes, which are thought of as links of the networks, between proteins, enzymes, and genes, the nodes of the resulting networks.

Climate networks, in turn, encode relationships within environmental subsystems with complex dynamics like ecosystems and the atmosphere [34, 35]. The study of such networks can be helpful in understanding and mitigating the effects of climate change.

In the field of neuroscience, one can explore networks that span various scales, from expansive cortical areas to intricate individual neurons [36, 37]. While significant advancements have been achieved in exploring the connection between brain topology and

dynamics, researchers have yet to attain a comprehensive understanding. [38, 39]. Thus, the study of such networks is important to better understand the functioning of the brain and its disorders.

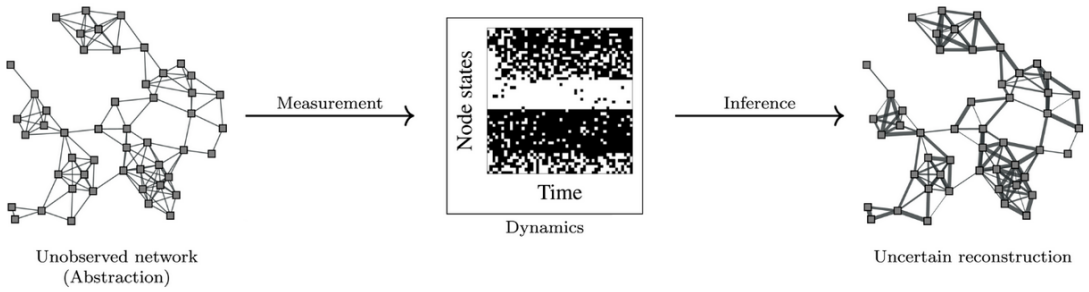

Figure 1.2: Framework for network inference using information (dynamics) obtained through measurements. Adapted from [29].

As represented in Fig. 1.2, the real network is not usually observed. This means we can say that the links are hidden variables, and we can only perform measurements on the units of the system (in the best-case scenario one can measure all the units) which will give us some feature (variable) of the system. With this in hand, we try to perform the network inference. One of the challenges of network inference is that, when using time series data, usually only one or a few variables can be observed (often not simultaneously), the observed variables can be recorded during a limited time interval, with limited temporal resolution, and with often unavoidable observational noise [27, 29].

On top of that, many times we rely solely on the data, without having a model for our system. Thus, deciding on a model that best encodes the network relationships of the variables observed becomes rather non-trivial. In such cases, researchers may end up using ad-hoc tuning of network model parameters [27, 28].

Naturally, it comes as no surprise that the list of methods proposed for network inference is as long as the number of applications for it. A popular approach is to perform some analysis between the time series of each node, like measuring the correlation between them, and the result one obtains is a matrix representing the measurement between all pairs of nodes. Then, a matrix representing the connections can be obtained by thresholding the covariance matrix. This approach can be used with other types of measures of similarity.

Moreover, we also find dedicated methods based on machine learning algorithms[40–42] bayesian inference[29, 43, 44] model-based [45–47] or model-independent approaches [48–54], among other types [55–59]. Here, we will build upon the work presented in [60], which utilized the Kalman filter [61] as a data assimilation tool to infer the connectivity of a network of Rössler oscillators [62]. In this continuation, our emphasis will shift to the study of networks of Izhikevich neurons.

1.4 Objectives

As we have seen, synchronization is present in many systems in nature that can be modeled as networks. On top of that, information about the underlying network is often missing, which can limit the analysis of such systems, and inferring the network from data is a challenging task.

With this in mind and drawing inspiration from neuroscience, the goal of this thesis is to explore these two themes using the IM as our framework. Part of the motivation stems from the fact that the examination of synchronization in networks of IM has yet to incorporate the application of the Master Stability Function. Additionally, our objective extends to inferring the network structure when the only available data is the timing of events, such as inter-spike intervals of neurons.

1.5 Outline

This thesis is divided into five parts, each comprising specific chapters. The first part serves as an introduction to the subjects and the motivation behind the thesis, paving the way for the subsequent discussions.

Transitioning from the introduction, Part II begins the core of the thesis, exploring synchronization in networks of Izhikevich neurons.

Chapter 2 is dedicated to introducing the Master Stability Function (MSF), the tool we use for analyzing both total synchronized and cluster-synchronized states in networks of Izhikevich neurons.

In the third Chapter, building upon the MSF revised in Chapter 2, we present the results of applying the MSF formalism to networks of Izhikevich neurons. We specifically focus on studying the stability of total and cluster synchronized states in small networks of electrically and chemically coupled neurons.

Transitioning from the study of synchronization in Part II, Part III is dedicated to the problem of network inference and the utilization of Kalman filters to address this challenge.

In Chapter 4, we shift our focus to network inference, introducing the concept of Bayesian filters and, specifically, the Kalman filter. Given our objective of studying nonlinear problems, we explore the Unscented Kalman filter —a version designed to handle nonlinearities— and discuss how these tools can be employed to infer the parameters of a given model.

In Chapter 5, we present the results of applying the Unscented Kalman filter (UKF) to infer the parameters of a given model, using the time series data of an Izhikevich neuron. Additionally, we extend our exploration to network inference, investigating small networks of Izhikevich neurons with both electrical and chemical couplings.

Closing Part III, Chapter 6 addresses the challenging problem of network inference when only event timing data, such as the spikes of a neuron, is available. In this chapter, we introduce a novel approach by combining the Kalman filter with the Kuramoto model to

effectively fit the data. The results of this method are presented using interspike interval data from Izhikevich neurons and experimental data from an electronic circuit.

Part IV is dedicated to summarizing the conclusions and discussions arising from the results presented in the thesis. Finally, the thesis concludes with some perspectives, presenting future avenues of research.

Following the conclusions chapter, four appendices are included. Appendix A complements the theoretical framework used in Chapter 3, while Appendix B covers the mathematical details of Chapter 4. Additionally, Appendices C and D contain supplementary material related to the findings in Chapters 5 and 6. These appendices were placed at the end to ensure the fluidity of the main text and the core chapters of the thesis.

Part II

Synchronization

2 Synchronization of Chaotic Networks

2.1 Stability and Synchronization

As posed by Heagy et al., in the context of coupled dynamical systems, the classic synchronization problem can be written as "will my system ever synchronize and, if so, under what conditions?" [63]. During the last decades of the twentieth century, chaotic oscillators were at the center of such a problem. All this interest resulted in many works, two of them being especially important due to the use of variational equations to study the stability of synchronized solutions.

Although the idea of analyzing how perturbations grow (or decay) with time was not new to nonlinear systems, Fujisaka and Yamada were the first to use Lyapunov exponents [64, 65] to tackle the problem of the stability of synchronized motion of coupled oscillators [66]. They considered coupling schemes such as global coupling and only nearest neighbor with and without periodic boundary conditions. Starting from a system with N nodes the form

$$\dot{\mathbf{x}}^i = \mathbf{F}(\mathbf{x}^i) + \sigma \sum_j A_{ij}(\mathbf{x}^j - \mathbf{x}^i) \, . \tag{2.1}$$

Where $\mathbf{x}^i$ is the m-dimensional vector of dynamical variables of the ith node, and assuming that the isolated dynamics of each node are described by the vector field $\mathbf{F} : \mathbb{R} \to \mathbb{R}^m$. Additionally, σ is the coupling strength and A_{ij} is the adjacency matrix that encodes the network structure, which is defined as

$$A_{ij} = \begin{cases} 1, & \text{if there is an edge between nodes} \quad i \text{ and } j \\ 0, & \text{otherwise} \end{cases} \, . \tag{2.2}$$

Using that the synchronized solution satisfies $\sum_j A_{ij}(\mathbf{x}^j - \mathbf{x}^i) = 0$, which is now known as global (or total) synchronization, they derived a *stability parameter* λ' such that for $\lambda' < 0$ the synchronized state is stable, and unstable against infinitesimal perturbations if $\lambda' > 0$. As we will see in the next sections, the stability of the synchronized solution will depend on the dynamics of the isolated node, the coupling strength, and the network architecture.

Moreover, the stability parameter turns out to be the Maximum (or Largest) Lyapunov Exponent (MLE) of the dynamical system transverse to the synchronized solution. A similar approach was used by Shnöl a few years later, in the context of periodic oscillators [67].

Beyond the global synchronized state, one can also observe solutions where the system splits itself into groups displaying the same dynamics. The stability of this so-called *cluster synchronization* was first studied by Kaneko in the context of coupled maps [68] and later by Terry *et al.*, analytically and experimentally with an array of lasers [69].

All these works were essential to the development of formalism known as the *Master Stability Function* (MSF), derived by Pecora and Carrol in [14]. The MSF generalizes the results of previous works, especially [66], and allows one to calculate the threshold for total synchronization, and the linear stability of such a state. Throughout the years, the MSF was extended to networks of non-identical oscillators, directed networks, networks with noise, and more recently to cluster synchronized states and multilayer networks [70–73].

2.2 Master Stability Function

In this section, we derive the MSF formalism following Pecora et al. [14], using the Rössler oscillator [62] in the hope that it serves as a foundational step. Given that the Rössler oscillator is a classical example of chaotic systems, we can focus on the intricacies of the MSF, leaving the application details to the Izhikevich neuron for the next Chapter. The MSF offers a systematic framework for analyzing synchronized states in networks of coupled oscillators. The revised formalism presented here serves as the foundation for this particular part of the thesis.

Let there be N nodes, with $\mathbf{x}^i$ being the m-dimensional vector of dynamical variables of the ith node. The isolated dynamic of each node is described by the vector field $\mathbf{F} : \mathbb{R} \to \mathbb{R}^m$, i.e. $\dot{\mathbf{x}}^i = \mathbf{F}(\mathbf{x}^i)$. $\mathbf{H} : \mathbb{R}^m \to \mathbb{R}^m$ is a function of each node's variables that is used together with the structure of the network to define the coupling. Now, let $\mathbf{x} = [\mathbf{x}^1, \mathbf{x}^2, ..., \mathbf{x}^N]^T$, $\mathbf{F}(\mathbf{x}) = [\mathbf{F}(\mathbf{x}^1), \mathbf{F}(\mathbf{x}^2), ..., \mathbf{F}(\mathbf{x}^N)]^T$ and $\mathbf{H}(\mathbf{x}) = [\mathbf{H}(\mathbf{x}^1), \mathbf{H}(\mathbf{x}^2), ..., \mathbf{H}(\mathbf{x}^N)]^T$. Then, in the case of diffusive coupling, the equations of motion are

$$\dot{\mathbf{x}} = \mathbf{F}(\mathbf{x}) - \sigma L \otimes \mathbf{H}(\mathbf{x}) \tag{2.3}$$

where σ is the coupling strength, $\otimes$ represents the Kronecker product[1] [74], and L is the Laplacian matrix, which is given by

$$L = \{L_{ij}\}, \quad L_{ij} = (\delta_{ij} \sum_j A_{ij}) - A_{ij} \tag{2.4}$$

and δ_{ij} is the Kronecker delta. The second term, $\delta_{ij} \sum_j A_{ij}$ is known as the degree matrix, a diagonal matrix with the number of links of each node in the main diagonal.

[1]The Kronecker product, denoted $A \otimes B$, combines matrices A and B to create a larger matrix, where each element of A is multiplied by the entire matrix B. If A is a $m \times n$ matrix and B is $p \times q$, the result is a $pm \times qn$ matrix.

As an example, consider a network of $N = 2$ Rössler oscillators. If they are coupled only by the first variable of each node, like in [14], we have

$$\mathbf{F}(\mathbf{x}^i) = \begin{bmatrix} -y_i - z_i \\ x_i + a y_i \\ b + z_i(x_i - c) \end{bmatrix} \qquad L = \begin{bmatrix} 1 & -1 \\ -1 & 1 \end{bmatrix} \qquad \mathbf{H} = \begin{bmatrix} 1 & 0 & 0 \\ 0 & 0 & 0 \\ 0 & 0 & 0 \end{bmatrix} . \tag{2.5}$$

which, using Eq. (2.3), leads to

$$\begin{bmatrix} \dot{x_1} \\ \dot{y_1} \\ \dot{z_1} \\ \dot{x_2} \\ \dot{y_2} \\ \dot{z_2} \end{bmatrix} = \begin{bmatrix} -y_1 - z_1 \\ x_1 + a y_1 \\ b + z_1(x_1 - c) \\ -y_2 - z_2 \\ x_2 + a y_2 \\ b + z_2(x_2 - c) \end{bmatrix} - \sigma \begin{bmatrix} x_1 - x_2 \\ 0 \\ 0 \\ x_2 - x_1 \\ 0 \\ 0 \end{bmatrix} . \tag{2.6}$$

The synchronization manifold $\mathbf{x}^s$ is defined by the $N - 1$ constraints

$$\mathbf{x}^1 = \mathbf{x}^2 = ... = \mathbf{x}^N = \mathbf{x}^s \, , \tag{2.7}$$

and as a consequence of the Laplacian matrix being a zero row-sum matrix, we have that

$$L \otimes \mathbf{H}(\mathbf{x}^s) = \mathbf{0} \, , \tag{2.8}$$

which is the second term of Eq. (2.6) when $x_1 = x_2$. This yields the synchronized solution $\dot{\mathbf{x}}^s = \mathbf{F}(\mathbf{x}^s)$.

In order to study the stability of the synchronization solution, we can analyze how small perturbations to it evolve, i.e. $\delta\mathbf{x}^i = \mathbf{x}^i - \mathbf{x}^s$, where $\mathbf{x}^s = [x_s, y_s, z_s]^T$. Using linear stability analysis, we have for each node

$$\dot{\mathbf{x}}^i \approx \mathbf{F}(\mathbf{x}^s) + D\mathbf{F}(\mathbf{x})\Big|_{\mathbf{x}^s} \delta\mathbf{x}^i - \sigma \sum_j L_{ij} D\mathbf{H}(\mathbf{x})\Big|_{\mathbf{x}^s} \delta\mathbf{x}^j \tag{2.9}$$

hence

$$\delta\dot{\mathbf{x}}^i = \dot{\mathbf{x}}^i - \dot{\mathbf{x}}^s = D\mathbf{F}(\mathbf{x})\Big|_{\mathbf{x}^s} \delta\mathbf{x}^i - \sigma \sum_j L_{ij} D\mathbf{H}(\mathbf{x})\Big|_{\mathbf{x}^s} \delta\mathbf{x}^j \tag{2.10}$$

where D is the Jacobian matrix. Using a $N \times N$ identity matrix $\mathbf{I}_N$, we can write an equation for $\delta\dot{\mathbf{x}} = [\delta\dot{\mathbf{x}}^1, \delta\dot{\mathbf{x}}^2, ..., \delta\dot{\mathbf{x}}^N]^T$

$$\delta\dot{\mathbf{x}} = [\mathbf{I}_N \otimes D\mathbf{F}(\mathbf{x}^s) - \sigma L \otimes D\mathbf{H}(\mathbf{x}^s)]\delta\mathbf{x} \, . \tag{2.11}$$

Note that the coupling term in Eq. (2.11) becomes problematic, as different modes of perturbation, $\delta\mathbf{x}$, end up being coupled. Therefore, we cannot distinguish perturbations parallel to the synchronized manifold from those orthogonal to it. Ideally, we want to access information about the evolution of perturbation modes in each possible direction separately. To achieve it, let's first turn our attention to our Laplacian matrix. In the general case of symmetric and undirected coupling, which we will consider in this thesis, L has important properties:

- A real non-negative set of eigenvalues ($\gamma_i \geq 0$)
- The associated set of eigenvectors constitutes an orthonormal basis of $\mathbb{R}^N$
- The smallest eigenvalue is $\gamma_1 = 0$, which is associated to the eigenvector

$$V_1 = \pm\frac{1}{\sqrt{N}}(1, 1, 1, ..., 1)^T \,. \tag{2.12}$$

Importantly, V_1 is aligned with the synchronization manifold $\mathcal{S}$, and all the other eigenvalues have associated eigenvectors spanning all the phase space transverse to $\mathcal{S}$ [75]. Due to these properties, L has a diagonalization form

$$V^{-1}LV = \mathbf{\Gamma} = diag(\gamma_1, \gamma_2, ..., \gamma_N) \tag{2.13}$$

where $V = [V_1, V_2, ..., V_N]$ is an orthonormal matrix whose columns are eigenvectors of L, and $\mathbf{\Gamma}$ is a diagonal matrix whose diagonal elements are associated eigenvalues ordered by magnitude.

We define a new set of variables $\eta = (V^{-1} \otimes \mathbf{I}_m)\delta\mathbf{x}$, so that Eq. (2.11) becomes

$$(V \otimes I_m)\dot{\eta} = [\mathbf{I}_N \otimes D\mathbf{F}(\mathbf{x}^s) - \sigma L \otimes D\mathbf{H}(\mathbf{x}^s)](V \otimes \mathbf{I}_m)\eta \tag{2.14}$$

solving for η

$$\dot{\eta} = (V^{-1} \otimes \mathbf{I}_m)[\mathbf{I}_N \otimes D\mathbf{F}(\mathbf{x}^s) - \sigma L \otimes D\mathbf{H}(\mathbf{x}^s)](V \otimes \mathbf{I}_m)\eta \tag{2.15}$$

which give us

$$\dot{\eta} = [\mathbf{I}_N \otimes D\mathbf{F}(\mathbf{x}^s) - \sigma\mathbf{\Gamma} \otimes D\mathbf{H}(\mathbf{x}^s)]\eta \,. \tag{2.16}$$

Equation (2.16) is the celebrated *Master Stability Function*, a block diagonalized variational equation where each block has the form

$$\dot{\eta}_k = [D\mathbf{F}(\mathbf{x}^s) - \sigma\gamma_k D\mathbf{H}(\mathbf{x}^s)]\eta_k \,. \tag{2.17}$$

Therefore, we have successfully decoupled the variational equation (2.11), with η_1 accounting for perturbations parallel to the motion along the synchronous manifold, and all other variables η_i (for $i > 1$) representing transverse modes [14].

Let's return to our simple example of two Rössler oscillators, we have for $D\mathbf{F}$ and $D\mathbf{H}$

$$D\mathbf{F}(\mathbf{x})\big|_{\mathbf{x}^s} = \begin{bmatrix} 0 & -1 & -1 \\ 1 & a & 0 \\ z_s & 0 & (x_s - c) \end{bmatrix}, \qquad D\mathbf{H}(\mathbf{x})\big|_{\mathbf{x}^s} = \begin{bmatrix} 1 & 0 & 0 \\ 0 & 0 & 0 \\ 0 & 0 & 0 \end{bmatrix} . \tag{2.18}$$

The Laplacian matrix L has eigenvalues $\gamma_1 = 0$ and $\gamma_2 = 2$, so that V is

$$V = V^{-1} = \frac{1}{\sqrt{2}}\begin{bmatrix} 1 & 1 \\ 1 & -1 \end{bmatrix} \quad \text{which give us} \quad \eta = \left(\frac{1}{\sqrt{2}}\begin{bmatrix} 1 & 1 \\ 1 & -1 \end{bmatrix} \otimes \begin{bmatrix} 1 & 0 & 0 \\ 0 & 1 & 0 \\ 0 & 0 & 1 \end{bmatrix}\right)\delta\mathbf{x} \,, \tag{2.19}$$

thus, using that $\delta\mathbf{x} = [\mathbf{x} - \mathbf{x}^s]^T = [\mathbf{x}^1 - \mathbf{x}^s, \mathbf{x}^2 - \mathbf{x}^s]^T$,

$$\eta = \frac{1}{\sqrt{2}} \begin{bmatrix} x_1 + x_2 - 2x_s \\ y_1 + y_2 - 2y_s \\ z_1 + z_2 - 2z_s \\ x_1 - x_2 \\ y_1 - y_2 \\ z_1 - z_2 \end{bmatrix} = \frac{1}{\sqrt{2}} \begin{bmatrix} \mathbf{x}^1 + \mathbf{x}^2 - 2\mathbf{x}^s \\ \mathbf{x}^1 - \mathbf{x}^2 \end{bmatrix} = \begin{bmatrix} \eta_1 \\ \eta_2 \end{bmatrix} . \tag{2.20}$$

Plugging the latter on Eq. (2.16) one obtains

$$\begin{bmatrix} \dot{\eta}_1 \\ \dot{\eta}_2 \end{bmatrix} = \begin{bmatrix} D\mathbf{F} & \mathbf{O} \\ \mathbf{O} & D\mathbf{F} - 2\sigma\mathbf{H} \end{bmatrix} \begin{bmatrix} \eta_1 \\ \eta_2 \end{bmatrix} , \tag{2.21}$$

where $\mathbf{O}$ is a $m \times m$ null matrix. This yields

$$\dot{\eta_1} = \begin{bmatrix} -\eta_{1y} - \eta_{1z} \\ \eta_{1x} + a\eta_{1y} \\ z_s\eta_{1x} + (x_s - c)\eta_{1z} \end{bmatrix} \tag{2.22}$$

and

$$\dot{\eta_2} = \begin{bmatrix} -2\sigma\eta_{2x} - \eta_{2y} - \eta_{2z} \\ \eta_{2x} + a\eta_{2y} \\ z_s\eta_{2x} + (x_s - c)\eta_{2z} \end{bmatrix} . \tag{2.23}$$

Putting everything together, we can express $\dot{\eta}_1$ and $\dot{\eta}_2$ in a more compact form:

$$\begin{aligned} \dot{\eta}_1 &= (D\mathbf{F})\eta_1 \\ \dot{\eta}_2 &= (D\mathbf{F} - 2\sigma D\mathbf{H})\eta_2 . \end{aligned} \tag{2.24}$$

Notice that the first equation gives us the evolution of perturbations to the uncoupled system, $\dot{\mathbf{x}}^\mathbf{s} = \mathbf{F}(\mathbf{x}^s)$, therefore, it allows us to obtain Lyapunov exponents of the original system. Plus, if $\sigma = 0$, the second equation is equivalent to the first one. By calculating the maximum Lyapunov exponent Λ of the second equation we can verify the stability of the synchronization solution. The result is shown in Fig. 2.1, where the Maximum Lyapunov exponent was calculated using the method proposed in [76], using $a = 0.2$, $b = 0.2$, and $c = 7.0$ in the Rössler equations.

In general, the synchronous solution is linearly stable if the set of $(N-1)m$ Lyapunov exponents that correspond to the phase space transverse to $\mathcal{S}$ are negative. This reads,

$$\Lambda(\sigma\gamma_i) < 0 . \tag{2.25}$$

So, for the Rössler oscillators here considered, this condition is satisfied for

$$0.14 < \gamma_2\sigma < 4.47, \quad \text{and since } \gamma_2 = 2, \quad 0.07 < \sigma < 2.235. \tag{2.26}$$

According to Checco et al., [77], if we denote the synchronization region as Ω, and assuming that there only three eigenvalues, there are three possible forms that it can take:

- $\Omega_1 = \emptyset$
- $\Omega_2 = (\sigma\gamma^2, +\infty)$
- $\Omega_3 = \bigcup(\sigma\gamma^2, \sigma\gamma^3)$

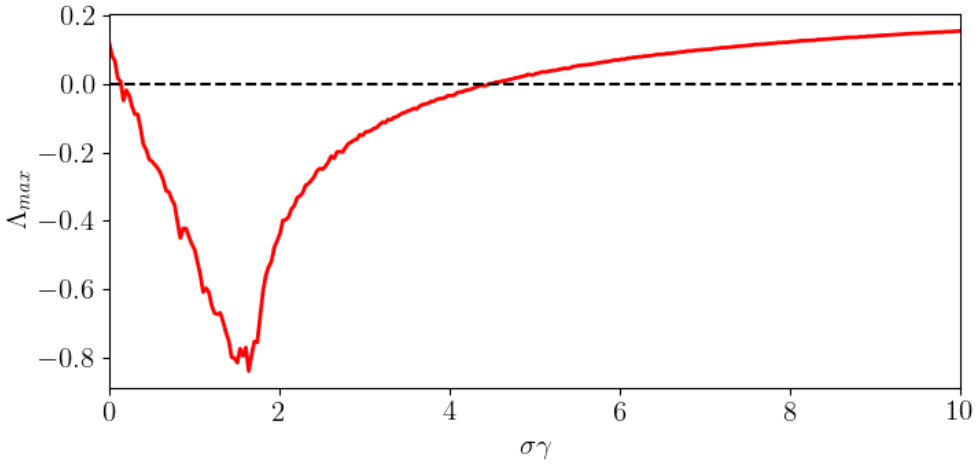

Figure 2.1: Maximum Lyapunov exponent transverse to the synchronization manifold Λ_{max}, as a function of the coupling strength σ and the corresponding eigenvalue γ for $N = 2$ Rössler oscillators with diffusive coupling.

This means that the Lyapunov exponent associated with the synchronized manifold can be positive for all values of coupling, and therefore the synchronized solution is not stable (Ω_1 case). It can be positive up to a threshold σ_2, and beyond this threshold, it is always negative, yielding a stable synchronized solution (Ω_2 case). And lastly, it can be negative only within a range of values delimited by γ^2 and γ^3, turning positive outside this domain (in the Ω_3 case). The latter is illustrated in Fig. 2.1.

As important as the phenomenon of total synchronization is that of cluster synchronization, where the network is divided into clusters with the same evolution. Fortunately, as we will see in the next section, the MSF formalism has been extended to study the stability of such states.

2.3 MSF applied to Cluster Synchronization

In this section, we will cover the application of the MSF to cluster-synchronized states. To do this, let's once again consider a network with N nodes, where $\mathbf{x}^i$ is the m-dimensional vector of dynamical variables of the ith node. The local dynamic of each node is described by the vector field $\mathbf{F} : \mathbb{R} \to \mathbb{R}^m$. $\mathbf{H} : \mathbb{R}^m \to \mathbb{R}^m$ is a function of each node's variables that is

used together with the structure of the network to define the coupling. Hence, the equations of motion are the same as Eq. (2.3):

$$\dot{\mathbf{x}} = \mathbf{F}(\mathbf{x}) - \sigma L \otimes \mathbf{H}(\mathbf{x}) \,. \tag{2.27}$$

Consider now a cluster synchronized state with M clusters, with $1 \leq M \leq N$, where C_m is the set of nodes in the m-th cluster with synchronous motion $\mathbf{s}^m(t)$:

$$\mathbf{x}^i - \mathbf{x}^j = 0 \quad \text{if} \quad (i,j) \in C_m \rightarrow \mathbf{x}^i = \mathbf{x}^j = \mathbf{s}^m \,. \tag{2.28}$$

Thus, we have to look to small perturbations around the cluster synchronized state, i.e. $\delta\mathbf{x} = \mathbf{x} - \mathbf{s}^m$. This leads to the following variational equations

$$\delta\dot{\mathbf{x}} = \Big[\sum_m E^{(m)} \otimes D\mathbf{F}(\mathbf{s}^m) - \sigma \sum_m E^{(m)} L \otimes D\mathbf{H}(\mathbf{s}^m)\Big]\delta\mathbf{x} \,, \tag{2.29}$$

where $E^{(m)}$ is a N-dimensional diagonal matrix such that

$$E^{(m)}_{ij} = \begin{cases} 1, & \text{if } i \in C_m \\ 0, & \text{otherwise.} \end{cases} \tag{2.30}$$

Note that the case of global synchronization can be seen as a one-cluster state with $E^1 = \mathbf{I}^N$.

Our goal is to decouple the modes associated with the cluster synchronized manifold and the ones transverse to it, just as in the case of total synchronization. Naturally, one may proceed to diagonalize Eq. (2.29). The problem is that now we have $2m$ [2] matrices to be diagonalized, instead of only one matrix as in Eq. (2.11). As we know, a set of matrices cannot be simultaneously diagonalized unless they commute within each other, fortunately, we can find a transformation that leaves the set of $2m$ matrices simultaneously block-diagonalized. In the next subsections, we will discuss some of these methods.

2.3.1 External Equitable Partitions

The first method we will cover comes from a concept of graph theory known as *Equitable Partitions* (EP) [78–80]. We start with an extension of this concept, known as *External Equitable Partitions* (EEP). A key component in this method is the definition of a quotient graph. Given a graph encoded by a laplacian matrix L, we can partition the network into M clusters. Such a partition is encoded by an indicator matrix Z, such that $Z : Z_{ij} = 1$ if node i is in the cluster M_j and $Z_{ij} = 0$ otherwise [81]. Then, we can associate a graph with a number of nodes equal to the number of clusters of the original graph. This new graph, known as the quotient graph, will be encoded by a laplacian matrix L^π where the elements represent the number of connections between and within clusters. An example of this procedure is shown in Fig. (adapted from oclery Fig. 1),

[2] Since we end up with m $E^{(m)}$ matrices plus m $E^{(m)}L$ matrices.

where A and A_π are given by

$$L = \begin{bmatrix} 2 & 1 & 0 & 1 & 0 & 0 & 0 & 0 \\ 1 & 2 & 0 & 1 & 0 & 0 & 0 & 0 \\ 0 & 0 & 1 & 1 & 0 & 0 & 0 & 0 \\ 1 & 1 & 1 & 5 & 1 & 1 & 0 & 0 \\ 0 & 0 & 0 & 1 & 3 & 0 & 1 & 1 \\ 0 & 0 & 0 & 1 & 0 & 3 & 1 & 1 \\ 0 & 0 & 0 & 0 & 1 & 1 & 3 & 1 \\ 0 & 0 & 0 & 0 & 1 & 1 & 1 & 3 \end{bmatrix} \quad \text{and} \quad L^\pi = \begin{bmatrix} 1 & -1 & 0 & 0 \\ -3 & 5 & -2 & 0 \\ 0 & -1 & 3 & -2 \\ 0 & 0 & -2 & 2 \end{bmatrix} . \tag{2.31}$$

The partition is considered an EEP only if the original and the quotient laplacian matrices obey the following condition:

$$LZ = ZL^\pi . \tag{2.32}$$

This constraint ensures that each node in cluster M_j has the same number of connections with nodes in cluster M_i, for all i, j with $i \neq j$ [82, 83].

Equation (2.32) yields powerful spectral properties. Thanks to it, the laplacian matrices of the original graph and quotient graphs share eigenvectors and eigenvalues. In fact, the properties of the EEP ensure that a subset of eigenvectors, denoted as V_s, of the original Laplacian L is related to the eigenvectors of L^π by [81, 82]

$$V_s = HV^\pi \in \mathbb{R}^{N\times M} , \tag{2.33}$$

where V^π are the M eigenvectors of the quotient laplacian. Thus, the eigenvectors (2.33) define the cluster synchronized manifold, and the cluster synchronized state (CSS). The eigenvectors orthogonal to the CSS are denoted $V_\perp \in \mathbb{R}^{N\times(N-M)}$. These are the eigenmodes that can drive the system out of the CSS.

One can obtain an orthogonal matrix of eigenvectors V of L such that

$$V^T LV = \Gamma \quad \text{where} \quad \Gamma = \text{diag}(\gamma_i) , \tag{2.34}$$

where

$$V = [V_s, V_\perp] = [HV^\pi, V_\perp] , \quad \text{and} \quad V_\perp^T V_s = 0 . \tag{2.35}$$

As in the case of global synchronization, we define a coordinate transformation $\eta = (V^T \otimes \mathbf{I}_N)\delta\mathbf{x}$, which leads to

$$\dot\eta = \Big[\sum_m V^T E^m V \otimes D\mathbf{F}(\mathbf{s}^m) - \sigma \sum_m V^T E^{(m)} V V^T L V \otimes D\mathbf{H}(\mathbf{s}^m) \Big] \eta . \tag{2.36}$$

Defining the set of matrices

$$V^T E^m V = Q^m , \tag{2.37}$$

we can write $\dot\eta$ as

$$\dot\eta = \Big[\sum_m Q^m \otimes D\mathbf{F}(\mathbf{s}^m) - \sigma \sum_m \Gamma Q^m \otimes D\mathbf{H}(\mathbf{s}^m) \Big] \eta . \tag{2.38}$$

The structure of the matrices Q^m is given by

$$Q^m = V^T E^m V = \begin{bmatrix} Q_s^m & 0_{M\times(N-M)} \\ 0_{M\times(N-M)} & Q_\perp^m \end{bmatrix} . \tag{2.39}$$

Hence, we have succeeded in decoupling the variational equations for the CS manifold from others transverse to it.

2.3.2 Simultaneous Block Diagonalization

The simultaneous block diagonalization (SDB) of a set of matrices is a standard problem in group theory and has applications in field theory and synchronization theory. Due to this, many algorithms were developed aiming to deal with this problem, and here, we focus on the algorithm developed by Zhang et al. [84]. In contrast with the EEP formalism, their SBD framework does not require any information about the possible partitions of the network.

Remember that we want to find an orthogonal transformation Θ such the set of symmetric matrices $\mathcal{B} = [\mathbf{B}^{(1)}, ..., \mathbf{B}^M]$ can be simultaneously block diagolized by Θ. Then, the algorithm consists of the following steps.

- Find the eigenvectors $\mathbf{B} = \sum_{m=1}^{M} \xi_m \mathbf{B}^m$, where ξ_m are independent random coefficients which can be drawn from Gaussian distribution. Set $\mathbf{D} = [\mathbf{d}_1, ..., \mathbf{d}_N]$
- Generate $\mathbf{B} = \sum_{m=1}^{M} \xi_m \mathbf{B}^m$ for a new realization of ξ_m and compute $\tilde{\mathbf{B}} = \mathbf{D}^T \mathbf{B} \mathbf{D}$. Mark the indexes i and j as being in the same block if $\tilde{B}_{ij} \neq 0$
- Set $\Theta = [\mathbf{d}_{c(1)}, ..., \mathbf{d}_c(N)]$, where c is a permutation of $1, ..., N$ such that indexes in the same block are sorted consecutively.

This algorithm was based on the work by Maehara and Murota [85] and it yields the finest SBD given that there are no degeneracies in the set of eigenvalues. In this context, "finest" is defined by having the maximum number of common blocks, which is also equivalent to the blocks' sizes being minimal [84].

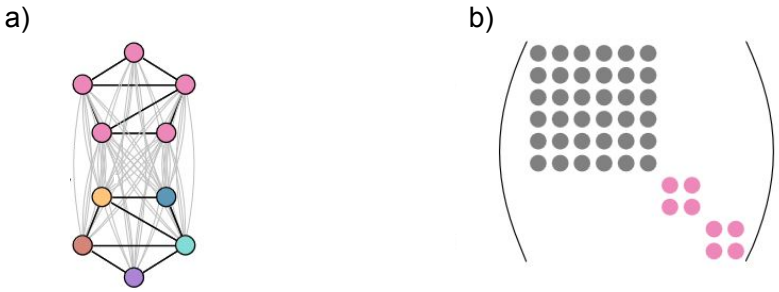

Figure 2.2: Example of simultaneous block diagonalization for a network of $N = 10$ elements. In (a), each color represents a solution, so the cluster state has $m = 6$ clusters, a cluster with five nodes (magenta) and five other cluster with only one node. As a result, in (b), the block Q_s^m that represents the perturbations parallel to the synchronized manifold is 6×6. Adapted from [84].

As we saw in this Chapter, the ceaseless interest in synchronization led to the development of the MSF formalism, which can be used to study the linear stability of synchronized states. In the following Chapter, we will use this framework to study total and cluster synchronized states in networks of Izhikevich neurons.

3 Master Stability Functions for Networks of Izhikevich neurons

This chapter presents the results of the research conducted in collaboration with Hilda A. Cerdeira[1]. The results here presented were summarized in a paper that is currently under review.

3.1 Introduction

As commented in the last Chapter 2.1, the mathematical description of synchronization is well established in nonlinear dynamics, and it can be applied to many natural phenomena, including neural activity. With this in mind, in this chapter, we apply the MSF formalism to study the linear stability of synchronized states in networks of Izhikevich neurons. Both global and partial synchronization patterns are considered. To calculate the associated Lyapunov exponents, we use the *Saltation Matrices* formalism, which takes into account the discontinuities of the Izhikevich model.

We study both global and cluster synchronization. First, we consider networks with electrical coupling, followed by the case with chemical coupling, and then with both coupling schemes. For each case, we study how the stability of the synchronized state depends on the coupling strength. We verify that the MSF formalism is effective for probing the threshold for synchronization, except for the last case, where the outcome of the system depends on its initial conditions. This can be the case when the system under study has a *riddled basin* of attraction [86]. As a result, the system evolves towards a non-synchronized solution even with initial conditions in the neighborhood of the synchronization state [87].

[1]Instituto de Física Teórica, Universidade Estadual Paulista, São Paulo, Brasil

3.2 MSF applied to Izhikevich Model

The Izhikevich model (IM) is a two-dimensional neuronal model, celebrated for its biophysical accuracy, and its capacity of displaying many spiking patterns without losing computational efficiency. Letting $\mathbf{x} = [x, y]^T$, the model consists of a system of differential equations [3]

$$\dot{\mathbf{x}} = \mathbf{F}(\mathbf{x}) = \begin{bmatrix} 0.04x^2 + 5x + 140 - y + I \\ a(bx - y) \end{bmatrix} \tag{3.1}$$

with the after-spike reset given by

$$\text{if} \quad x \geq 30, \quad \text{then} \begin{cases} x \to c \\ y \to y + d \end{cases} \tag{3.2}$$

For all calculations, we used $a = 0.2$, $b = 2$, $c = -56$, $d = -16$ and $I = -99$, with this choice of parameters, the IM displays chaotic dynamics, as discussed in Nobukawa et al. [88]. As in [3], the variables x and y and all the parameters are dimensionless.

The Izhikevich model can be seen as a hybrid model, a continuous-time evolution process interfaced with a logical process, in this case, the resetting function when x crosses the threshold. These discontinuities interfere with the usual straightforward methods [76, 89, 90] to compute the Lyapunov exponents of such a system.

Following Bizarri et al. [91] we resort to saltation matrices, which allow us to calculate the Lyapunov exponents associated with the master stability functions of networks of Izhikevich neurons. In this framework, these matrices are used as correction factors at the instants of the discontinuities due to the resetting function, yielding the correct Lyapunov exponents.

Between spikes the dynamics of the Izhikevich is smooth, and for a small perturbation $\delta\mathbf{x}$ we have

$$\delta\dot{\mathbf{x}} = D\mathbf{F}\big|_{\mathbf{x}}\delta\mathbf{x} \,, \tag{3.3}$$

where $D\mathbf{F}\big|_{\mathbf{x}}$ is the Jacobian matrix applied to $\mathbf{F}$ evaluated at $\mathbf{x}$. If a spike occurs, the after-spike reset (6.2) induces a discontinuity in the flow such that $D\mathbf{F}\big|_{\mathbf{x}^-} \neq D\mathbf{F}\big|_{\mathbf{x}^+}$, where $-$ and $+$ indicates the before and after the reset. Then, the perturbation $\delta\mathbf{x}^+$ after the reset event is given by

$$\delta\mathbf{x}^+ = S(D\mathbf{F}\big|_{\mathbf{x}^-}\delta\mathbf{x}^-) \,, \tag{3.4}$$

which allows us to write

$$\delta\dot{\mathbf{x}}^+ = D\mathbf{F}\big|_{\mathbf{x}^+}\delta\mathbf{x}^+ \,, \tag{3.5}$$

where S is the *saltation matrix*, which for Izhikevich neurons is given by

$$S = \begin{bmatrix} \dfrac{\dot{x}^+}{\dot{x}^-} & 0 \\ \dfrac{\dot{y}^+ - \dot{y}^-}{\dot{x}^-} & 1 \end{bmatrix} . \tag{3.6}$$

The complete derivation of the procedure can be found at [91, 92].

Throughout this study, we numerically solve Eq. (3.1) with a backward differentiation formula, which yields a variable integration step, with a maximal step of $dt = 0.001$. The initial conditions for the simulations, unless stated differently, were picked from a normal distribution centered at a fixed point of Eq. (3.1) in the case of no coupling, $(-56.25, -112.5)$, with a standard deviation equal to 1.

3.2.1 Electrical Coupling

First, we study the effect of electrical coupling, which represents electrical synapses between nodes [93]. Consider a network with N nodes, where the isolated dynamics of each node is given by Eq. (3.1). An adjacency matrix A indicates whether node i is diffusively connected through its first variable x to node j. In this case, the dynamics of each node is modified by

$$W_i = -g_e \sum_{j=1}^{N} A_{ij}(x^j - x^i) \tag{3.7}$$

where g_e is the coupling conductance (strength) and A_{ij} is an element of the adjacency matrix. Note that in this case, the coupling can be written as a function of the Laplacian matrix of the network, given by $L = D - A$ where D is the degree matrix defined by $D_{ii} = \sum_j A_{ij}$, then $W_i = g_e \sum_{j=1}^{N} L_{ij}x^j$. If we define $\mathbf{x} = [\mathbf{x}^1, ..., \mathbf{x}^N]^T$, where $\mathbf{x}^i = [x^i, y^i]^T$, and $\mathbf{F}(\mathbf{x}) = [\mathbf{F}(\mathbf{x}^1), ..., \mathbf{F}(\mathbf{x}^N)]^T$, we can write the dynamical system of the network as

$$\dot{\mathbf{x}} = \mathbf{F}(\mathbf{x}) - g_e(L \otimes \mathbf{G})\mathbf{x} \tag{3.8}$$

where $\otimes$ is the Kronecker product and

$$\mathbf{G} = \begin{bmatrix} 1 & 0 \\ 0 & 0 \end{bmatrix} \tag{3.9}$$

is the matrix encoding the coupling scheme. The synchronization manifold $\mathbf{x}^s$ is defined by the $N-1$ constraints $\mathbf{x}^1 = \mathbf{x}^2 = ... = \mathbf{x}^N$, and since the Laplacian matrix is a zero row-sum matrix, $(L \otimes \mathbf{G})\mathbf{x^s} = 0$, we have $\dot{\mathbf{x}}^\mathbf{s} = \mathbf{F}(\mathbf{x}^s)$. The linear stability of the synchronized solution can be investigated with the MSF of Eq. (3.8)

$$\dot{\eta}_k = [D\mathbf{F}\big|_{\mathbf{x}^s} - g_e\gamma_k D\mathbf{G}\big|_{\mathbf{x}^s}]\eta_k \ , \tag{3.10}$$

where γ_k is the k-th eigenvalue of L. Thus, the analysis is decomposed in eigenmodes, one being parallel to the synchronization manifold γ_0, the others transverse to it. We are interested in the Lyapunov exponents of transverse modes, which tell us whether or not perturbations to the synchronized solution will decay. We highlight that at the event of a spike, the synchronized solution $\mathbf{x}^s$ encounters a discontinuity, and therefore at this point, we need to apply the saltation matrix Eq. (3.6).

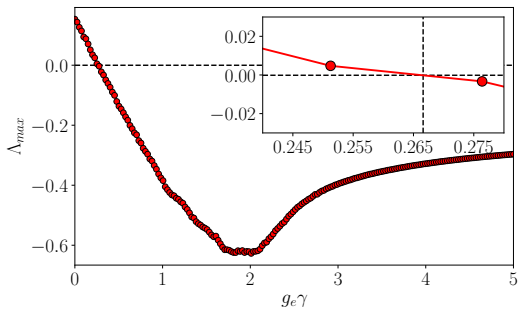

Figure 3.1: Maximum Lyapunov exponent transversal to the synchronization manifold for electrically coupled Izhikevich neurons as a function of $g\gamma$.

The maximum Lyapunov exponent (MLE) of Eq. (3.10) is presented in Fig. 3.1. The expanded inset shows that Λ_{max} becomes negative for $g_e\gamma \gtrapprox 0.2670$. To check our results, we simulate a network of $N = 4$ nodes, as depicted in Fig. 3.2. In such a case, the Laplacian matrix is

$$L = \begin{bmatrix} 2 & -1 & 0 & -1 \\ -1 & 2 & -1 & 0 \\ 0 & -1 & 2 & -1 \\ -1 & 0 & -1 & 2 \end{bmatrix} \tag{3.11}$$

with eigenvalues $0, 2, 2$ and 4. The smallest eigenvalue $\gamma_1 = 0$ is associated with the synchronized manifold, and the other two are transverse to it. Putting together that the MLE is negative for $g_e\gamma \gtrapprox 0.2670$, and that 2 is the smallest eigenvalue associated with the transverse mode, we conclude that for $g_e \gtrapprox 0.133$ the synchronized solution is stable.

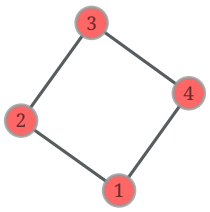

Figure 3.2: Undirected network with $N = 4$ nodes, which is used to exemplify the stability of complete synchronization for identical Izhikevich neurons.

Fig. 3.3 depicts the synchronization error, which is computed as $\text{Err} = \langle \sum_j^N |\bar{\mathbf{x}} - \mathbf{x}^j| \rangle_t$ where $\bar{\mathbf{x}}$ is the average state for the nodes in the networks, and $\langle \cdot \rangle_t$ represents the average on time. We notice a good agreement with the result given by the MSF analysis.

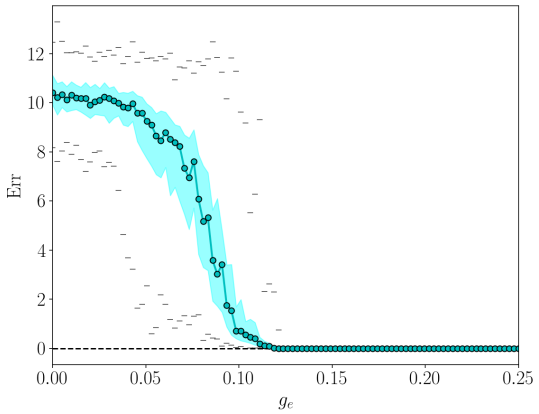

Figure 3.3: Synchronization error for a network of $N = 4$ Izhikevich neurons (3.2) with electrical coupling. It goes to zero at $\sigma \approx 0.133$, in conformity with the MSF. The solid line represents the average of 100 realizations, the shaded area represents the first and third quartiles, and the grey dashes represent the maximum and minimum values.

3.2.2 Chemical Coupling

We now study the synchronization of an Izhikevich network with chemical synaptic coupling between nodes. The chemical synapses that node i receives from every other node j are modeled by the sigmoidal function B_i [94]

$$B_i = g_c(x^i - v_s)\sum_{j=1}^{N} A_{ij}\zeta(x^j), \tag{3.12}$$

where v_s is the reversal potential, $\zeta(x) = [1 + \exp(-\epsilon(x - \theta))]^{-1}$, ϵ defines the slope of the sigmoidal function and θ is the synaptic firing threshold. Througout this study we set $v_s = 0$, $\epsilon = 7$ and $\theta = 0$. This set of parameters allows the chemical synapses to be both excitatory and inhibitory, since v_s lies inside the range of oscillation of the action potential x_i. This is the case for some classes of neurons, as discussed in [95, 96].

Note that this coupling term cannot be written as a function of the Laplacian matrix, instead we can write it in terms of the adjacency matrix. To obtain an equation analogous to (3.8), we introduce a few objects, which are defined in the Appendix A.1, together with the complete derivation of the equation for the dynamics of the network with chemical coupling, which is given by:

$$\dot{\mathbf{x}} = \mathbf{F}(\mathbf{x}) - g_c\mathbf{T}(\mathbf{x})[(A \otimes \mathbf{C})(\mathbf{x})] \, . \tag{3.13}$$

The synchronized solution, $\mathbf{x}^1 = \mathbf{x}^2 = ... = \mathbf{x}^N$, derived in the Appendix A.1 from Eq. (A.15) to (A.19), takes the form

$$\dot{\mathbf{x}}^s = \mathbf{F}(\mathbf{x}^s) - g_c k_n \mathbf{T}(\mathbf{x}^s)\mathbf{C}(\mathbf{x}^s) \, , \tag{3.14}$$

and it exists only if the number of links k_n is the same for all nodes [97]. Following the Pecora-Carroll analysis, we obtain the Master Stability Function for this case, and after we

diagonalize A we have

$$\dot{\eta} = \{[\mathbf{I}_N \otimes (D\mathbf{F}\big|_{\mathbf{x}^s} - g_c k_n D\mathbf{H}\big|_{\mathbf{x}^s}\mathbf{K}(\mathbf{x}^s))] - g_c \Gamma^A \otimes \mathbf{T}(\mathbf{x}^s) D\mathbf{C}\big|_{\mathbf{x}^s}\}\eta \,. \tag{3.15}$$

Where Γ^A is a diagonal matrix with eigenvalues of A as entries. The complete derivation of this equation, which is analogous to Eq. (3.10), is given in Appendix A.1 and it was first derived by Checco et al. [97]. As an example, we consider the network of $N = 4$ nodes, depicted in Fig. 3.2, with an adjacency matrix given by

$$A = \begin{bmatrix} 0 & 1 & 0 & 1 \\ 1 & 0 & 1 & 0 \\ 0 & 1 & 0 & 1 \\ 1 & 0 & 1 & 0 \end{bmatrix} \tag{3.16}$$

The adjacency matrix Eq. (3.16) has an eigenvalue $\gamma_1 = 2$ associated with the synchronized solution, so we need to calculate the MLE for the remaining eigenvalues $\{0, 0, -2\}$. Figure 3.4 shows the MLE of Eq. (3.15), which is positive for the range studied. Our calculation for the synchronization error in Fig. (3.5) shows good agreement with the MLE , i.e., we verified that the network does not synchronize with chemical coupling.

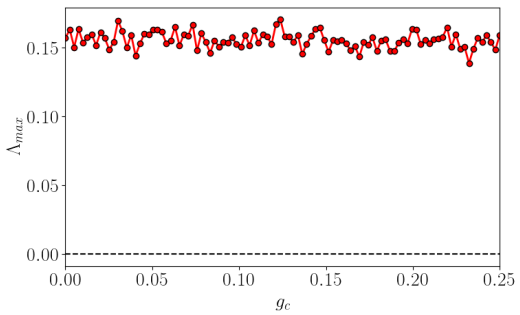

Figure 3.4: Maximum Lyapunov exponent transversal to the synchronization manifold for $N = 4$ Izhikevich neurons with chemical coupling.

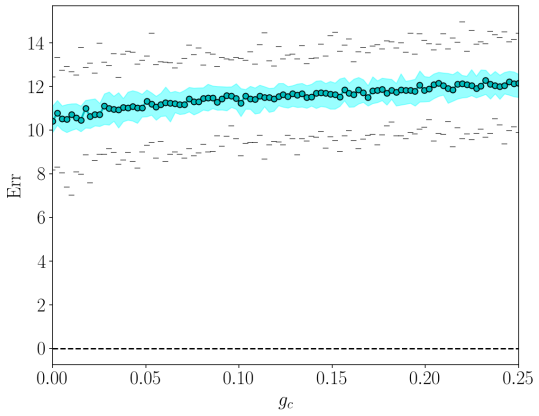

Figure 3.5: Synchronization error for a network of $N = 4$ Izhikevich neurons (3.2) with chemical coupling. As expected from the MSF analysis, the system does not synchronize. The solid line represents the average of 100 realizations, the shaded area represents the first and third quartiles and the grey dashes represent the maximum and minimum values

3.2.3 Chemical and Electrical Coupling

Finally, we study the effect of both electrical and chemical coupling on synchronization. In this case, the evolution of the network is given by

$$\dot{\mathbf{x}} = \mathbf{F}(\mathbf{x}) - g_e L \otimes \mathbf{G}(\mathbf{x})) - g_c \mathbf{T}(\mathbf{x})(A \otimes \mathbf{C})\mathbf{x} \,. \tag{3.17}$$

For the sake of simplicity, we consider that both interactions depend on the same diagonalizable adjacency matrix, i.e., $L = D - A$, and that every node has the same number of neighbors k_n. Combining the results of previous sections, we write the variational equation for the perturbations to the synchronized state as

$$\delta\dot{\mathbf{x}} = \{[\mathbf{I}_N \otimes (D\mathbf{F}\big|_{\mathbf{x}^s} - g_c k_n D\mathbf{H}\big|_{\mathbf{x}^s}\mathbf{K}(\mathbf{x}^s))] - g_e L \otimes D\mathbf{G}\big|_{\mathbf{x}^s} - g_c A \otimes \mathbf{T}(\mathbf{x}^s) D\mathbf{C}\big|_{\mathbf{x}^s}\}\delta\mathbf{x} \,. \tag{3.18}$$

Since L and A commute, we can diagonalize both simultaneously, yielding

$$\dot{\eta} = \{[\mathbf{I}_N \otimes (D\mathbf{F}\big|_{\mathbf{x}^s} - g_c k_n D\mathbf{H}\big|_{\mathbf{x}^s}\mathbf{K}(\mathbf{x}^s))] - [g_e \Gamma^L \otimes D\mathbf{G}\big|_{\mathbf{x}^s} - g_c \Gamma^A \otimes \mathbf{T}(\mathbf{x}^s) D\mathbf{C}\big|_{\mathbf{x}^s}]\}\eta \,. \tag{3.19}$$

where Γ^L and Γ^A are diagonal matrices with eigenvalues of L and A respectively as entries.

Once again, we take a network of $N = 4$ neurons, with electrical and chemical coupling given by $g = g_e = g_c$, and represented by the adjacency matrix (3.16). Thus, the eigenvalues associated with transverse modes are $\{\gamma^A\} = \{0, 0, 2\}$ from the adjacency matrix and $\{\gamma^L\} = \{2, 2, 4\}$, from the Laplacian matrix. We calculate the MLE of Eq. (3.19) as a function of g, and as shown in Fig. 3.6, the global synchronization pattern becomes linearly stable for $g \approx 0.13$. To confirm this result we calculate the synchronization error over 200 simulations, which is shown in Fig. 3.7, and find that it does not go to zero when the MLE becomes negative.

We notice that the synchronization error only vanishes around $g \approx 0.16$, and for values below that, the system can either synchronize or not. To better understand these results, we calculate the synchronization error for different initial conditions, for $g = 0.155$. While the y-variables are set to -101, we partitioned the network into two distinct clusters according to their x-variables. The range of x-variables spans from 1 to -1, resulting in initial conditions that are either orthogonal, represented as $\pm[1, -1, 1, -1]$, or parallel to the synchronized manifold, denoted as $\pm[1, 1, 1, 1]$, within the $y = -101$ plane. The value $y = -101$ corresponds to an approximate value for y in the range of x we selected.

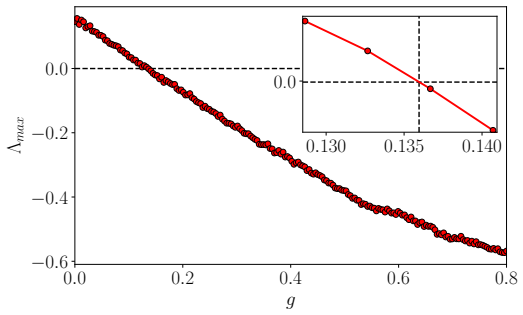

Figure 3.6: Maximum Lyapunov exponent transversal to the synchronization manifold for $N = 4$ Izhikevich neurons with electrical and chemical coupling.

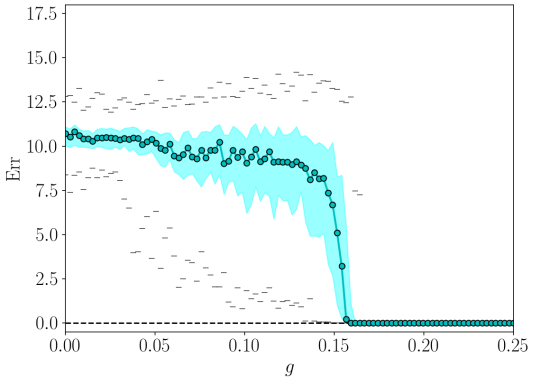

Figure 3.7: Synchronization error for $N = 4$ with electrical and chemical coupling. The solid line represents the average of 200 realizations, the shaded area represents the first and third quartiles, and the grey dashes represent the maximum and minimum values.

As we see in Fig. 3.8 (a) for $g = 0.155$, depending on the initial conditions, the system can end up in different solutions, a characteristic of multistable systems [98]. For simplicity, we differentiate synchronized solutions from non-synchronized solutions by setting a threshold at Err$= 0.05$, which are represented by white and black dots respectively. Moreover, the different solutions are intertwined in a complex way. This type of basin of attraction is often called a riddled basin, and can be the cause for the divergence between the MLE and the

synchronization error results [87]. Figure 3.8 (b) shows an inset of Fig. 3.8 (a), where we see that synchronized solutions are intertwined with non-synchronized in a similar way as in Fig. 3.8 (a) even though the domain is reduced.

Besides that, it is usually assumed that the presence of riddled basins of attraction is related to the MLE approaching zero from below, as discussed in [63, 99]. A similar result, where the system fails to exhibit synchronization when the MLE approaches zeros from above was reported by [87] but the presence of the riddled basin was not investigated.

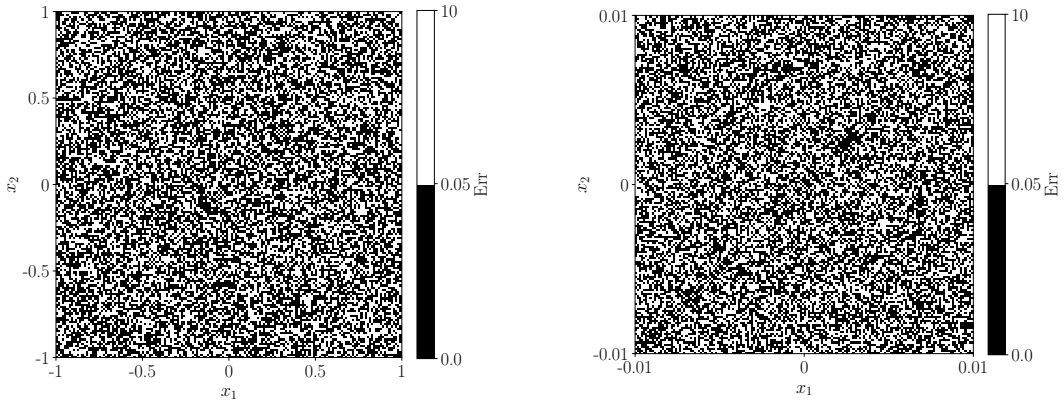

Figure 3.8: Riddled basin of attraction in (x_1, x_3) plane for $g = 0.155$, calculated with 10.24×10^4 initial conditions in (a) $x_1, x_2 \in [1, -1]$ and (b) $x_1, x_2 \in [0.01, -0.01]$. Solutions that reach a final state with a synchronization error $Err > 0.05$ are marked as white dots; otherwise, they are marked as black.

To better understand the basin of attraction, we calculate the uncertainty exponent α, which as defined in [100, 101], measures how small perturbations to initial conditions affect the final state of the system. To do so, we pick $M = 1000$ pairs of initial conditions with $g = 0.155$, iterating each to its final state. Each pair is separated by a distance d, i.e., $\mathbf{x} - \mathbf{x}' = d$. We then compare the final states of each initial condition to verify if there are pairs that end up in different states and therefore are *uncertain*. The fraction of the phase space that is uncertain obeys

$$f(\varepsilon) = \varepsilon^{\alpha} \tag{3.20}$$

with $\alpha < 1$. We record that the uncertainty exponent is related to the dimension of the phase space D as $\alpha = D - \delta$, where δ is the (capacity) dimension of the basin boundary [101].

We found an uncertainty exponent equal to $\alpha \approx 0.005$. As a result, even for extraordinarily small perturbations to the synchronized state, a fraction of them can grow and desynchronize the system. Moreover, using the $\alpha = D - \delta$, we find that the dimension of the basin boundary, $\delta \approx 7.995$, is close to the dimension of the state space. In conclusion, the obtained uncertainty exponent of $\alpha \approx 0.005$ suggests the presence of a riddled basin of attraction [98, 102].

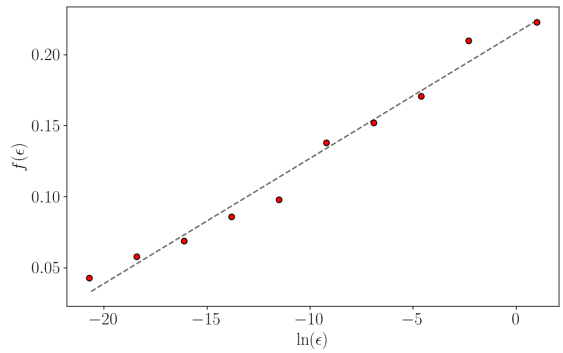

Figure 3.9: The fraction of pairs of initial conditions that converge to different basins of attraction, f, as a function of the distance between initial condition ε - Eq, (3.20). For $g = 0.1555$, the slope of the line that best fits the points yields an uncertainty exponent $\alpha = 0.005$.

3.3 Izhikevich Model: Partial Synchronization

3.3.1 Electrical Coupling

As mentioned in the first section, the electrical coupling can be written in terms of the Laplacian matrix. In this case, the variational equation concerning the linear stability around the cluster synchronized state (CSS) is given by [72]

$$\delta\dot{\mathbf{x}} = [\sum_{m=1}^{M}(E^m \otimes D\mathbf{F}\big|_{\mathbf{s}^m} - g_e(LE^m \otimes D\mathbf{G}\big|_{\mathbf{s}^m}))]\delta\mathbf{x} \tag{3.21}$$

where M is the number of clusters and E^m is an $N \times N$ diagonal indicator matrix for each cluster such that $E^m_{ii} = 1$ if i belongs to cluster m, and it is equal to zero otherwise. If we consider a CSS with M clusters, the dynamical evolution of such state is given by [81, 103]

$$\dot{\mathbf{x}} = (Z \otimes \mathbf{I}_q)\dot{\mathbf{s}}, \quad \text{where} \tag{3.22}$$

$$\dot{\mathbf{s}} = \mathbf{F}(\mathbf{s}) - g_e(L^\pi \otimes \mathbf{I}_q)\mathbf{G}(\mathbf{s}) \tag{3.23}$$

and Z is the $N \times M$ indicator matrix which encodes the cluster state configuration $Z : Z_{ij} = 1$ if node i is part of cluster C_j and $Z_{ij} = 0$ otherwise. $\mathbf{I}_q$ is an $q \times q$ identity matrix, where q is the dimension of the isolated dynamical system, $q = 2$ in our case. The state of each cluster is encoded in the $M \times q$-dimensional vector $\mathbf{s}$. If the quotient network Laplacian L^π satisfies the condition [82]

$$LZ = ZL^\pi\,, \tag{3.24}$$

where $L^\pi = (Z^T)^{-1}Z^TLZ = Z^+LZ$ and Z^+ is the left Moore-Penrose of pseudoinverse Z [104, 105], then the partition encoded by Z is said to be an Equitable External Partition (EEP) [82]. In this case, the network is divided into M clusters in such way that the number of connections from nodes in a cluster C_i to nodes in a cluster C_j depends only on i, j with $i \neq j$. The quotient network dynamics is a coarse-grained version of the original network,

where each cluster becomes a node and the weights between these nodes are the out-degrees between clusters in the original network [81, 83].

Again, we start our example with a network of Izhikevich neurons coupled through electrical synapses. Consider a network with the following Laplacian matrix

$$L = \begin{bmatrix} 2 & 1 & 0 & 1 & 0 & 0 & 0 & 0 \\ 1 & 2 & 0 & 1 & 0 & 0 & 0 & 0 \\ 0 & 0 & 1 & 1 & 0 & 0 & 0 & 0 \\ 1 & 1 & 1 & 5 & 1 & 1 & 0 & 0 \\ 0 & 0 & 0 & 1 & 3 & 0 & 1 & 1 \\ 0 & 0 & 0 & 1 & 0 & 3 & 1 & 1 \\ 0 & 0 & 0 & 0 & 1 & 1 & 3 & 1 \\ 0 & 0 & 0 & 0 & 1 & 1 & 1 & 3 \end{bmatrix} \tag{3.25}$$

and a CSS with indicator matrix Z given by $M = 5$ cluster, 3 with 2 nodes, and 2 with one:

$$Z = \begin{bmatrix} 1 & 0 & 0 & 0 & 0 \\ 1 & 0 & 0 & 0 & 0 \\ 0 & 1 & 0 & 0 & 0 \\ 0 & 0 & 1 & 0 & 0 \\ 0 & 0 & 0 & 1 & 0 \\ 0 & 0 & 0 & 1 & 0 \\ 0 & 0 & 0 & 0 & 1 \\ 0 & 0 & 0 & 0 & 1 \end{bmatrix} . \tag{3.26}$$

One can verify that this choice of L and Z satisfies (3.24) and therefore this cluster configuration is an EEP. A representation of such network is given in Fig. 3.10, where nodes of the same color represent a cluster. Putting this together, Eq. (3.23) reads

$$[\dot{\mathbf{x}}]^T = [\dot{\mathbf{s}}^1, \dot{\mathbf{s}}^1, \dot{\mathbf{s}}^3, \dot{\mathbf{s}}^4, \dot{\mathbf{s}}^5, \dot{\mathbf{s}}^5, \dot{\mathbf{s}}^7, \dot{\mathbf{s}}^7]^T . \tag{3.27}$$

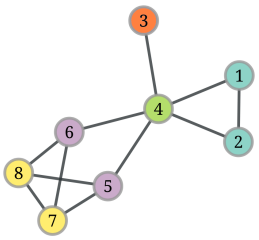

Figure 3.10: Network studied in this section, where the clusters are indicated with colors.

After block-diagonalizing the variational equation (3.21), we investigated the linear stability of the CSS with the following equation

$$\dot{\eta} = \Big[\sum_m Q^m \otimes D\mathbf{F}\big|_{\mathbf{s}^m} - g_e \Gamma^L Q^m \otimes D\mathbf{G}\big|_{\mathbf{s}^m} \Big] \eta \, . \tag{3.28}$$

Where $Q^m = V^{-1}E^m V$ is a block diagonal matrix and $\Gamma^L = V^{-1}LV$ is a diagonal matrix filled with eigenvalues of L. The orthogonal matrix that block-diagonalizes both E^m and L can be found using group theory [103], External Equitable Partitions (EEP's) [81] and Simultaneous Block Diagonalization (SBD) [84] approaches, resulting in the decoupling between modes within the cluster synchronized manifold and transverse to it.

To check if all transverse modes are damped, we calculated the maximum Lyapunov exponent of Eq. (3.28), which is given in Fig. 3.11 as a function of g_e.

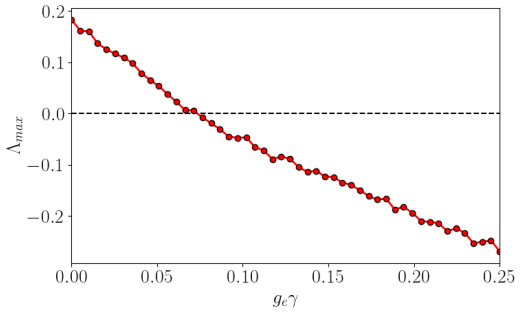

Figure 3.11: Maximum Lyapunov exponent transversal to the synchronization manifold for $N = 8$ Izhikevich neurons with electrical coupling under partial synchronization.

Fig. 3.12 shows the synchronization error of the cluster synchronization state as a function of g_e. The error is computed as $\langle |x^i(t) - x^i_m(t)| \rangle$, where we take an average both in time and over the neurons i in a cluster m. x^i_m is the average state for the neurons in the cluster to which node i belongs.

Fig. 3.11 and Fig. 3.12 show excellent agreement between the stability analysis and the synchronization error: the MLE associated with the transverse modes goes negative around $g_e \approx 0.073$, and the synchronization error vanishes around the same value.

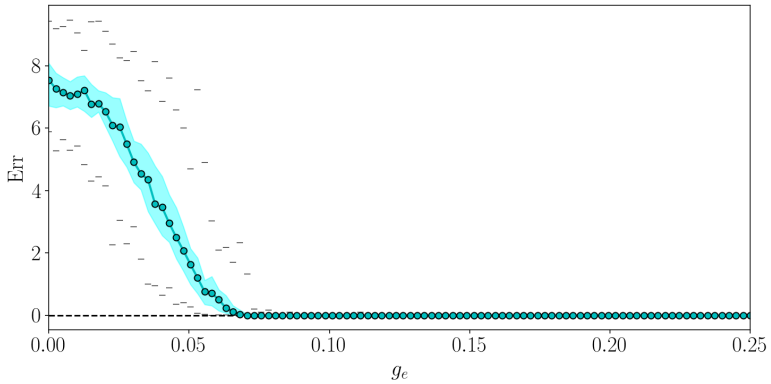

Figure 3.12: Synchronization error for Izhikevich model with electrical coupling, partial synchronization.

3.3.2 Chemical Coupling

We now extend the linear stability study of cluster synchronized states to networks with chemical coupling, which is mediated by the adjacency matrix of the network. Consider a network with N nodes and adjacency matrix A, given a CSS with M clusters encoded by an indicator matrix Z, the coarse-grained dynamics can be written as follows

$$\dot{\mathbf{x}} = (Z \otimes \mathbf{I}_q)\dot{\mathbf{s}}, \quad \text{where} \tag{3.29}$$

$$\dot{\mathbf{s}} = \mathbf{F}(\mathbf{s}) + g_e \mathbf{T}(\mathbf{s})(A^\pi \otimes \mathbf{C})(\mathbf{s}) \, . \tag{3.30}$$

If the adjacency matrix of the quotient network is given by $A^\pi = Z^+ A Z$, its diagonal entries correspond to self-loops in the quotient network whenever we have connections between nodes in the same cluster, and the partition encoded by Z is an External Partition (EP). For EPs the number of connections from nodes in a cluster C_i to nodes in a cluster C_j depends only on i, j [81].

The variational equation of Eq.(3.29) is

$$\delta\dot{\mathbf{x}} = \Big\{ \sum_{m=1}^{M} [E^m \otimes (D\mathbf{F}\big|_{\mathbf{s}^m} - g_c P R^m)] - [\sum_{m=1}^{M} (E^m A \otimes \mathbf{T}(\mathbf{s}^m))(\sum_{m=1}^{M} E^m \otimes D\mathbf{K}\big|_{\mathbf{s}^m})] \Big\} \delta\mathbf{x} \, . \tag{3.31}$$

And after block-diagonalizing Eq. (3.31), we obtain

$$\dot{\eta} = \Big\{ \sum_{m=1}^{M} Q^m \otimes [D\mathbf{F}\big|_{\mathbf{s}^m} - g_c \mathbf{G} R^m] - (Q^m \Gamma^A \otimes \mathbf{T}(\mathbf{s}^m)(\sum_{m=1}^{M} Q^m \otimes D\mathbf{K}\big|_{\mathbf{s}^m}) \Big\} \eta \, . \tag{3.32}$$

where we defined

$$\mathbf{G} = \begin{bmatrix} 1 & 0 \\ 0 & 0 \end{bmatrix} \quad \text{and} \quad R^m = \sum_{n=1}^{M} A^\pi_{mn} \zeta(x_n) \, . \tag{3.33}$$

Where ζ is the nonlinear operator defined in Appendix A.1. With these equations in hand, we now consider the network of the previous subsection, depicted in Fig. 3.10, and the same indicator matrix Z (Eq. (3.26)), with chemical coupling between neurons. In this case, the adjacency matrix is given by

$$A = \begin{bmatrix} 0 & 1 & 0 & 1 & 0 & 0 & 0 & 0 \\ 1 & 0 & 0 & 1 & 0 & 0 & 0 & 0 \\ 0 & 0 & 0 & 1 & 0 & 0 & 0 & 0 \\ 1 & 1 & 1 & 0 & 1 & 1 & 0 & 0 \\ 0 & 0 & 0 & 1 & 0 & 0 & 1 & 1 \\ 0 & 0 & 0 & 1 & 0 & 0 & 1 & 1 \\ 0 & 0 & 0 & 0 & 1 & 1 & 0 & 1 \\ 0 & 0 & 0 & 0 & 1 & 1 & 1 & 0 \end{bmatrix} \, . \tag{3.34}$$

Unlike the case with electrical coupling, here the CSS is not stable, as seen in Fig. (3.13), where the maximum Lyapunov exponent is positive in the range of g_c considered. This analysis is supported by the synchronization error of this case (Fig. 3.14), which is greater than 0 in the range of g_c studied.

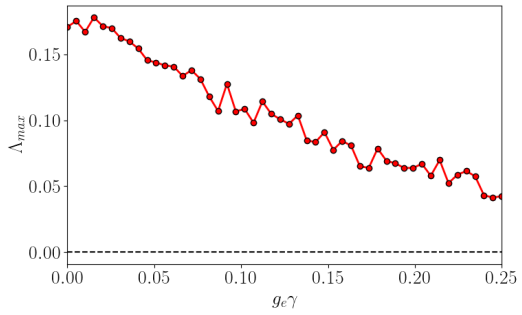

Figure 3.13: Maximum Lyapunov exponent transversal to the synchronization manifold for $N = 8$ Izhikevich neurons with chemical coupling partial synchronization (N=8).

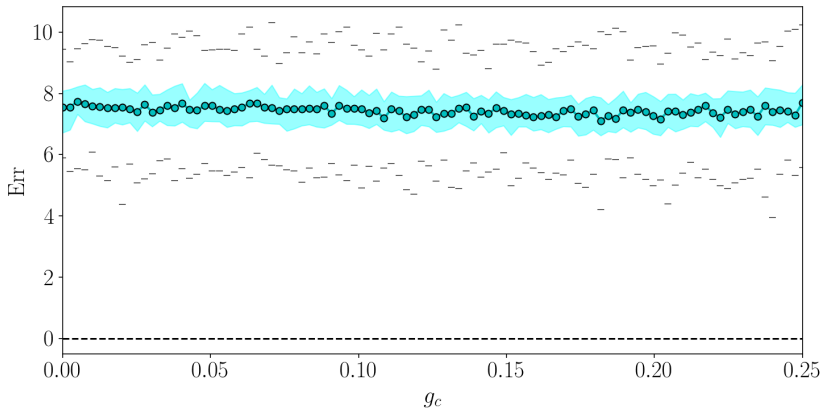

Figure 3.14: NEW Synchronization error for Izhikevich model with chemical coupling, partial synchronization (N=8).

3.3.3 Electrical and Chemical Coupling

In the case where the network admits both electrical and chemical coupling, the dynamics of the CSS is governed by

$$\dot{\mathbf{x}} = (Z \otimes \mathbf{I}_q)\dot{\mathbf{s}}, \quad \text{where} \tag{3.35}$$

$$\dot{\mathbf{s}} = \mathbf{F}(\mathbf{s}) - g_c\mathbf{T}(\mathbf{s})(A^\pi \otimes \mathbf{C})(\mathbf{s}) - g_e(L^\pi \otimes \mathbf{I}_q)\mathbf{G}(\mathbf{s}) \; . \tag{3.36}$$

where Z is the indicator matrix of the CSS state, A^π and L^π are the quotient adjacency and Laplacian matrices, and for the sake of simplicity we take $g_c = g_e = g$. Putting together the

results of the later subsections, the master stability function of a given CSS state can be written as

$$\dot{\eta} = \{ \sum_{m=1}^{M} Q^m \otimes [D\mathbf{F}\big|_{\mathbf{x}^m} - g_c \mathbf{G} R^m] - g_c (\sum_{m=1}^{M} Q^m \Gamma^A \otimes \mathbf{T}(\mathbf{x}^m)) (\sum_{m=1}^{M} Q^m \otimes D\mathbf{K}\big|_{\mathbf{x}^m}) - g_e \sum_{m=1}^{M} \Gamma^L Q^m \otimes D\mathbf{H}\big|_{\mathbf{x}^m} \} \eta \,. \tag{3.37}$$

We proceed with the analysis of the network in Fig. 3.10, with indicator matrix (3.26). The MLE of Eq. (3.37) is shown in Fig. 3.15, where we notice that the introduction of electrical coupling in the network seems to induce the CSS, since the MLE becomes negative for $g > 0.102$.

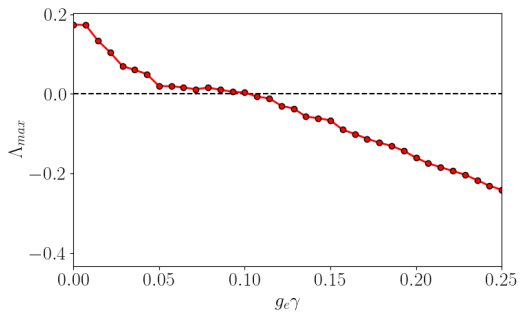

Figure 3.15: Maximum Lyapunov exponent transversal to the synchronization manifold for $N = 8$ Izhikevich neurons with chemical and electric coupling, partial synchronization.

The synchronization error is shown in Fig. 3.16, the dotted line represents the median over 100 simulations and the shaded area is the limit betwen first and third quartiles, and the grey lines represent the upper and lower limits of the errors. Although the lower bound of the synchronization error goes to zero around $g \approx 0.125$, we see that on average the system does not reach the synchronized solution. While the initial conditions are similiar to the ones used in Fig. 3.12, the introduction of chemical coupling results in a distinct outcome concerning the agreement between the MSF and synchronization error. This sensibility to perturbations is characteristic of multistable systems [98], and as discussed in [87], a riddled basin of attraction can be the cause for such behavior, which in turn may be a consequence of the discontinuity of the differential equation. A thorough understanding of this phenomenon needs intense research which is outside the scope of this work.

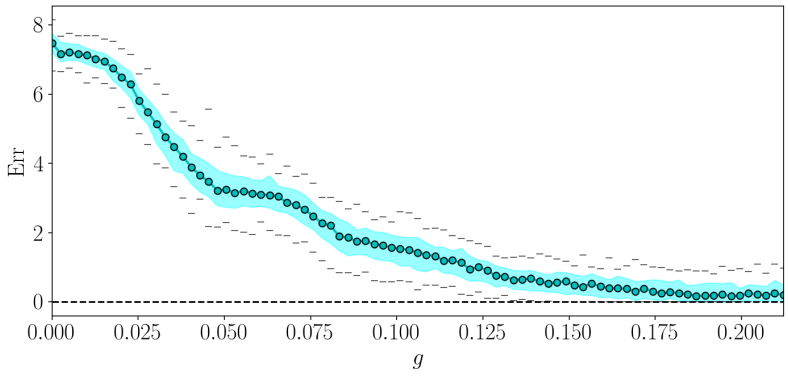

Figure 3.16: Synchronization error as a function of g for Izhikevich model with electrical and chemical coupling. The CSS considered is the one Fig. 3.10. The average over 150 runs, with nearly identical initial conditions, is depicted with its bounds.

To verify that, we consider adding a disturbance in only one direction transverse to the synchronized solution, which means perturbing only one cluster. For example, if we take the solution

$$\mathbf{x} = \begin{bmatrix} \mathbf{s}_1 \\ \mathbf{s}_1 \\ \mathbf{s}_3 \\ \mathbf{s}_4 \\ \mathbf{s}_5 \\ \mathbf{s}_5 \\ \mathbf{s}_7 \\ \mathbf{s}_7 \end{bmatrix}, \quad \text{and add} \quad \mathbf{p}_\perp = \alpha \begin{bmatrix} 0 \\ 0 \\ 0 \\ 0 \\ 1 \\ -1 \\ 0 \\ 0 \end{bmatrix} \otimes \begin{bmatrix} 1 \\ 1 \end{bmatrix}, \tag{3.38}$$

where α is a constant used to control the magnitude of the perturbation $\mathbf{p}_\perp$, we are pulling the first cluster out of synchronicity. Figure 3.17 (a) shows how the synchronization error is sensible to initial conditions for $g = 0.155$. We used the same method as in Fig. 3.8. To calculate Err, we consider initial conditions slightly perturbed as in Eq. (3.38). The initial conditions for $\mathbf{x}_{(5,6)} = [x^{(5,6)}, y^{(5,6)}]^T$ vary from $[1, 1]$ to $[-1, -1]$, which is equivalent to α varying from 1 to -1 in Eq. (3.38). Along the diagonal $\mathbf{x}_5 = \mathbf{x}_6$ the system is always synchronized. In the off-diagonal region, we have both synchronized and non-synchronized solutions. As in Fig. 3.8, we see that the basin is riddled with these two kinds of solutions. The same calculation is depicted in Fig. 3.17 (b), illustrating the riddle basin for $g = 0.195$. As anticipated from Fig. 3.16, the increased number of black dots signifies a higher proportion of points ending up in the synchronized basin.

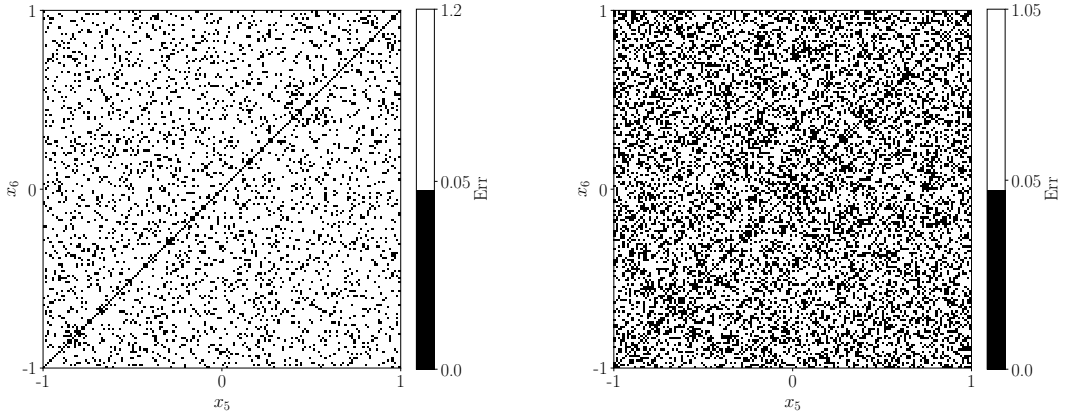

Figure 3.17: Riddled basin of attraction in (x_5, x_6) plane for $g = 0.155$. (a) is calculated with 10.24×10^4 initial conditions in $x_5, x_6 \in [1, -1]$. (b) same as (a) for $g = 0.195$.

The solutions found in Fig. 3.17 are shown in Fig. 3.18. The solution in panel (a) yields a synchronization error greater than the one in panel (b). We notice that in both cases, there are finite windows of time where the system goes off synchronization, however, the solution in panel (a) seems to display more and longer windows. This type of intermittence is similar to the one discussed in [106], and it is only found in the perturbed cluster formed by nodes 5 and 6, the remaining clusters stay synchronized throughout the simulation.

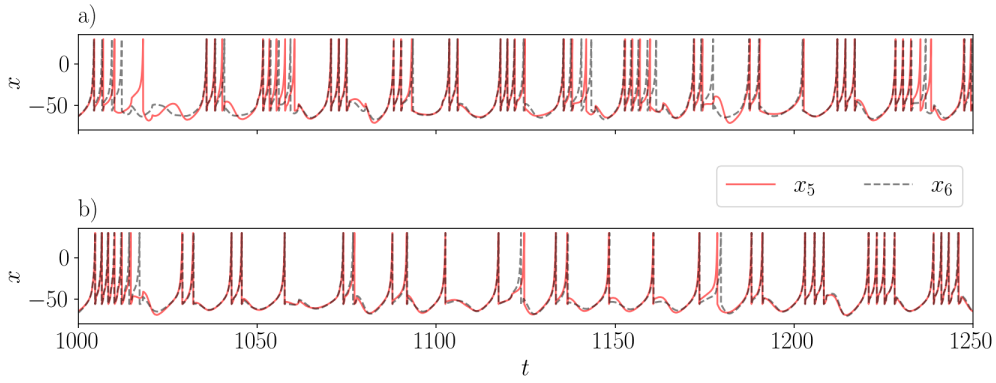

Figure 3.18: Time series of the x-variable from nodes 5 (solid red) and 6 (dashed black) for different initial conditions, both with $g = 0.155$. (a) Incomplete synchronization Err =, (b) .

To confirm the basin riddling, we compute the uncertainty exponent α. Again, we take a pair of initial conditions $\mathbf{x}, \mathbf{x}'$ such that the distance between the two is $\epsilon = |\mathbf{x} - \mathbf{x}'|$ and verify if the initial conditions are uncertain or not. For each distance ϵ, we simulate 1000 pairs of initial conditions and save the uncertain fraction $f(\epsilon)$. The result is plotted in Fig.

3.19, where the fitted line indicates an uncertainty exponent equal to $\alpha \approx 0.007$, and thus the basin dimension is equal to $d \approx 15.993$.

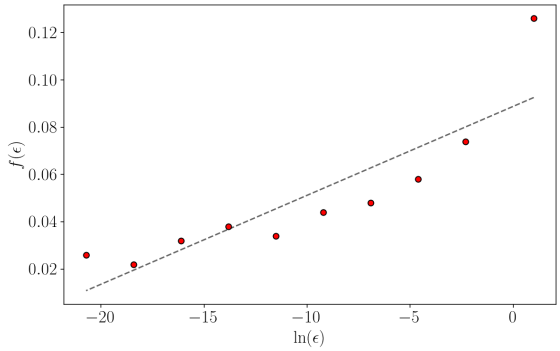

Figure 3.19: The fraction of pairs of initial conditions that converge to different basins of attraction, f, as a function of the distance between initial condition ε - Eq, (3.20). For $g = 0.1555$, the slope of the line that best fits the points yields an uncertainty exponent $\alpha = 0.007$.

3.4 Remarks

We have calculated the MSF of networks of Izhikevich neurons, considering global and cluster synchronized states with electrical and chemical coupling schemes. To do so, we combined the MSF formalism with the use of saltation matrices, which allow the calculation of Lyapunov exponents of systems with discontinuities such as the Izhikevich model. For the networks studied, we found that the synchronization error exhibits a nice agreement with the MSF analysis when only one type of coupling is considered. Moreover, the addition of electrical coupling to a network with only chemical coupling induces synchronization for both global and cluster-synchronized states. However, the presence of both coupling schemes yielded a riddled basin of attraction. Due to this, even in the range where the MSF is negative and with nearly identical initial conditions concerning the CSS, the system can end up in a non-synchronized state.

This mismatch between the results expected by the MSF and the real output of the network reinforces that having a negative MLE for the synchronized state is *necessary*, but it does not *guarantee* it. Moreover, we highlight that the MSF relies on knowledge of the network structure, i.e., the adjacency matrix A, such information is not usually available to us in real-world scenarios. Putting this together, the application of the MSF is not straightforward.

Motivated by these challenges, especially the lack of information regarding network structure, in the next part of this thesis, we will shift our focus toward addressing the problem of network inference. This shift in focus allows us to attempt to bridge the gap between theoretical models, such as the MSF, and the complexities of applying synchronization analysis to real-world networks.

Part III

Network Inference

4 Kalman filters

Before diving into the problem of network inference per se, in this chapter, we introduce the mathematical foundation of the Kalman filter, which will be a central method to deal with the inference problem.

4.1 From Tracking to Network Inference

Since its introduction in 1960 by Robert E. Kalman, the Kalman filter has been used in applications such as the tracking of the Apollo space program, the stock market, and global positioning system (GPS) receivers. But what is a filter? And why does someone need to use a filter in the first place? To answer these questions, let us first talk about a ubiquitous characteristic of sensors we use in our day-to-day lives: they are all noisy.

Assume that you are measuring the fruits at the grocery store with two scales, with the weight on one scale being 200g and that on the other scale being 220g. If we assume that the scales are equally accurate, you would estimate the weight to be 210g. On the contrary, if you knew that one scale was more accurate than the other, you would still combine both measures, but you would like the final estimate closer to the measure with higher accuracy.

So this is the idea behind *filtering*: combining pieces of information from a system to gain more knowledge than we would get from the isolated pieces. We want to use such filters because our sensors, the scales, the radars, the multimeters, etc., carry uncertainty with their measurements. Hence, to get a better idea of the system we are measuring, we want to combine the measurements with more pieces of information, which can be other measurements or prior information regarding the system, such as a mathematical model that describes it.

This idea is closely related to *Bayesian probability*, which determines what is likely to be true given prior information. Putting it in a simple way, The Kalman filter is a *Bayesian filter*, an algorithm that combines measurements coming from a noisy sensor with predictions from a mathematical model of the system under study.

As pointed out by Zarchan, while the mathematical formulation of the Kalman filter can be

challenging to grasp, it has been applied even without a profound understanding of its mathematical derivation [107]. In this chapter, we aim to stay in the middle. We do not aim to provide a complete review and derivation of the Kalman filter, but rather, we will describe its main features, with a focus on implementation.

With this in mind, we will first discuss the g-h filter, a type of Bayesian filter. Through the use of a tracking example, we will introduce the main concepts of filtering. Next, we will move to the Kalman filter, which closely resembles the g-h filter. Finally, we will comment on the challenges that arise when applying the Kalman filter to nonlinear systems. This will lead us to the Unscented Kalman filter, which was designed specifically to address such issues. Finally, we will comment on how we can use all of this knowledge to address the problem of network inference.

4.2 The g-h Filter

The g-h filter can be seen as a simplified version of more robust filters like the Kalman filter. Derived by Shumway and Stoffer [108], it shares many features with these filters. Here we use it to introduce the key concepts of filtering. First, let us introduce some terminology. We refer to the dynamical system that we want to estimate simply as *system*. The actual value of the system is said to be *hidden*, as we can not directly observe it, we can only obtain a *measurement* from it. As we commented before measurements carry some uncertainty with them.

To mathematically model the system, we use a *process model*. If our system of interest is a moving object, the process model can be as simple as distance $=$ velocity $\times$ time. We use the process model to make *predictions* of the system from the current state. To our process model, and therefore to its predictions, we associate a *process error*, which reflects the errors in the model.

Assume that we are tracking a target, which is moving radially away or towards a radar, which is responsible for tracking it. For simplicity, we consider that this problem is one-dimensional and that the target's velocity is constant. Hence, we can propose the following process model for our system:

$$\mathbf{x}_{k+1} = \begin{bmatrix} \text{position}_k \\ \text{velocity}_k \end{bmatrix} = \begin{bmatrix} x_k + T\dot{x}_k \\ \dot{x}_k \end{bmatrix} \tag{4.1}$$

where x denotes the position of the target and $\dot{x}$ its velocity at time k and T is the time between measurements of the radar. So, given a measurement at time k, we can make a prediction for time $k+1$ using our process model Eq. (4.1). Our goal is to combine our prediction with the measurement at time $k+1$, which will yield a better estimate of the system state. The measurement and the prediction are the pieces of information we have, as in the scale example, our estimate should lie between the two. Ideally, we would like to know if our predictions are more or less precise than our measurements. Heuristically, we want our equation to be

$$\text{estimate} = \text{prediction} + g(\text{measurement} - \text{prediction}) \tag{4.2}$$

where the difference between the measurement and the prediction is known as *residual*. g serves as the scaling factor in our estimation process, commonly referred to as the *gain*. The point of including it in our equation is to regulate the influence of predictions and measurements on final our estimation. Setting $g = 0$ results in the exclusion of measurements, relying solely on predictions. Conversely, choosing $g = 1$ implies relying exclusively on information from measurements.

Starting with a measurement at time $k - 1$, we can assume that this is our first estimation. We can make a prediction about the state for time k using our process model. Following the notation on [109], we write this prediction as $x^*_{k,k-1}$. Putting this together with Eq. (4.2) and our measurement at time k, y_k, we can write the estimate for the position as

$$x^*_{k,k} = x^*_{k,k-1} + g(y_k - x^*_{k,k-1}) \, . \tag{4.3}$$

Where the second subscript tells us the time of the measurement used in the estimation. Using this strategy to estimate the velocity, we want our equation to be something like

$$\text{new velocity} = \text{old velocity} + h\Big(\frac{\text{measurement} - \text{prediction}}{T}\Big) \, , \tag{4.4}$$

where h, like g is a scaling factor in our estimation. By combining the latter with the Eq. (4.3), we get

$$\dot{x}^*_{k,k} = \dot{x}^*_{k,k-1} + h\Big(\frac{y_k - x^*_{k,k-1}}{T}\Big) \, . \tag{4.5}$$

Note that here, we assume that we have an estimation from the velocity using the time $k - 1$, which requires knowing the displacement between times $k - 2$ to $k - 1$, and if it is not available one can use a guess at the first estimation. Moreover, the estimations will always lie between the measurement and the prediction from the model. Whether it will be closer to the measurement or to the prediction will depend on the choice of the parameters g and h. An exemplary discussion with well-crafted examples about the effect of g and h in the estimations can be found in [110].

Putting together these equations, and our process model, we can write the *update* equations of our filter as

$$x^*_{k+1,k} = x^*_{k,k-1} + T\dot{x}^*_{k+1,k} + g(y_n - x^*_{k,k-1}) \tag{4.6}$$

$$\dot{x}^*_{k+1,k} = \dot{x}^*_{k,k-1} + \frac{h}{T}(y_n - x^*_{k,k-1}) \tag{4.7}$$

The g-h filter, defined by the equations above, gets its name from the two scaling factors used in the estimations. The difference between more sophisticated filters and the g-h filter is how these scaling factors are defined. In fact, the g-h filter is actually a family of filters, and all of them follow the same logic. How one defines g or h usually depends on the problem in question, and, for a deeper discussion on it, the reader is referred to [109]. One possible definition involves a scaling factor that, between measurements and predictions, provides an estimation closer to the one with the least uncertainty. As we will explore in the next section, this holds true for the Kalman filter.

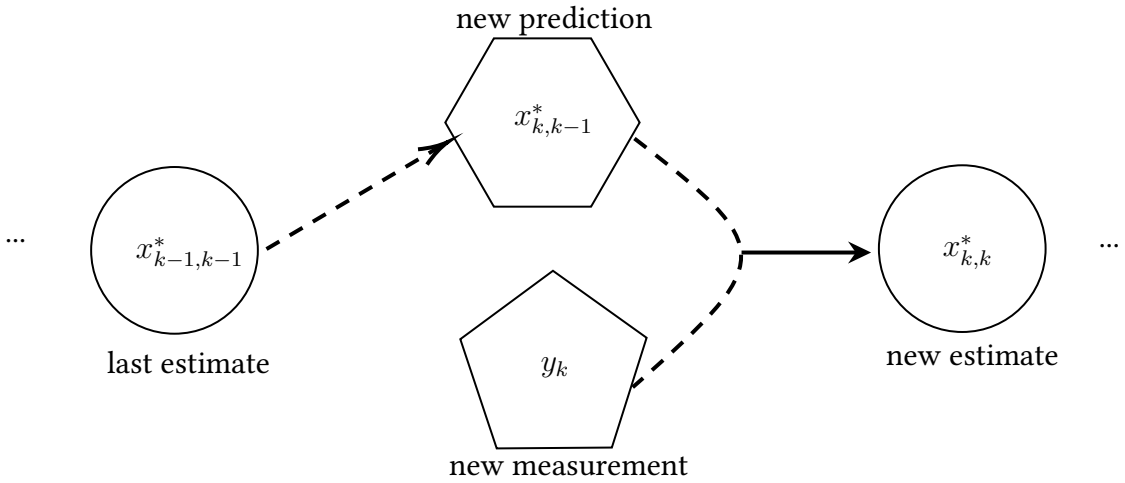

Figure 4.1: Diagram of the g-h filter. The second subscript tells us the time of the measurement used in the estimation.

4.3 The Kalman Filter

As mentioned in the previous section, the Kalman filter operates as a g-h filter. Consequently, it relies on a dynamic interplay between predictions and measurements. In this section, we will explore how the principles of Bayes' rule and the mathematics of Gaussian distributions work within the Kalman filter, contributing to enhancing the estimations.

The idea is to reproduce the math done in the previous section using Gaussians to represent our variables. The use of Gaussian will make the math involving the prediction and update steps easier. Before we continue, it comes in hand to remember that Bayes' rule states that

$$P(A|B) = \frac{P(B|A) \cdot P(A)}{P(B)} = \text{posterior} = \frac{\text{likelihood} \times \text{prior}}{\text{normalization}} \,. \tag{4.8}$$

It relates an event A and an observation B, both described by probabilities $P(A)$ and $P(B)$, with a probability of having A given B, also known as conditional probability $P(A|B)$. Bayes rule will let us improve our estimation (*posterior*) by combining our predictions (*priors*) with our measurements. To do so, we evaluate how probable the measurement is under the assumption that the prediction is true (*likelihood*). As will be seen, the Bayes rule comes into play in the update equations of the Kalman filter.

Once again, we will study a one-dimensional tracking problem, as it facilitates the introduction of mathematical formalism and the understanding of the filters' mechanism. So, assume that we have a radar and its measurements reflect the spatial separation between the radar and the object, indicating how far away the object is from the radar.

We start with a measurement $\mathbf{y}_k$, which can be described by a Gaussian distribution with mean $\mu_\mathbf{y}$ and variance $\sigma_\mathbf{y}$. As we did before, we can use our process model to make a prediction $\mathbf{x}_{k+1,k}$ of our target:

$$\mathbf{x}^*_{k+1,k} = \mathbf{x}^*_{k,k} + f(\mathbf{x}^*_{k+1,k}) \tag{4.9}$$

where $\mathbf{x}_{k+1,k}$ is described by a Gaussian distribution with mean μ_* and variance σ_* where f is the state propagation function for $\mathbf{x}$, which in this case is simply

$$f(\mathbf{x}) = \text{velocity} \times \text{time between measurement} \tag{4.10}$$

Note that we can simply add the probabilistic position $\mathbf{x}_{k,k}$, which is the last estimate, with the probabilistic displacement between times k to $k+1$, $f(\mathbf{x}_{k+1,k})$ because we are assuming that we are dealing with Gaussian distributions. Now, given our prediction and a new measurement $\mathbf{y}_{k+1}$, we can use the g-h filter strategy (Eq. (4.6). But, how can we improve our estimations by combining both pieces of information? Using that

$$P(\text{prediction}|\text{measurement}) \propto P(\text{measurement}|\text{prediction})P(\text{prediction}) \ , \tag{4.11}$$

and relating these probabilities with the process model and a measurement function [1], Kalman derived the following *update* equation:

$$\mathbf{x}^*_{k+1,k+1} = \mathbf{x}^*_{k,k-1} + K(\mathbf{y}_{k+1} - \mathbf{x}^*_{k+1,k}) \ , \tag{4.12}$$

where K, also known as the Kalman gain, is

$$K = \frac{\sigma_*^2}{\sigma_*^2 + \sigma_{\mathbf{y}}^2} \tag{4.13}$$

and determines the weight given to the measurement and the prediction when updating the state estimate. And, as we will see when we move to matrix notation, is closely related to the *likelihood*.

First, we write the dynamical system into matrix notation,

$$X_{k+1} = \Phi X_k \tag{4.14}$$

where

$$X_k = \begin{bmatrix} x_k \\ \dot{x}_k \end{bmatrix} \quad \text{is the state vector, and} \quad \Phi = \begin{bmatrix} 1 & T \\ 0 & 1 \end{bmatrix} \tag{4.15}$$

is the state transition matrix for constant velocity. Explicitly, we have

$$X_{k+1} \begin{bmatrix} x_{k+1} \\ \dot{x}_{k+1} \end{bmatrix} = \begin{bmatrix} 1 & T \\ 0 & 1 \end{bmatrix} \begin{bmatrix} x_k \\ \dot{x}_k \end{bmatrix} = \begin{bmatrix} x_k + T\dot{x}_k \\ \dot{x}_k \end{bmatrix} \tag{4.16}$$

Assuming randomness in our system, we get

$$X_{k+1} = \Phi X_k + U_n \tag{4.17}$$

where [2]

$$U_k = \begin{bmatrix} 0 \\ u_k \end{bmatrix} \tag{4.18}$$

[1] For a complete derivation of the Kalman update equation from a Bayes perspective, the reader is referred to [111].

[2] Where the choice for U_k and N is arbitrary, both were chosen following the example discussed in [109].

where we assume that u_n is given by a Gaussian noise. This yields

$$\begin{bmatrix} x_{k+1} \\ \dot{x}_{k+1} \end{bmatrix} = \begin{bmatrix} x_k + T\dot{x}_k \\ \dot{x}_k + u_k \end{bmatrix} . \tag{4.19}$$

Now, we write an equation to describe the measurement process, these equations are known as the observation system equation:

$$Y_k = MX_k + N_k \tag{4.20}$$

where $M = \begin{bmatrix} 1 & 0 \end{bmatrix}$ is the observation matrix, $N = [\nu_k]$ [3] is the observation error, and $Y = [y_k]$ is the measurement matrix. Note that

$$[y_k] = \begin{bmatrix} 1 & 0 \end{bmatrix} \begin{bmatrix} x_k \\ \dot{x}_k \end{bmatrix} + [\nu_k] = \begin{bmatrix} x_k + \nu_k \end{bmatrix} \tag{4.21}$$

x_k is the real position at the time k, we can not observe it. When we measure it, we get y_k, which is x_k plus the error in our measurement.

Hence, in matrix form, our predictions can be written as

$$X^*_{k+1,k} = \Phi X^*_{k,k} \tag{4.22}$$

where

$$X^*_{k,k} = \begin{bmatrix} x^*_{k,k} \\ \dot{x}_{k,k} \end{bmatrix} \quad \text{and} \quad X^*_{k+1,k} = \begin{bmatrix} x^*_{k+1,k} \\ \dot{x}^*_{k+1,k} \end{bmatrix} \tag{4.23}$$

the update equation is given by

$$X^*_{k,k} = X^*_{k,k-1} + K_k(Y_k - MX^*_{k,k-1}) \tag{4.24}$$

which is known as the Kalman filtering equation, and the tracking-filter constants g and h are encoded by the matrix

$$K_k = \begin{bmatrix} g_k \\ \dfrac{h_k}{T} \end{bmatrix} \tag{4.25}$$

which explicitly, is given by

$$K_k = S^*_{k,k-1}M^T[R_k + MS^*_{k,k-1}M^T]^{-1} \tag{4.26}$$

where the prediction equation is,

$$S^*_{k,k-1} = \Phi S^*_{k-1,k-1}\Phi^T + Q_k \tag{4.27}$$

where Q_k is the dynamic model noise covariance matrix, R_k is the observation noise covariance matrix and $S^*_{k-1,k-1}$ is the corrector equation, given by

$$S^*_{k-1,k-1} = [I - K_{k+-1}M]S_{k-1,k-2} \tag{4.28}$$

[3] See footnote 2 in page 40.

Physically, the matrix $S^*_{k,k-1}$ is an estimate of our accuracy in predicting the target position and velocity at time k based on the measurements made at time $k-1$ and before. Here, $S^*_{k,k-1}$ is the covariance matrix of the state vector $X^*_{k,k-1}$.

The matrix R_k is related to the accuracy of the radar measurements.

The matrix Q_k gives the magnitude of the random system dynamics model uncertainty.

Note that, as we dealt with Gaussian distributions, this set of equations allows us to update our prediction and the uncertainty associated with them. And, on top of that, the Kalman gain enhances the updates by valuing information with less uncertainty.

To better understand its meaning, let's take Eq. (4.26) and solve it for our study case. For the sake of simplicity, we omit the subscripts. Then covariance matrices are

$$S^* = \begin{bmatrix} \sigma^2_{x^*} & 0 \\ 0 & \sigma^2_{\dot{x}^*} \end{bmatrix} \tag{4.29}$$

$$R = [\sigma^2_\nu] \tag{4.30}$$

and the measurement matrix is $M = [1 \quad 0]$. Putting it together, we have

$$K = \begin{bmatrix} \sigma^2_{x^*} & 0 \\ 0 & \sigma^2_{\dot{x}^*} \end{bmatrix} \begin{bmatrix} 1 \\ 0 \end{bmatrix} \left([\sigma^2_\nu] + \begin{bmatrix} 1 & 0 \end{bmatrix} \begin{bmatrix} \sigma^2_{x^*} & 0 \\ 0 & \sigma^2_{\dot{x}^*} \end{bmatrix} \begin{bmatrix} 1 \\ 0 \end{bmatrix} \right)^{-1}, \tag{4.31}$$

which yields

$$K = \begin{bmatrix} \sigma^2_{x^*} \\ 0 \end{bmatrix} \left([\sigma^2_\nu] + [\sigma^2_{x^*}] \right)^{-1} = \begin{bmatrix} \dfrac{\sigma^2_{x^*}}{\sigma^2_{x^*} + \sigma^2_\nu} \\ 0 \end{bmatrix}. \tag{4.32}$$

To better understand its meaning, we can take two limits keeping Eq. (4.26) in mind:

$$\text{if} \quad \sigma_* \gg \sigma_\nu \quad \text{then} \quad K \approx \begin{bmatrix} 1 \\ 0 \end{bmatrix} \tag{4.33}$$

this means giving less weight to predictions since it is much more uncertain than our measurements. Conversely,

$$\text{if} \quad \sigma_* \ll \sigma_\nu \quad \text{then} \quad K \approx \begin{bmatrix} 0 \\ 0 \end{bmatrix} \tag{4.34}$$

yields an estimation that depends more on the predicted state, since it has a smaller uncertainty.

One of the key assumptions in the results obtained by Kalman was that the process under study was described as linear, both $f(\mathbf{x})$ and Φ. So, how can we apply it to nonlinear systems like Izhikevich neurons? Fortunately, the Kalman filter formalism has been extended to nonlinear systems. In the next section, we will discuss one of the most robust versions of the Kalman filter designed to handle nonlinearities - the Unscented Kalman filter.

4.4 The Unscented Kalman Filter

The formalism developed by Kalman that we revised in the last section uses linear equations, both the process model and the measurements are assumed to be described by linear processes. This poses a problem since nonlinearities are a natural part of our world. At first, one may suggest that a simple linearization of our equations can solve this problem. Following the example in [110], let's consider a distribution that represents a two-dimensional state,

$$\text{with mean} \quad \mu = \begin{bmatrix} 0 \\ 0 \end{bmatrix} \quad \text{and covariance matrix} \quad \Sigma = \begin{bmatrix} 32 & 15 \\ 15 & 40 \end{bmatrix} \tag{4.35}$$

and the nonlinear system $\mathbf{f} = [f_1, f_2]$

$$f_1(x, y) = x + y \tag{4.36}$$
$$f_2(x, y) = 0.1x^2 + y^2 \tag{4.37}$$

which, when linearized takes the form

$$\bar{f}_1(x, y) = 2 \tag{4.38}$$
$$\bar{f}_2(x, y) = 0.2x + 2y\ . \tag{4.39}$$

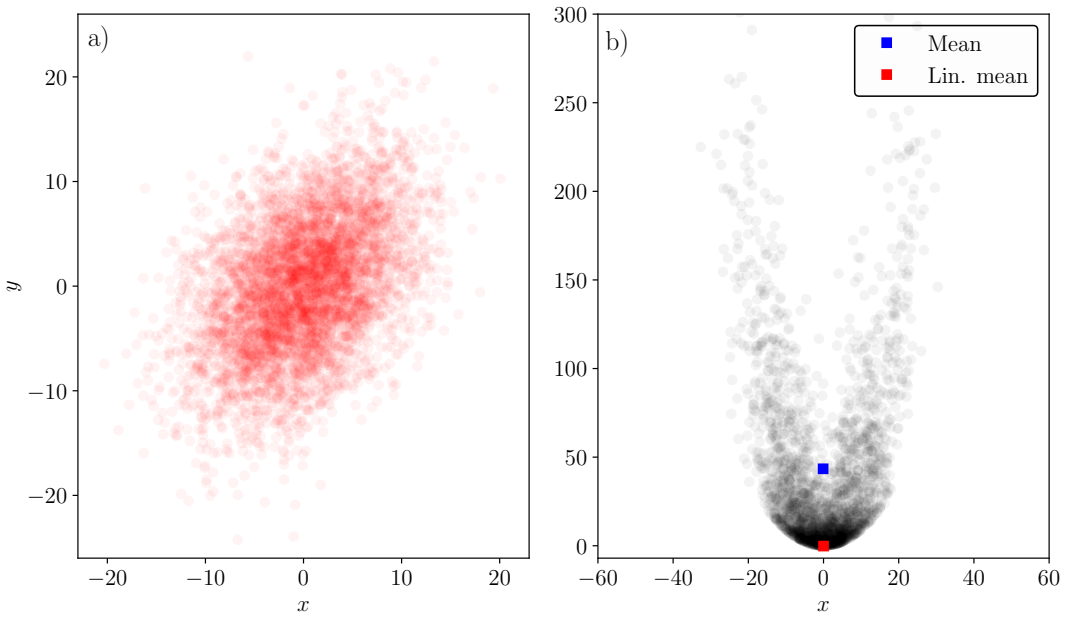

Figure 4.2: (a) Distribution of five thousand points according to (4.35). (b) Result of applying the nonlinear system (4.37) to the distribution. The real mean is represented by the blue square. The mean calculated from the linearized version (4.39) is shown in red.

How bad does our transformation get when we use this linearization? To answer this question, we draw 5000 points from our distribution Eq. (4.35) in Fig. 4.2 (a). Then, pass

these points through the nonlinear system $\mathbf{f}$. The result is shown in panel (b), and the new mean is marked with the blue square. Note mean obtained by using the linearized version of the system is marked in red. The difference between the two means is $|\text{Mean} - \text{Lin. mean}| \approx 44.96$. Hence, a filter relying on this linearization would diverge after a few iterations.

Then, one can argue that a reasonable transformed distribution can be obtained if we sample a sufficient number of points from our original distribution. This strategy, known as the *Monte Carlo* approach, is key for a family of filters known as particle filters. The problem with such an approach lies in defining "enough", as evaluating the nonlinear system for a large number of points can result in a very slow algorithm. Remember that one of the key aspects of the Kalman filter is the representation and update of our beliefs as distributions, which are encoded by their means and covariances.

To overcome this problem, Julier proposed to sample only a few points from the original distribution, claiming that when passed by the nonlinear system, these few points would yield a decent new distribution [112]. More details about the properties of these points, known as *sigma points*, can be found in the Appendix B. For now, we focus on the qualitative aspect of them. Let's see how they compare against the result of sampling 1000 points from our original distribution. Such a comparison is shown in Fig. 4.3, where we plot both the sigma points and the ensemble of points sampled from the distribution (Eq. (4.35)) in panel (a). As we see in panel (b), the means obtained with the sigma points is close to the one obtained by the ensemble of points, using 200 times fewer points.

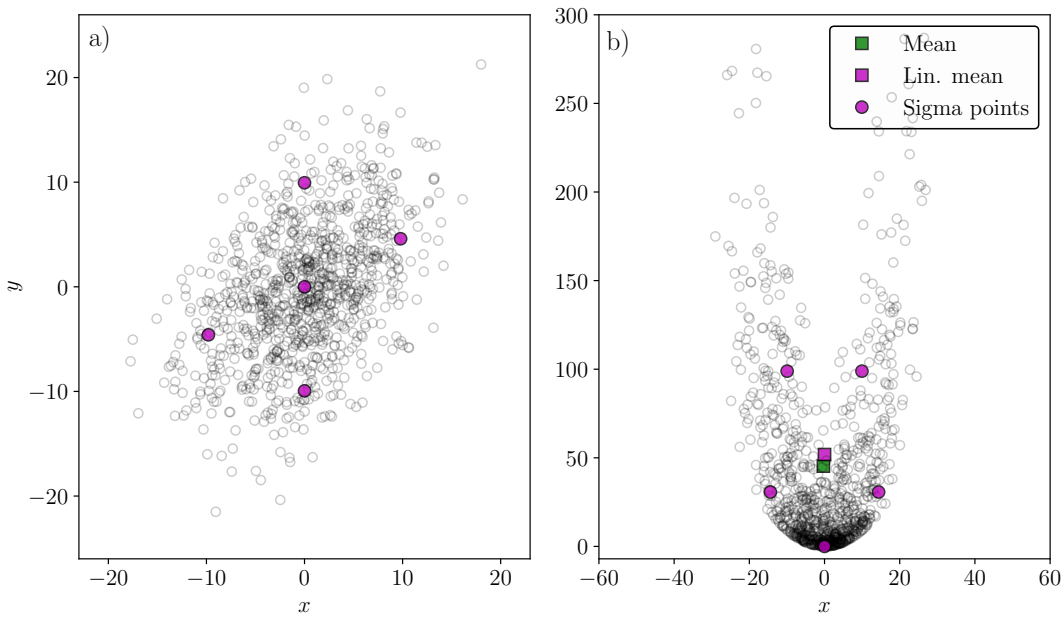

Figure 4.3: (a) One thousand points drawn from the distribution (4.35) plotted in greys and five sigma points plotted in magenta. (b) The transformed distribution and the transformed sigma points. The mean of the new distribution is plotted in green.

The idea behind the sigma points is that "it is easier to approximate a probability distribution than it is to approximate an arbitrary nonlinear function or transformation" [113]. Recall that the Kalman filter uses the mean and the covariance in its update rule. This implies that by utilizing a set of sigma points χ, we can derive a set of transformed points $\psi = \mathbf{f}(\chi)$. Each point is represented by a Gaussian distribution, and once we have that, all the formalism derived in the last Section 4.3 can be used. This method is known as the Unscented Kalman filter.

4.5 Estimating Parameters with the Kalman Filter

So far, we have seen that the Kalman filter is capable of tracking the variables that describe a hidden state $\mathbf{x}$. And, fortunately, we can use it to tackle nonlinear problems using methods like the unscented transformation. All of this is done by combining the data from measurements with a model of the system under study, while the variables of the model are kept fixed. But, what if we want to estimate a variable from our model? This question was first studied by Trudinger et al. [114], where they used the KF to estimate variables of a biogeochemical model.

With this in mind, recall that the equations for a network of diffusively coupled oscillators can be written as (2.1)

$$\dot{\mathbf{x}}^i = \mathbf{F}(\mathbf{x}^i) + \sum_j K_{ij}\mathbf{H}(\mathbf{x}^k - \mathbf{x}^i) \,, \tag{4.40}$$

where $K_{ij} = \sigma A_{ij}$ is the product of the coupling strength with the adjacency matrix of the network. Then, we can try to estimate not only the parameters of our oscillator model $\mathbf{F}$, but also the connectivity (or structure) of our network, by estimating the K_{ij} elements. This idea was studied by Forero et al. [60], using Rösslers oscillators. Inspired by them, in this part of the thesis we will apply it to the Izhikevich model [3].

To do so, we can assume that the parameters of our model are also variables that we want to estimate. Our state takes the form

$$\mathbf{x} = (x_1, ..., x_n, y_1, ..., y_n, p_1, ..., p_n) \,, \tag{4.41}$$

where p_n is the n-th parameter we want to estimate. Plus, we assume that our parameters do not change with time and that they are modeled by $\dot{p}_i = 0$ without any process noise. Hence, the covariance matrix $\mathbf{Q}$ associated with our process model is given by [60, 114]

$$\mathbf{Q} = \begin{bmatrix} Q_{11} & \cdots & Q_{1n} & 0_{1,n+1} & \cdots & 0_{1,n+q} \\ Q_{21} & \cdots & Q_{2n} & 0_{2,n+1} & \cdots & 0_{2,n+q} \\ Q_{31} & \cdots & Q_{3n} & 0_{3,n+1} & \cdots & 0_{3,n+q} \\ \vdots & \vdots & \vdots & \vdots & \ddots & \vdots \\ Q_{n1} & \cdots & Q_{nn} & 0_{n,n+1} & \cdots & 0_{n,n+q} \\ 0_{n+1,1} & \cdots & 0_{n+1,n+1} & 0_{n,n+1} & \cdots & 0_{n,n+q} \\ \vdots & \vdots & \vdots & \vdots & \ddots & \vdots \\ 0_{n+q,1} & \cdots & Q_{n+q,n} & 0_{n+q,n+1} & \cdots & 0_{n+q,n+q} \end{bmatrix} . \tag{4.42}$$

Then, all the formalism derived in Sections 4.3 and 4.4 can be used to estimate the parameters of the process model under study. In the next chapter, we will apply this methodology to infer the parameters of an isolated Izhikevich neuron, and also to infer the connectivity of networks of Izhikevich neurons.

5

Parameter and Network Inference with the Unscented Kalman Filter

This chapter presents the results of the research conducted in collaboration with Antonio J. Pons[1], Hilda A. Cerdeira[2], Cristina Masoller[1], and Giulio Tirabassi[1]. The paper, titled *Parameter and coupling estimation in small networks of Izhikevich's neurons*, was previously published in Chaos, Volume 33, Issue 4.

5.1 Introduction

One of the main challenges that neuroscience has faced for a long time is the determination of brain topology, which is morphologically diverse and complex. On top of that, the elements that form the brain network, the neurons, are also diverse and complex. Neurons show reproducible nonlinear responses to stochastic stimuli [115]. Hence, they can be modeled as stochastic nonlinear dynamical systems [116].

Mathematical models of the whole brain or just of a tiny fraction of millions of neurons, as well as information-based data analysis techniques are powerful tools for shedding light on the relationship between brains' dynamics and topology [117]. However, a realistic estimation of the models' states and parameters is a very difficult challenge, and different approaches based on control theory have been developed [118]. A well-known method is the Kalman filter. [119–121]

The Kalman filter allows inferring optimal parameters of a model given uncertain observations, balancing the effects of measurement noise, disturbances, and model uncertainties and has found applications in many fields of science and technology [122]. In neuroscience, the Kalman filter has been used, for example, for decoding brain signals for brain-machine interfaces [123–125]. It has also been used to estimate the parameters of neural models [126–131]. However, the models that have been considered, such as the

[1]Departament de Fisica, Universitat Politecnica de Catalunya, Terrassa, España
[2]Instituto de Física Teórica, Universidade Estadual Paulista, São Paulo, Brasil

Morris–Lecar or the Hodgkin-Huxley, contain a large number of parameters that make a systematic exploration of the parameter space unfeasible.

Here we study the Izhikevich model (IM) [132] because it reproduces many important properties of biological neurons and, at the same time, has a small number of parameters and is computationally low-cost[133]. Therefore, the Izhikevich model is an ideal candidate for a systematic exploration of the parameter space allowing a study of small ensembles of coupled neurons. Besides, the IM was recently studied in the context of network inference by Garcia et al. [134], where they studied how the inference depends on the topology of the network.

We analyze under which conditions a nonlinear version of the Kalman filter, the Unscented Kalman Filter (UKF) [112, 135], provides a good estimation of the IM parameters and we discuss its main limitations. We show that the UKF is able to recover the parameters of an isolated neuron and the external current that is exciting its activity. We also show that the UKF is able to do so even in the case of time-dependent input currents. Then, we study small networks with different topologies, with both electrical and chemical couplings, and show that UKF is able to recover the topology of the network using observations of the dynamic variables, assuming the coupling strength, electrical or chemical, and all the internal parameters are known.

5.2 Methods

5.2.1 Model

As posed in Eq. (3.1), the state of an Izhikevich neuron i is fully specified by two state variables. x_i represents the neuron membrane potential and y_i represents the membrane recovery variable accounting for the activation of the ionic currents. For completeness, we write the equations again:

$$\begin{aligned} \dot{x}_i &= 0.04\,x_i^2 + 5x_i + 140 - y_i + I + E_i + C_i + \sigma_Z \xi_i^x \\ \dot{y}_i &= a\,(b\,x_i - y_i) + \sigma_Z \xi_i^y \end{aligned} \tag{5.1}$$

with the after-spike reset condition:

$$\text{if} \quad x_i > 30, \quad \text{then} \begin{cases} x_i \to c, \\ y_i \to y_i + d. \end{cases} \tag{5.2}$$

The last term in Eq. (5.1) represents random fluctuations and we refer to it as dynamic or process noise. ξ_i^x and ξ_i^y represent Gaussian white noises with zero mean and unity variance. σ_Z is the noise strength and for simplicity, it is the same for x and y. For a system of N neurons, the dynamical noise can be thought as a random $2N$-dimensional vector with zero mean and covariance matrix $\bar{Q}_Z = \sigma_Z^2 \mathbf{I}$, where $\mathbf{I}$ is the identity matrix.

The electrical coupling between neurons is described by a system of ordinary first-order differential equations with different levels of detail that represent various degrees of

Table 5.1: Dimensionless parameters[132] used in the simulations of the IM.

a	b	c	d	$I\,(I_s)$	g_e	g_c	μ_s	ϵ	θ	α	ω	σ_Z	σ_ν
0.2	2	-56	-16	-99	$(0, 0.1)$	$(0, 0.05)$	35	7	0	3	0.15	0.025	0.15

Table 5.2: Initial guesses of the parameters used by the UKF.

a	b	c	d	$I\,(I_s)$	g_e	g_c	α	ω	σ_P
$(0.01, 0.9)$	$(0.01, 5)$	$(-70, -40)$	$(-25, -5)$	$(-94, -104)$	$(0, 0.1)$	$(0, 0.05)$	$(1, 5)$	$(0.1, 1)$	0.01

physiological descriptions [136]. Here we consider the simplest coupling, namely linear diffusive coupling, E_i is given by

$$E_i = g_e \sum_{j=1}^{N} A^e_{ij}(x_j - x_i)\ . \tag{5.3}$$

where g_e is the coupling conductance and A^e_{ij} are the coefficients of the adjacency matrix: $A^e_{ij} = 1$ whenever neuron i is connected to neuron j, otherwise $A^e_{ij} = 0$.

The coupling C_i comprises inputs delivered through chemical synapses to neuron i from all other neurons in the network. It is given by[94]:

$$C_i = g_c(x_i - \mu_s) \sum_{j=1}^{N} A^c_{ij}\zeta(x_j). \tag{5.4}$$

g_c is the synaptic coupling strength, μ_s is the reversal potential, and the sigmoid function $\zeta(x)$ is defined as

$$\zeta(x_j) = [1 + \exp(-\epsilon(x_j - \theta))]^{-1}, \tag{5.5}$$

where ϵ controls the slope of the sigmoidal function and θ is the synaptic firing threshold. This function represents the activation of the postsynaptic current when a presynaptic neuron sends an action potential, that is when x becomes larger than θ. Hence, a neuron i receives a chemical synapse from a neuron j only if x_j is larger than θ. The value of the prefactor $(x_i - \mu_s)$ in Eq. 5.4 controls whether the synapses are inhibitory or excitatory. In particular, we chose μ_s such as $(x_i - \mu_s) < 0$, that is inhibitory chemical synapses. The numerical values of all parameters are given in Table 5.1[88].

Throughout this study, we use symmetric A^e matrices and asymmetric A^c matrices, because the electrical coupling is symmetric, but the chemical coupling is directional. Here we only focus on a proof-of-concept demonstration of the UKF's ability to infer coupling topology; in the future, we plan to study the more challenging (and realistic) scenario of heterogeneous, excitatory, or inhibitory chemical synapses.

5.2.2 The Unscented Kalman Filter

The Kalman filter makes a prediction for the future state of a system, resulting from the state evolution of a dynamical model, and then corrects it using the information coming

from experimental data. Even though it was originally developed for linear systems, soon it was extended to include nonlinearities. Different nonlinear extensions were created. The UKF is one nonlinear version of the filter which has a good performance in terms of computational effort.

Following the notation in Forero et al. [60], we consider the extended state $\bar{\mathbf{u}}$ as the vector given by the state variables x_i and y_i of the N neurons $(i = 1, ..., N)$ and all the parameters we want to retrieve. Our process model to be employed in the UKF will be $\bar{\mathbf{u}}_{k+1} = \bar{\mathbf{a}}(\bar{\mathbf{u}}_k)$, where k is the timestep index. $\bar{\mathbf{a}}$ is given by the deterministic part of Eq. (5.1) for the state variables and is the identity operator for the parameters, as we assume they are constant. In the UKF algorithm, the estimation for $\bar{\mathbf{u}}_{k+1}$ predicted using the stochastic dynamical model is corrected by an experimental piece of data. However, this experimental data will necessarily have some uncertainty resulting from the measurement process, represented by a measurement function. Our measurement function is a selection of the state variables from the extended vector $\bar{\mathbf{u}}_k$, which are perturbed by the measurement noise with standard deviation σ_ν: $x_i \to x_i + \sigma_\nu \chi_i^x$ and $y_i \to y_i + \sigma_\nu \chi_i^y$, where χ represents Gaussian white noise. Thus, the covariance matrix of the measurement noise will be $\bar{Q}_\nu = \sigma_\nu^2 \mathbf{I}$. The covariance of the estimated state is $P = \sigma_P \mathbf{I}$, which is evolved by the UKF algorithm from the initial values given in Table 5.2.

5.2.3 Implementation

To generate the synthetic data that we use as experimental observations, we numerically solve Eq. (5.1) with a fourth-order Runge-Kutta method, an integration step of $dt = 0.01$, and the parameters reported in Table 5.1, keeping the measurements with sampling rate equal to the integration step. With these parameters, single (uncoupled) neurons display chaotic dynamics[88], as depicted in Fig. 5.1(a). Initial conditions for the simulations were drawn from a normal distribution centered at a fixed point of Eq. (5.1) in the case of no coupling, $(-56.25, -112.5)$, with a standard deviation equal to 1.

Throughout the study, we employ the UKF implemented by the Python package *FilterPy*[137]. The confidence in the process model ($\bar{Q}_Z$) and the measurements ($\bar{Q}_\nu$) are kept constant (see Table 5.1). An initial transient of 50000 timesteps was discarded in all runs.

The UKF requires an initial guess for the parameters that we want to estimate. To test the robustness of the UKF, we consider different initial guesses for each run, which are selected from a uniform distribution in the ranges given in Table 5.2.

To quantify the performance of the UKF in recovering the adjacency matrix $g_e A^{KF} = G_e^{KF}$, we use the Euclidean distance between the original and the recovered matrix:

$$D(G, G^{KF}) = \sqrt{\sum_{i,j} (G_{i,j} - G_{i,j}^{KF})^2} \,. \tag{5.6}$$

We quantify the performance using the full coupling matrix G, as we want to test not only if the UKF is able to reconstruct the connectivity, but also if it can devise the correct coupling strength without being informed that the coupling strength is the same for all links. Also,

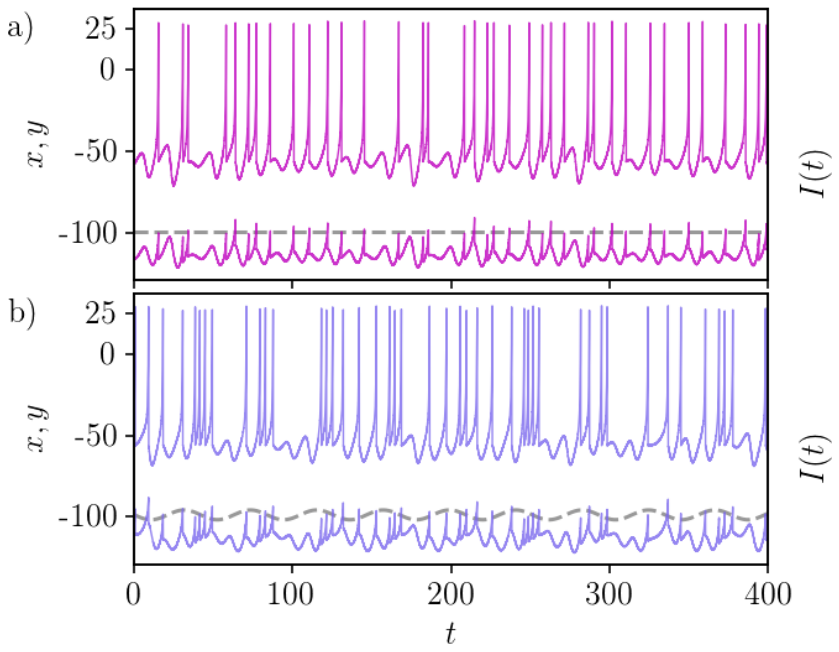

Figure 5.1: (a) Time evolution of the variables $x(t)$ (upper curve) and $y(t)$ (lower curve) of an isolated Izhikevich neuron, simulated with Eq. (5.1) with parameters given in Table 5.1. (b) Response to an external modulated current $I(t) = I_s + \alpha \sin(\omega t)$. In each panel, the current input is represented by the dashed line. The values of the parameters are given in Table 5.1.

we chose to use the Euclidean distance because it is a simple, straightforward measure to compare two graphs of weighted links with a single figure.

5.3 Results

5.3.1 Estimation of the parameters of a single neuron

First, we illustrate the effectiveness of the UKF in estimating the parameters of a single Izhikevich neuron. The parameters that we attempt to estimate are a, b, c, d, and I. Note that the parameters c and d only appear in the resetting dynamics, therefore the UKF can only update them in the event of a spike. Moreover, the equation for $\dot{y}$ contains a product ab, which can increase the uncertainty of the estimation. For example, an underestimation of a can compensate an overestimation of b. To avoid such problems, we estimated ab and a independently.

To recover the unknown parameters, we consider 100 simulated time series as input, each with a different initial parameter guess drawn uniformly from the intervals reported in Table 5.2. These intervals have been chosen because in those ranges the spiking of the neuron will be chaotic, which is a piece of information we can infer from the spike sequence. Results are shown in Fig. 5.2. For all cases, the real value of the parameter is within the range of the standard deviation. As the estimation of c and d is only updated

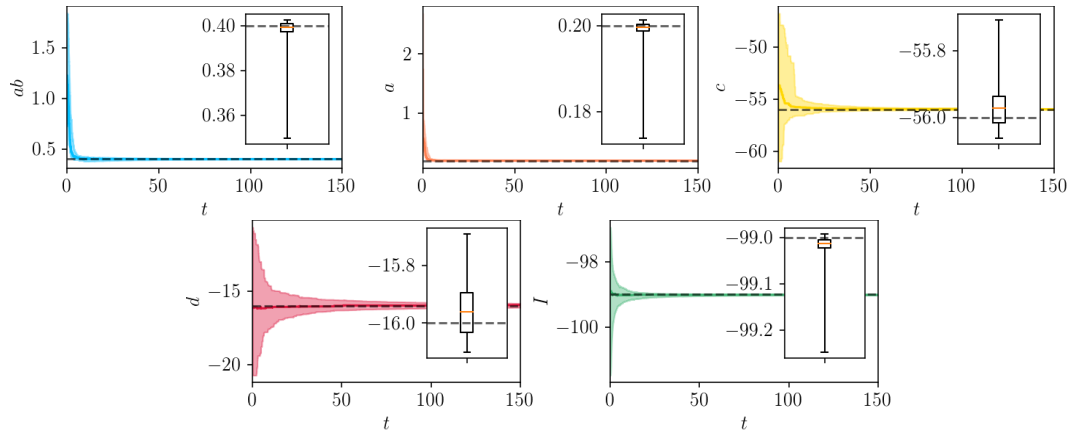

Figure 5.2: Parameter estimation for a single neuron as a function of the simulation time. The colored thick lines represent the median of the estimations computed from 100 runs. The shaded regions represent the first and third quartiles. The dashed lines mark the true values of the parameters. The inset in each subplot shows the distribution of the final estimations. The orange line is the median, the box marks the first and third quartiles and the upper and lower whiskers of the bars represent the maximum and minimum values. The parameter values are given in Table 5.1.

when the neuron spikes, the duration of the simulated time series required to obtain a reliable estimation is larger than for the other parameters.

We point out that using the UKF to estimate c and d is unnecessary because a direct estimation of these parameters can be done by checking the values of x and y after a spike.

Now, we test the estimation of time-varying parameters. Specifically, we consider a sinusoidal external current, $I(t) = I_s + 3\alpha \sin(\omega t)$, and estimate a, b and $I(t)$ (wrongly assuming that the current is constant). The effect of such a current on the neuron's dynamics is shown in Fig. 5.1(b), where we see that bursts of spikes are followed by periods of subthreshold oscillations. Since at constant I the Izhikevich model displays a great variety of dynamical behaviors including bursting [132], the inspection of the time series does not provide evidence of the presence of a sinusoidal input current.

The results of the parameter estimation are shown in Fig. 5.3. The recovered values of a and b are comparable to those obtained in the previous parameter estimation (see Fig. 5.2). The estimated value of I oscillates with a frequency equal to ω, suggesting that I is not constant.

Next, we substitute the expression of $I(t)$ in the model, Eq. (5.1), and separately estimate I_s, α and ω. In this case, we also need to include time as an additional dimension of the extended vector space, with dynamic equation $\dot{t} = 1$. The results of this approach are shown in Fig. 5.4. The UKF can estimate the correct parameters of the oscillation in the majority of cases. However, large departures from the correct values can be observed, which could be due to the fact that the model with constant I can produce similar output dynamics.

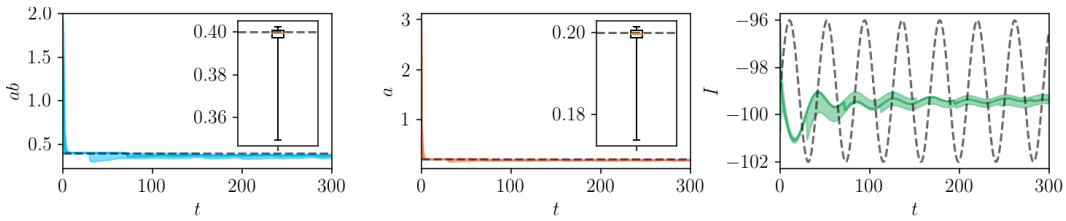

Figure 5.3: Parameter estimation for a single neuron with a time-dependent external current, which is modeled as a constant input. The colored thick lines represent the median of the estimations computed from 100 runs. The shaded regions represent the first and third quartiles. The dashed lines mark the true values of the parameters. The inset in each subplot shows the distribution of the final estimations. The orange line is the median, the box marks the first and third quartiles and the upper and lower whiskers of the bars represent the maximum and minimum values. The parameter values are given in Table 5.1.

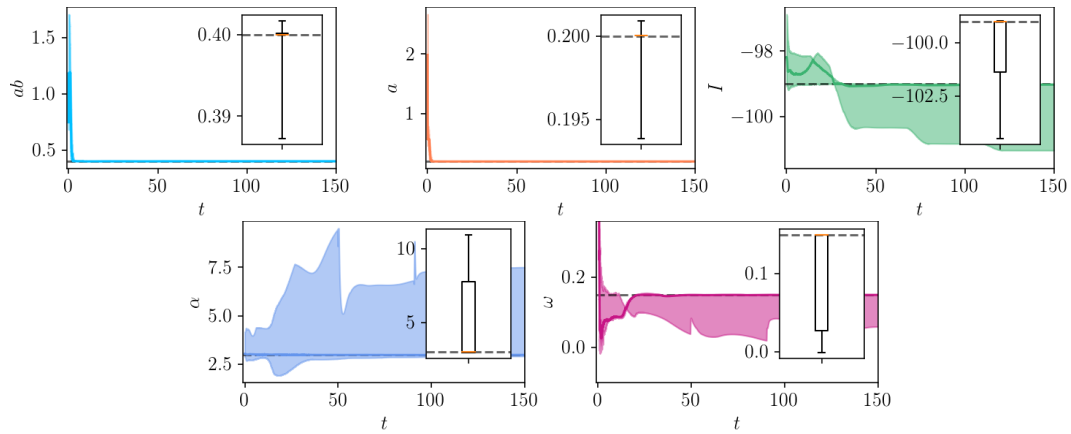

Figure 5.4: As Fig. 5.3, but explicitly modeling the input current as $I = I_s + \alpha \sin(\omega t)$. The colored thick lines represent the median of the estimations computed from 100 runs. The shaded regions represent the first and third quartiles. The dashed lines mark the true values of the parameters. The inset in each subplot shows the distribution of the final estimations. The orange line is the median, the box marks the first and third quartiles and the upper and lower whiskers of the bars represent the maximum and minimum values. The parameter values are given in Table 5.1.

5.3.2 Estimation of network connectivity

We now consider small networks of Izhikevich neurons, and we investigate the capacity to recover the adjacency matrix A assuming that the coupling strengths, g_e and g_c, and all the internal parameters are known. Of course, this is not possible in experiments, and we use these assumptions as a first step for testing the neural network reconstruction problem using the UKF approach: if, given these assumptions, the network cannot be inferred, we can conclude that the UKF approach is not useful; on the other hand, if we succeed in reconstructing the network with these assumptions, as a next step we will test the UKF approach having less information, for instance, assuming a different neuron model, unknown internal parameters, unknown coupling strengths. We run the UKF algorithm, considering each element of A as an additional dimension of the extended vector $\bar{\mathbf{u}}$.

We consider networks with $N = 4$ neurons, which can be seen as building blocks of bigger networks. However, we must keep in mind that complex systems usually display emergent collective behavior when the number of elements is large enough, and therefore, while the UKF algorithm may succeed in reconstructing the topology of a small network, the collective behavior that may emerge for a large enough number of neurons (and/or a large number of parameters to be inferred), will probably cause the UKF algorithm to fail. Therefore, the study of the role of the network size is of course important, and additional work is planned, that will be reported elsewhere.

The network topologies are shown in Appendix C, see Figs. C.1 and C.2. The simulated time evolution of the membrane potentials of all nodes for each network topology are also shown in Figs. C.1 and C.2. The network dynamics differ in their level of synchronization. First, we consider electrical coupling only ($g_c = 0$), such that the adjacency matrix is symmetric and we only need to determine its upper triangular elements $G_e = g_e A^e$ with $g_e = 0.05$.

The results for the different topologies are displayed in Fig. 5.5, where we see that the UKF gives an excellent estimation of G_e, as the Euclidean distance $D(G_e, G_e^{KF})$ approaches 0.

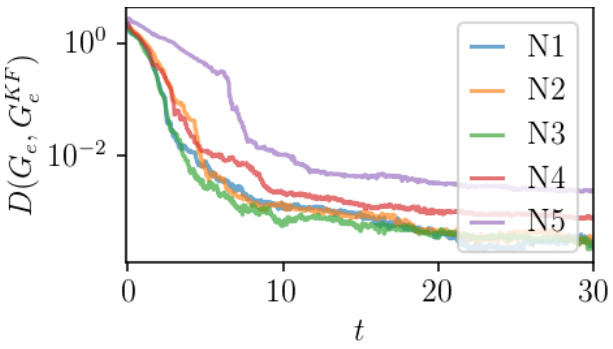

Figure 5.5: Evolution of the distance D, which represents the Euclidean distance between real coupling matrix G_e and the estimated one G_e^{KF}. N1, N2, N3, N4, and N5 represent different topologies, as shown in Fig. C.1. For all topologies D decreases sharply at first, then it saturates below 10^{-2}. The coupling strength is $g_e = 0.05$ and the dynamics displayed by the networks are shown in Fig. C.1.

To study the effect of chemical synaptic coupling in the UKF estimation, we add direct links between some nodes in the formerly symmetric networks, as shown in Appendix C, Fig. C.2.

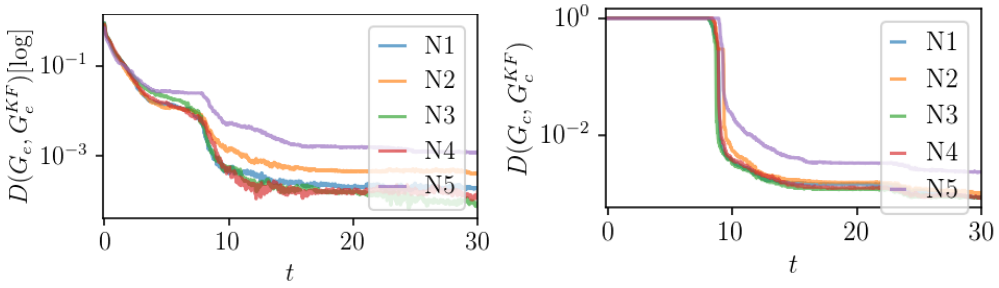

Figure 5.6: Evolution of the distance D for (a) electrical coupling and (b) chemical coupling, with coupling strengths $g_e = 0.1$ and $g_c = 0.05$. The distance between the original and the estimated adjacency matrices, $D(G, G^{KF})$, decreases sharply with simulation time, saturating below 10^{-2} for all network topologies. The dynamics displayed by the networks are shown in Fig. C.2.

We estimate two adjacency matrices, one encoding electrical coupling, $g_e A^e = G_e$ with $A^e = (A^e)^T$, and the other encoding chemical coupling, $g_c A^c = G_c$ with $A^c \neq (A^c)^T$. We chose $g_e = 0.1$ and $g_c = 0.05$. Note that we increase g_e compared to the previous case to test the robustness of the UKF against synchronized states. Since we use inhibitory synapses, the firing rate decreases slightly. In the limit of total synchronization the input through electric coupling, E_i goes to zero, while C_i is exactly the same for each element in the network.

We see in Figs. 5.6(a) and 5.6(b) that even with two coupling schemes, the chemical one being nonlinear, the UKF can estimate the correct coupling matrices. All networks are heterogeneous in the sense that the number of connections is not the same for the different neurons. As pointed out by Forero et al. [60], the UKF is robust against synchronization, which is confirmed here.

Here we presented reconstruction results in the case of inhibitory synapses, however, we checked that the UKF provide similar results also for excitatory synapses and a mix of excitatory and inhibitory synapses, provided it knows which synapses are excitatory and which are inhibitory.

We highlight that for all cases the Euclidean distance $D(G, G^{KF})$ saturates below 10^{-2}. Furthermore, to verify that all the links were correctly estimated we classified the performance of the UKF using the Receiver Operating Characteristic (ROC) curve[138]. If the UKF recovers the right connectivity, then the Area Under the ROC Curve (AUC)[138] will be 1. For all cases studied, we obtained an AUC > 0.99, implying a perfect reconstruction of the underlying topologies, that is, the UKF predicts a link between two neurons i and j only if $A_{ij} = 1$. We believe that the UKF is robust against noise as long as noise can be seen as a small perturbation to the system and the dynamics is not driven by it.

5.3.3 Estimation of network connectivity in temporal networks

Finally, we consider temporal networks, in which $G_{e,ij} = g_e\, A_{ij}$ varies with time. This is the case in many applications of network theory [139], and in neuroscience, it is especially important since it can be linked to plasticity [140].

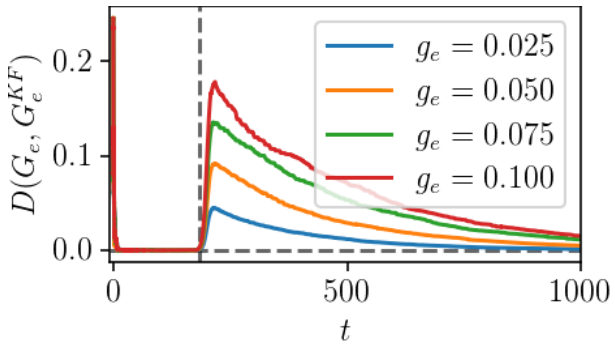

Figure 5.7: Evolution of the distance D between the adjacency matrix and the estimated one in the case of time-dependent coupling. D is depicted as a function of time, for different coupling strengths. The vertical dashed line represents the instant in which the coupling is turned on and the horizontal one marks the zero.

We model time-varying networks by considering couplings between neurons that switch on at a simulation time $t = 200$. More precisely, three single neurons connect at $t = 200$ in a linear chain, $(1 \leftrightarrow 2 \leftrightarrow 3)$,

$$g_e \begin{bmatrix} 0 & 0 & 0 \\ 0 & 0 & 0 \\ 0 & 0 & 0 \end{bmatrix} \rightarrow g_e \begin{bmatrix} 0 & 1 & 0 \\ 1 & 0 & 1 \\ 0 & 1 & 0 \end{bmatrix} . \tag{5.7}$$

We assume that all the internal parameters are known and we only estimate the network's topology.

The results are presented in Fig. 5.7. Before the coupling is switched on, the UKF has quickly inferred the absence of coupling (as $D \rightarrow 0$). After the coupling is switched on, D first increases sharply and then decreases steadily for all values of g_e. This means that the UKF can detect the emergence of coupling and estimate the G_e matrix correctly. However, the estimation after the change in the network takes more time than the initial estimation of the null adjacency matrix. This is because the covariance on the matrix coefficients will decrease, meaning high confidence in the inferred matrix before the coupling is switched. When the matrix is changed, the filter has to adjust to the new state, but the low covariance will make the convergence rate slow. Nevertheless, the filter is eventually able to recover the right network structure. Different initial model or state covariances are expected to impact the convergence time, both before and after turning on the coupling. Higher covariances will result in higher variability in the predictions. This variability is more efficient in capturing changes in the parameters. On the contrary, when covariances are smaller, the predictions are less prone to change and thus adapt to new values. The right choice of this parameter will result in a responsive system with sufficiently stable inferred parameters.

5.4 Remarks

We studied the capability of the UKF for recovering the parameters of a single neuron and of small neural ensembles modeled with the Izhikevich model. We simulated the equations

governing the system dynamics and used the simulated time series as experimental observations to feed the UKF algorithm, with confidence regulated by $\bar{Q}_\nu$. The IM was the process model with confidence regulated by $\bar{Q}_Z$.

When the parameters of an isolated neuron are constant in time, the UKF is able to estimate all the parameters. Second, we studied an isolated neuron with a sinusoidal input current, which displayed bursting spike dynamics. Due to the rich variety of dynamical behaviors of the IM, it is not trivial to identify the cause of the bursting activity. Still, even when modeling the current as a constant, the UKF retrieved the neuron parameters and the average value of the current and suggested an oscillating current. When including the oscillating current in the process model, the UKF was able to provide a reasonable estimate of the amplitude (α), the mean (I), and frequency of the oscillation (ω).

We have also estimated the connectivity of small networks of Izhikevich neurons with known internal parameters. First, we analyzed the five possible network topologies for four neurons with undirected electrical coupling. Then, we added directed chemical connections to the same networks. The UKF was able to recover the connectivity for all the networks regardless of the synchronization level.

Finally, we addressed the problem of temporal networks by analyzing a network of three electrically coupled neurons, in which the topology changed from no coupling to a chain topology. The UKF was able to identify the change in the network and estimate the connectivity correctly

The results presented here were obtained considering measurements of both x and y. Beyond that, we conducted a preliminary analysis of the applicability of the UKF when only measurements of the x variable are available. Our results suggest that the UKF is still able to recover the parameters of a single neuron and the network connectivity. However, to obtain good estimates, the UKF hyperparameters had to be carefully tuned, in particular, the standard deviation σ_ν and the initial condition for σ_P.

As in experimental measurements only short time series with limited temporal resolution can be recorded, further work is needed to clarify the impact of the duration of the time series and the sampling time. While the results presented here were obtained using each simulated data point (i.e, using the integration step as sampling time), preliminary studies suggest that the UKF is robust to downsampling up to 1:20, if the time series is long enough.

Motivated by the inherent limitations of such datasets, in the upcoming chapter we will address the specific issue of time resolution. We aim to develop a methodology that can effectively handle network inference when the only data available is the timing of events such as neuronal spikes.

6 Inferring the Connectivity from Event Timing Analysis

This chapter presents the results of the research conducted in collaboration with Hilda A. Cerdeira[1], Cristina Masoller[2], and Giulio Tirabassi[2]. The results here presented were summarized in a paper that is currently under review.

6.1 Introduction

In this chapter, we follow up with the problem of network inference. As we saw in the last chapter, the UKF is capable of inferring small networks of neurons if we keep track of the entire evolution of the system under study, and we know the model that best assimilates the data. Here, we will take into account the typical experimental limitation that only neuronal spikes can be detected. Furthermore, the model describing neuronal activity is unknown. Motivated by this, we aim to determine whether neural connectivity can be inferred when only the spike times are known.

This problem was addressed by Cestnik and Rosenblum [141], who considered pulse-coupled oscillators whose phases are instantaneously reset by incoming pulses. Using an iterative procedure to recover, from the inter-spike intervals (ISIs), the phase response curves (PRCs), the authors were able to recover all the properties of all the nodes, including the strengths of all connections. This approach has the advantage that the data requirements are not demanding (sequences of 200 spikes allowed to reconstruct a network of 20 Morris-Lecar neurons), but it assumes that the coupling between neurons is mediated only by the pulses, and that it is sufficiently weak to justify the description of the neural activity in terms of PRCs. Another network inference method based on the analysis of spike times was proposed by Casadiego and coworkers [48]. By approximating the ISIs of each neuron i by an unknown, locally smooth function of K_i cross-spike intervals, the inference problem was mapped to event spaces yielding linear equations that allowed least squares solutions

[1]Instituto de Física Teórica, Universidade Estadual Paulista, São Paulo, Brasil
[2]Departament de Fisica, Universitat Politecnica de Catalunya, Terrassa, España

for the topology.

Machine learning (ML) network inference methods have also been proposed. Panaggio and coworkers [59] considered networks of phase oscillators and showed that ML can reconstruct the interaction network, given sufficient data on the transient evolution of each oscillator.

However, data limitations degrade the performance of ML algorithms. Banerjee and coworkers [42] considered the performance of reservoir computing, on synthetic data simulated with coupled Lorenz chaotic systems and on experimental data of *C. elegans* neural activity, with known structural network. The authors assigned scores that reflected the link probability between pairs of nodes and studied how various limitations of data acquisition, such as observational noise, affected the scores.

Complementing these efforts, here we analyze the situation in which the only information available for reconstructing the network are event times (e.g., spikes times). To use the UKF method, we need to assume a model and a straightforward choice is the Kuramoto model of coupled phase oscillators [13]. While we could use the coupling coefficients inferred by UKF to define scores that reflect the link probability (as in [42]), here we reconstruct the network by applying a clustering algorithm to the inferred coupling coefficients, to discriminate them into two groups that correspond to existing and non-existing links (as in [142]). This allows us to quantify the reconstruction performance by calculating the F_1 score and the area under the receiver operating characteristic (ROC) curve.

To demonstrate this methodology, once again, we analyze neural activity simulated with the Izhikevich model [132]. In addition to that, we also analyze experimental data recorded from coupled Rössler-like chaotic electronic circuits with known structural network [143]. To reconstruct the circuits' network, we assume that the only information we have are event times –specifically, the times when the circuits' voltages change signs, from negative to positive values.

6.2 Models, Datasets and Methods

6.2.1 Izhikevich model

To generate the spikes data, once again, we simulate networks using the Izhikevich model—a neuron model capable of exhibiting many neuronal dynamics while being computationally efficient [132]. For completeness, we will write it again:

$$\begin{aligned} \dot{x}_i &= 0.04\,x_i^2 + 5x_i + 140 - y_i + I + E_i + \sigma_Z \xi_i^x, \\ \dot{y}_i &= a\,(b\,x_i - y_i) + \sigma_Z \xi_i^y, \end{aligned} \tag{6.1}$$

with the after-spike reset condition:

$$\text{if} \quad x_i > 30, \quad \text{then} \begin{cases} x_i \to c, \\ y_i \to y_i + d. \end{cases} \tag{6.2}$$

The parameters a, b, c, d, and I, specified in Table 6.1, we selected values such that the neurons display chaotic spiking dynamics [88]. E_i represents the electrical coupling

Table 6.1: Dimensionless parameters used to simulate the Izhikevich model [88, 132]

a	b	c	d	I	K	σ_Z
0.2	2	-56	-16	-99	$(0, 0.1)$	0.02

between neurons and is given by

$$E_i = K \sum_{j=1}^{N} A_{ij}(x_j - x_i), \tag{6.3}$$

where K is the coupling conductance and A_{ij} are the coefficients of the adjacency matrix: $A_{ij} = 1$ whenever neuron i is connected to neuron j, otherwise $A_{ij} = 0$. Since electric coupling is symmetric, the adjacency matrix is symmetric, $A_{ij} = A_{ji}$. Finally, ξ_i^x and ξ_i^y represent Gaussian noise terms, and σ_Z is the square root of the noise variance.

We solved the model equations using a fourth-order Runge-Kutta method with an integration step of $dt = 0.01$ and initial conditions drawn from a normal distribution centered at $x = -56.25$ and $y = -112.5$, with a standard deviation $\sigma = 3$. A transient of 80000 time steps was discarded, and the times of the spikes that occurred in the following 40000 time steps were saved for analysis. The spike times were defined as the times in which the variable x reaches the reset condition, $x_i > 30$, and were linearly interpolated to be the $t_i : x(t_i) = 30$.

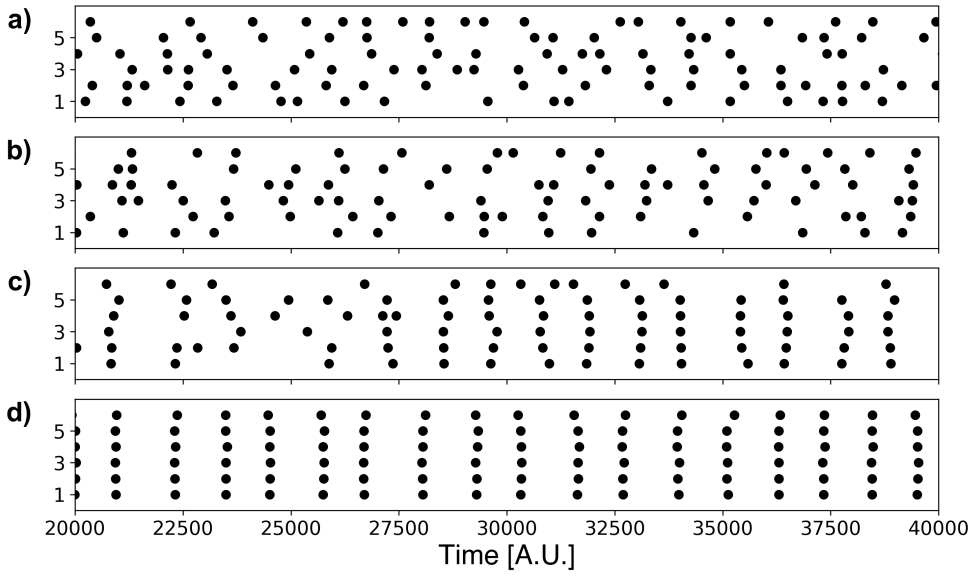

Figure 6.1: Spiking activity of a random network of 6 Izhikevich neurons and 8 links when the neurons are (a) uncoupled ($K = 0$), (b) weakly coupled ($K = 0.01$), (c), (d) strongly coupled (K =0.04 and 0.1 respectively).

Figure 6.1 displays an example of the spikes of a random network with 6 neurons and 8 links, for different coupling strengths. As can be observed, as the coupling increases, the spikes tend to become synchronized.

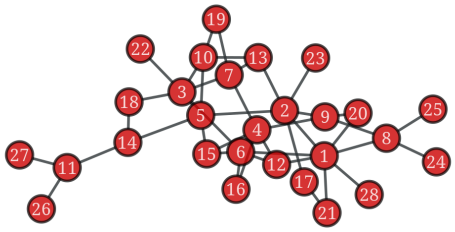

Figure 6.2: Network $R7$ of electronic circuits [143] that has $N = 28$ circuits (nodes) and 42 undirected links.

6.2.2 Chaotic electronic circuits

We also analyze a freely available experimental data set [143] that contains measurements from a network of $N = 28$ chaotic (Rössler-like) mutually coupled electronic circuits; the circuits are coupled with 42 links whose strength (the same for all the links) varies from 0 to 100. For each coupling strength, the voltage in each circuit was recorded three times. Each time, 30000 data points were recorded. We selected the data set recorded for the network $R7$, which is shown in Fig. 6.2. For our analysis, we used the following set of coupling strengths: {0, 6, 11, 16, 21, 26, 31, 36, 41, 46, 51}; for stronger coupling the circuits become phase synchronized and their phase dynamics does not change significantly from $K = 51$.

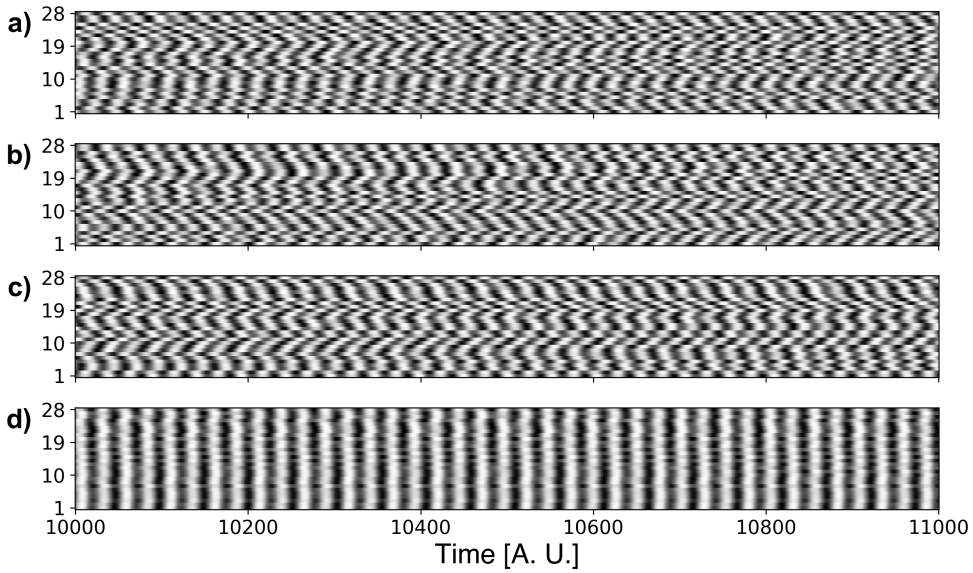

Figure 6.3: Oscillatory activity of 28 electronic circuits (in color code, experimentally recorded x variable) when the circuits are (a) uncoupled ($K = 0$), (b) weakly coupled ($K = 1$) and (c, d) strongly coupled ($K = 10$ and $K = 50$ respectively).

We show in Fig. 6.3 the time evolution of the 28 oscillators for different coupling strengths. As for the Izhikevich neurons, we consider different levels of synchronization, up to a phase synchronized state.

We define events by considering the crossings of the $x = 0$ axis from $x < 0$. As in the neurons' case, the crossing times are linearly interpolated.

6.2.3 Phase description

From now on, we consider that the event times are the only data available to reconstruct the network, that is, for the neurons, we only know the spike times, and for the electronic circuits, we only know the times of $x = 0$ crossings. Interpreting each neuron/circuit as a phase oscillator, we associate a phase time series to each neuron/circuit by assuming that the phase increases linearly by 2π between consecutive spikes/crossings [7, 144].

An example of the procedure is shown in Fig. 6.4. Regarding time resolution of the phases, we decided to use the model integration step for the neurons while, for the electronic circuits, we downsampled the original timeseries to 1/5 of the measurement frequency, as we have seen that this has little impact on the accuracy but, at the same time, it speeds up the calculation significantly. Since the Kalman filter is designed to assimilate noisy observations, we added to the piece-wise linear phases a small stochastic term (Gaussian white noise with variance $\sigma_\phi = 0.12$).

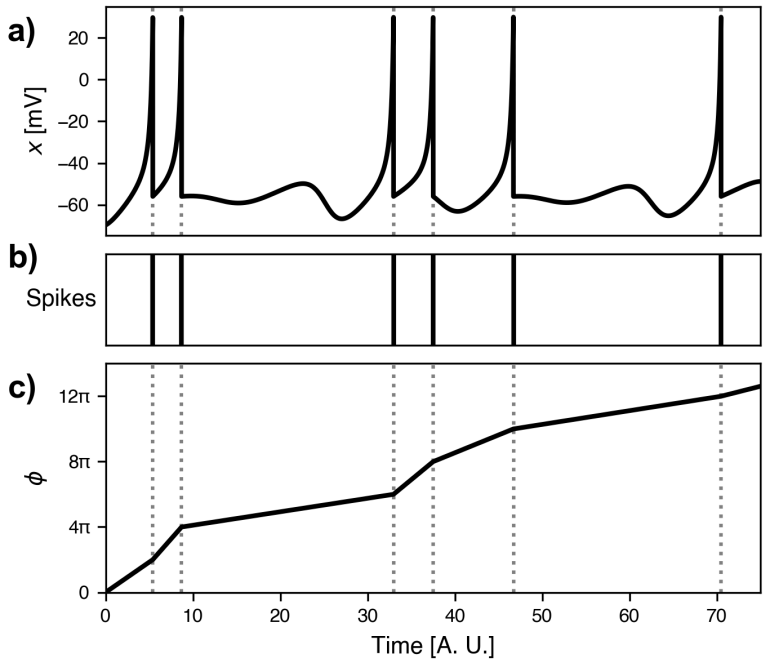

Figure 6.4: Example of a phase time series, $\phi(t)$, obtained from a voltage time series, $x(t)$. (a) $x(t)$. (b) Spikes occur when x reaches the reset condition ($x > 30$mV). (c) For each spike time, t_n, we define the phase as $\phi(t_n) = 2n\pi$ and interpolate linearly between consecutive spikes times.

6.2.4 UKF assimilation to the Kuramoto model

We assume that the phases' dynamics can be described, at least partially, in terms of a phase reduction equation of the form

$$\dot{\phi}_i = \bar{\omega} + \sum_{j=1}^{N} m_{ij} F(\phi_j, \phi_i) + \sigma_i \xi_i, \tag{6.4}$$

with F being a periodic function of ϕ_i and ϕ_j. A simple option for F is $F(\phi_j, \phi_i) = \sin(\phi_j - \phi_i)$, which gives the well-known Kuramoto model [13]:

$$\dot{\phi}_i = \bar{\omega} + \sum_{j=1}^{N} m_{ij} \sin(\phi_j - \phi_i) + \sigma_i \xi_i, \tag{6.5}$$

where $\bar{\omega}$ is the natural frequency of the oscillators, which is assumed to be the same for all oscillators, $m_{ij} = m_{ji}$ are symmetric coupling coefficients, ξ_i is a Gaussian noise term, and σ_i is the noise standard deviation, representing, in the context of UKF, the uncertainty in the model used to fit the data.

The Kuramoto model successfully describes coupled phase oscillators; however, we remark that our approach is flexible because another, more advanced model could be used. For instance, in Eq.(6.5), non-instantaneous, lagged interactions could have been considered; however, this has the drawback that additional parameters need to be estimated.

UKF is able to estimate the state of N phase oscillators, denoted by $\bar{u} = [\phi_1; ...; \phi_N]^T$, by assimilating N phase time series (defined from the spikes or event times) into the Kuramoto model. Since our goal is to retrieve the oscillators' connectivity, we extend the state of the system to include the $N(N-1)/2$ coupling parameters, m_{ij}. Therefore, the state vector, $\bar{u} = [\phi_1; ...; \phi_N; m_{1,2}; ...; m_{N-1,N}]^T$, is a vector of dimension $M = N + N(N-1)/2$. Since the network structure remains constant in time, the equations governing the evolution of the coupling coefficients are $dm_{ij}/dt = 0$.

The natural frequency of the oscillators, $\bar{\omega}$, can be estimated as the average frequency of the oscillators when they are uncoupled. However, this information might not always be available; therefore, to demonstrate the general applicability of our methodology, we estimate $\bar{\omega}$ for every coupling strength, K, directly from the phases' time series as the average frequency of the oscillators. A comparison of different ways to estimate $\bar{\omega}$ is presented in Appendix D.1

We implemented the UKF algorithm using the *Python* package *FilterPy*, with parameters given in Table 6.2. To initialize the algorithm, we have to choose initial conditions for the state vector $\bar{u}$. For the phases, we used the values at $t = 0$ while for the coupling coefficients, we set them all to an initial value K_0. The covariance matrices associated with the process and measurement processes, which are also evolved by the UKF algorithm, were initialized with the standard deviations σ_Z and σ_ν. The covariance estimate matrix was initialized as $\mathbf{I}\sigma_P$, where $\mathbf{I}$ is an $M \times M$ identity matrix.

The UKF provides an estimation for ϕ_i, σ_i, and m_{ij} at each time. An example of the evolution of the inferred coupling coefficients is presented in Fig. 6.5. Since the inference at

Table 6.2: Parameters used in the UKF algorithm [112, 137] for the assimilating the phase time series of the neurons (of the chaotic circuits) to the Kuramoto model.

K_0	σ_Z	σ_ν	σ_P	α
$0.1(0.05)$	$0.01(0.1)$	$0.05(0.15)$	$0.05(0.01)$	0.0001

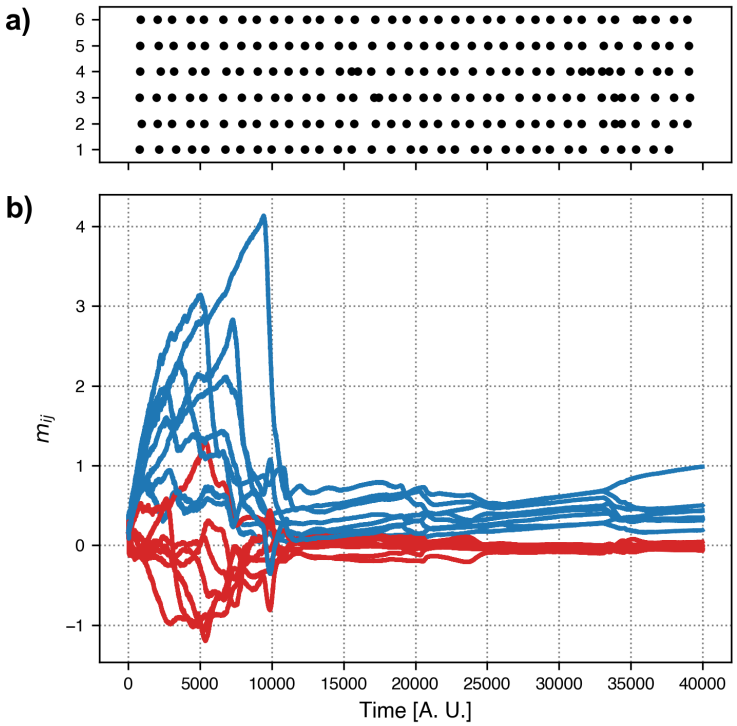

Figure 6.5: (a) Spike times of a random network of $N = 6$ Izhikevich neurons with 8 links and coupling $K = 0.04$. (b) Inferred coupling coefficients using the UKF. The blue lines represent the coefficients of existing links and the red lines, those of non-existing links.

the last available time integrates the information of all the other time steps, we consider the last estimation of the m_{ij} coefficients as the UKF estimation of the coefficients.

We remark that the UKF approach is multivariate, in the sense that the algorithm uses N $\phi_i(t)$ time series to infer at once the m_{ij} coefficients.

6.2.5 Network inference

To transform the set of m_{ij} values returned by UKF into an inferred binary adjacency matrix, we used a k-means clustering algorithm [145, 146] that classifies the coefficients in three clusters. Other choices are possible, but we found that three clusters is the minimum number that gives good performance. The clustering algorithm puts low coupling values in the first cluster, high values in the second, and outliers in the third. The first cluster is interpreted as

composed by non-existing links (zeros in the adjacency matrix), while the other two clusters are interpreted as composed by existing links (ones in the adjacency matrix). Alternative approaches can be used to binarize the coefficients m_{ij}, which include, for instance, using a threshold defined in terms of the mean value and the standard deviation of the m_{ij} values.

6.2.6 Performance quantification

To evaluate the performance of the network reconstruction, for the neuron network we will use the F_1 score [147],

$$F_1 = \frac{2TP}{2TP + FN + FP}, \tag{6.6}$$

where TP is the number of true positives, FP the number of false positives, and FN the number of false negatives. The F_1 score represents the harmonic average between two other scores: *precision*, which is the fraction of predicted links that are real links, and *recall*, which is the fraction of real links recovered by the algorithm. Therefore, a perfect reconstruction will have $F_1 = 1$. Moreover, being a harmonic average, a low value of one score (precision or recall) will give a low F_1, regardless of the value of the other score.

In the case of the 28 electronic circuits, we will evaluate the performance in terms of the Area Under the Curve (AUC). We use the AUC instead of F_1 because the clustering algorithm does not provide a good differentiation of the coefficients into existing and non-existing links. An AUC$= 1$ means that there is a threshold that can perfectly classify the inferred coefficients into high coefficients, representing links, and low coefficients representing non-existing links. An AUC$= 0.5$, instead, represents the expected performance of a random classifier.

We compare the UKF performance with the performance of two bivariate link inference methods: the Pearson cross-correlation coefficient (CC) and the Mutual Information (MI) [148]. We calculate CC and MI from the phase times series, because we assume that we only know the event times, from which we derive phase time series. CC_{ij} is calculated as:

$$CC_{ij} = \frac{1}{T}\left|\sum_{t=0}^{T} a_i(t)a_j(t)\right| \tag{6.7}$$

where $a_i(t)$ and $a_j(t)$ are the detrended and normalized (to zero mean and unit variance) phase time series of oscillators i as j, and T is the length of the time series. MI_{ij} is calculated as

$$MI_{ij} = \iint p_{ij}(a_i, a_j) \log \frac{p_{ij}(a_i, a_j)}{p_i(a_i)p_j(a_j)}\, \mathrm{d}a_i \mathrm{d}a_j, \tag{6.8}$$

where the probability distributions p_i and p_j are derived from $a_i(t)$ and $a_j(t)$, and p_{ij} is the joint distribution.

For simplicity, in Eqs. (6.7) and (6.8) we neglect a possible lag between a_i and a_j; taking into account a lag may improve the reconstruction for weak coupling, while no significant effect is expected at strong coupling because the oscillators synchronize with zero lag.

The clustering procedure described in Sec. 6.2.5 for inferring the network from the m_{ij} coefficients returned by UKF, will also be applied to the $\{CC_{ij}\}$ and $\{MI_{ij}\}$ values.

6.3 Results

6.3.1 Izhikevich neurons

The results obtained by applying the network inference algorithms based on UKF, MI, and CC are displayed in Fig. 6.6 as a function of the coupling strength K. Here, for each K, we simulated 15 random networks with 6 neurons and 8 links.

An F_1 value was calculated for each reconstructed network, and we used the 15 F_1 values to compute the F_1 statistics.

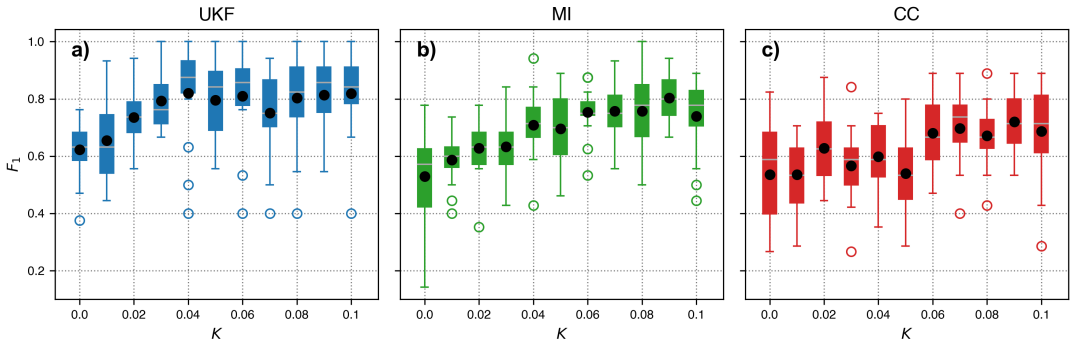

Figure 6.6: Performance of the inference methods based on UKF, MI, and CC as a function of the coupling strength, K, for a network of Izhikevich neurons. Box-plot statistics are obtained by inferring 15 different network topologies of 6 nodes and 8 links. Black circles represent the average score for each coupling coefficient.

We can observe that, for weak and intermediate coupling strengths, UKF tends to outperform the bivariate inference based on MI or CC, whereas the three methods perform similarly for strong coupling.

We also note a large dispersion of F_1 values for the three inference methods, regardless of the coupling strength. Perfect reconstruction of the adjacency matrix is, in general, not possible, as the F_1 is usually less than 1, except for a few perfect reconstructions obtained with the UKF algorithm.

To try to improve the performance of the inference methods, we simulated the model a number of times s, with different initial conditions but the same adjacency matrix. Alternatively, we could simulate long enough time series and divide them into s non-overlapping segments.

From each set k ($k = 1 \dots s$) of spike sequences we derived the phase time series and applied to them the UKF algorithm, which returned the m_{ij}^k coefficients of the kth set, and we also calculated the corresponding CC_{ij}^k and MI_{ij}^k values. Then, the network was reconstructed by applying the same clustering procedure as before, but to $\langle m_{ij} \rangle_s$, $\langle CC_{ij} \rangle_s$ and $\langle MI_{ij} \rangle_s$, where $\langle \dots \rangle_s = (\sum_{k=1}^{s} \dots)/s$ represents the average over s simulations. Then, an F_1 value was calculated for each reconstructed network. Repeating the procedure with 15 different

coupling topologies, we obtained 15 F_1 values that were used to compute the F_1 statistics.

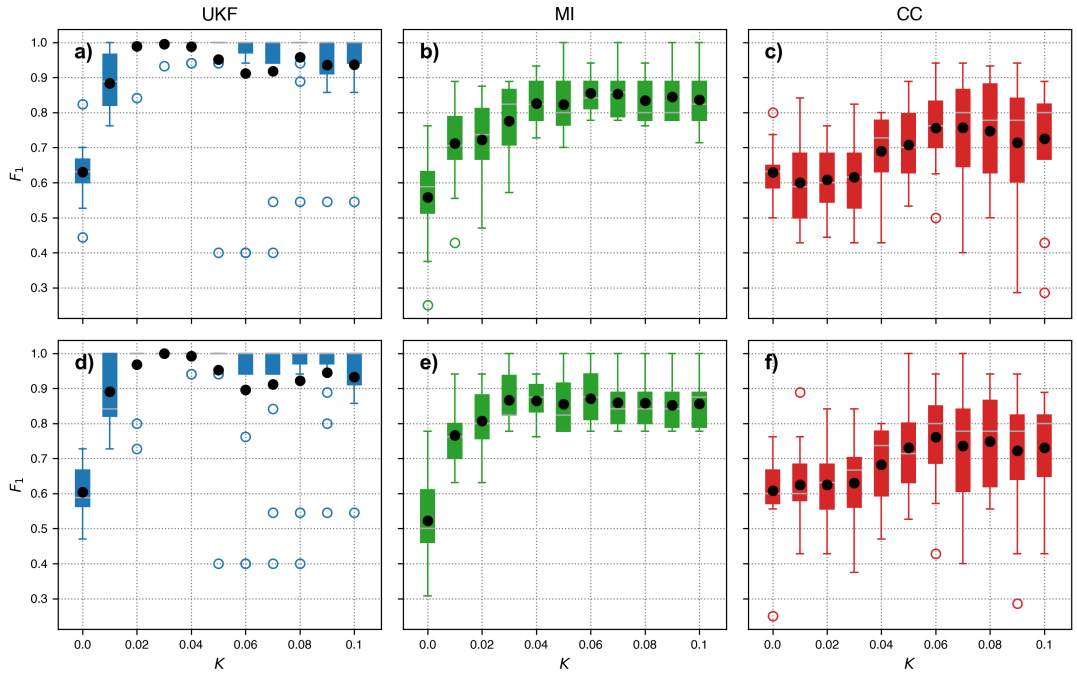

Figure 6.7: As Fig. 6.6 but the network is inferred from $\langle m_{ij} \rangle_s$, $\langle MI_{ij} \rangle_s$ and $\langle CC_{ij} \rangle_s$ averaged over $s = 36$ simulations (a, b, c) or $s = 99$ simulations (d, e, f).

The results are presented in Fig. 6.7, where the top (bottom) row presents the F_1 statistics for $s = 36$ ($s = 99$). We can see that averaging the inferred coefficients improves the UKF performance, whereas the performance of MI is only slightly improved, and the CC performance is left almost unaffected. However, despite the overall good performance, UKF presents some negative outliers, even after averaging $s = 99$ inferred coefficients, while MI and CC seem to be more robust. Examples of good and bad UKF reconstructions are presented in Fig. 6.8, where panel a) presents the real network, b) presents a good reconstruction ($F_1 = 0.933$), and c) presents a poor reconstruction ($F_1 = 0.4$).

We have analyzed the reasons for the negative UKF outliers and found that the m_{ij} coefficients are correctly ordered (the highest coefficients corresponding to existing links and the lowest coefficients, to missing links), but the clustering algorithm does not find the right threshold to separate them.

Low UKF performance occurs with three specific network topologies, and for these topologies, UKF inference does not benefit from the averaging procedure. While more work is needed in order to understand why UKF has low performance, we stress that for these topologies the performance is low for high enough coupling; for weaker coupling their reconstruction can even be perfect, as seen in Fig. 6.7 (d), where for $K = 0.03$ the 15 networks are perfectly reconstructed (for $K = 0.03$ and $s = 99$, UKF $F_1 = 1$).

It is important to note that, even though a general performance improvement is expected

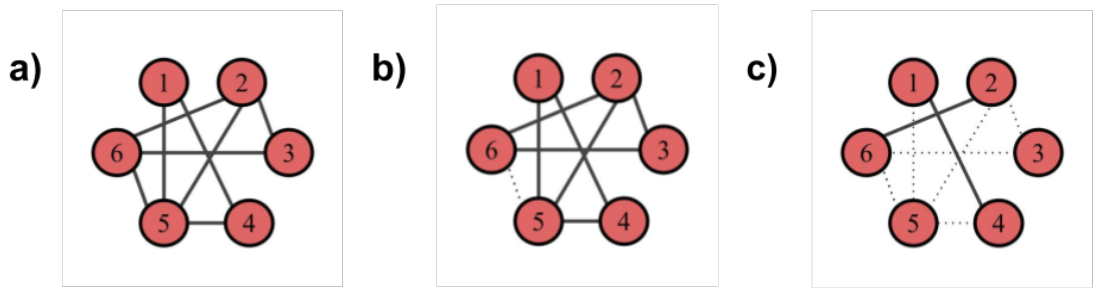

Figure 6.8: Examples of good (b) and poor (c) UKF reconstruction of the network shown in panel (a). In (b) and (c) the dashed lines indicate links that were not inferred (false negatives). The coupling strength is $K = 0.08$.

from the averaging procedure, as using more simulations provides more data to infer the links, the efficiency with which the three methods leverage the new information is clearly different. We speculate that the statistical similarity of the neurons' time series across various time series (or segments) is high, leading to high correlations between the MI-based and CC-based inferences obtained from different simulations, leading to a small improvement or even no improvement of their performance. On the other hand, providing a model such as the Kuramoto model to the UKF allows us to extract more information from small datasets, e. g. discriminating small coupling from no coupling. These arguments are of course heuristics and more work is needed to understand the effect of the averaging procedure.

We compared the UKF performance when different ways of estimating the natural frequency of the oscillators, $\bar{\omega}$, were used (see Appendix D.1). We found that when the dynamics of the oscillators is highly regular (the spike/crossing times are almost periodic), setting $\bar{\omega} = 0$ gives the best performance. In addition, we analyzed the effect of the network size and link density, the results are presented in Appendix D.2. As could be expected, for all methods, increasing the network size decreases the performance. On the other hand, increasing the link density facilitates the inference. Overall, UKF is the most precise method (see Figs. D.3 and D.4 in Appendix D.2). The effect of the time series length is discussed in Appendix D.3, where we show that, as expected, the performance of the three methods decreases for shorter time series, but still UKF yields the best performance. Finally, the computational cost of the algorithms as a function of the network size is analyzed in Appendix D.4. Inevitably, the UKF has the largest computational costs, and it increases rapidly with the size of the network. This comes as no surprise since the UKF is a multivariate estimator, while MI and CC are bivariate measures.

Taken together, the results of the analysis of synthetic spike sequences generated with the Izhikevich model indicate that UKF is the optimal choice to reconstruct small networks of weakly coupled neurons.

6.3.2 Chaotic electronic circuits

In this section, we present the results obtained for the reconstruction of the network of 28 chaotic, Rössler-like electronic circuits. As the time series have 30000 data points (much longer than the length needed for UKF to produce a stable inference), we divided the time series into six non-overlapping segments so that each one contains approximately 40 $x = 0$ crossing events, as in the neurons' case. Since, for each coupling strength, three time series are available, we have 18 segments to analyze, and therefore, we have 18 AUC values to compute the score statistics. As explained in Sec. 6.2.6, we quantify performance in terms of the AUC rather than F_1 because the clustering algorithm does not provide good differentiation of the coefficients between existing and non-existing links and this occurs not only for the m_{ij} set, but also, for the MI_{ij} and CC_{ij} sets.

As in the neurons' case, we can also use the 18 segments to obtain 18 estimations of the values of m_{ij}, MI_{ij} and CC_{ij}, and we can average them to obtain the final estimations, i.e. to obtain the matrices $\langle m_{ij} \rangle_s$, $\langle MI_{ij} \rangle_s$ and $\langle CC_{ij} \rangle_s$ that are binarized to reconstruct the network.

Figure 6.9 displays the performance of UKF, MI, and CC in the reconstruction of the network. For UKF reconstruction, we have found that when the oscillators' dynamics is highly regular, i.e., when the timing of $x = 0$ crossings is nearly periodic, the best UKF performance is obtained by setting $\bar{\omega} = 0$. This occurs when $K \geq 13$. The reason for this to happen and more in general the influence of the estimation of $\bar{\omega}$ is discussed in Appendix D.1.

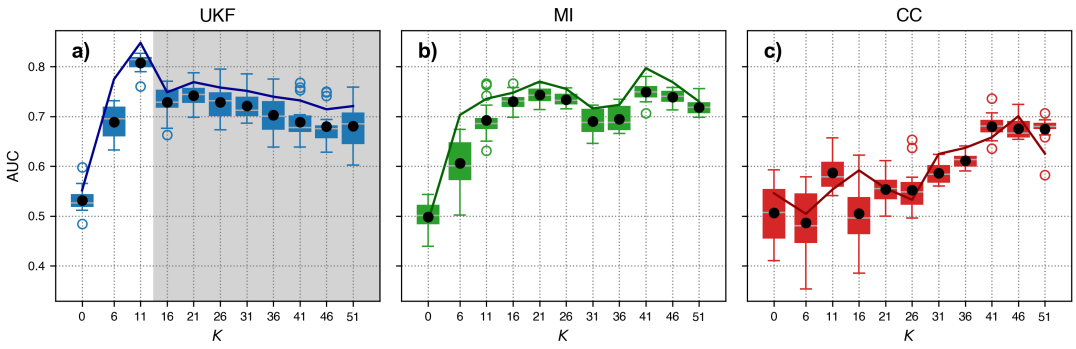

Figure 6.9: Performance of UKF, MI, and CC inference methods for the network of 28 chaotic electronic circuits. Box-plot statistics are obtained from 18 data segments and the black circles indicate the average score. The solid lines represent the AUC when the network is inferred from $\langle m_{ij} \rangle_s$, $\langle MI_{ij} \rangle_s$ and $\langle CC_{ij} \rangle_s$, where the average is over $s = 18$ non-overlapping segments. The shaded area in panel a) represents the region where the oscillators have nearly identical frequencies and the best UKF performance is obtained by selecting $\bar{\omega} = 0$.

We can see in Fig. 6.9 that the averaging procedure improves the performance of both UKF and MI, while it does not affect the CC performance, which remains poor.

We also note that MI's performance is comparable to UKF's, but UKF performs slightly better for low coupling. Specifically, UKF's best performance is at $K = 11$, and for this

coupling strength, the best binarization threshold gives, for UKF, $F_1 = 0.416$, while for MI, $F_1 = 0.281$. On the other hand, MI's best performance is at $K = 41$, and for this K, the best binarization threshold gives, for UKF, $F_1 = 0.344$, while for MI, $F_1 = 0.407$.

We believe that at high enough coupling MI outperforms UKF either because the approximation of the function $F(\phi_j, \phi_i)$ in Eq. 6.4 by $F(\phi_j, \phi_i) = \sin(\phi_j - \phi_i)$ is not appropriated (as discussed in Appendix A) or because the phase description is not sufficiently precise and amplitude effects need to be taken into account.

The good performance of the UKF in terms of AUC means that the inferred coefficients have the right relative magnitude: on average, those corresponding to existing links are larger than those corresponding to non-existing links. However, further studies are needed to determine the optimal strategy to choose an appropriate threshold to classify the $\langle m_{ij} \rangle_s$ values in two distinct populations that correlate as much as possible with the adjacency matrix.

6.4 Remarks

We have analyzed the performance of the Unscented Kalman filter (UKF) for inferring the topology of coupled oscillators directly from the timing of events that occur in their dynamics, and compared with the performance of the mutual information (MI), and of the cross-correlation (CC). Specifically, we have considered neural spike times simulated with the Izhikevich model and experimental data recorded from chaotic electronic circuits, consisting of the times when the circuits' voltages change sign, from negative to positive values. In both cases, we have used the event times (spikes or threshold crossings) to obtain phase time series, and used UKF to assimilate the phases' time series to the Kuramoto model. On synthetic data from small neural networks, we have found that averaging the UKF prediction over multiple realizations can allow obtaining a perfect reconstruction of the coupling topology. This averaging procedure also benefits the inference when using MI and CC, but their performance is in general lower than that of UKF.

In the experimental data, no method could fully recover the network. We have found a comparable performance of UKF and MI, with CC's performance being significantly lower. Both, UKF and MI benefit from the averaging procedure before inferring the network, with UKF performing better at weak coupling and MI performing better at higher coupling.

The downside is that the improved performance of UFK comes with a high computational cost, which makes it unfeasible to use in the case of large networks.

We believe that the UKF method proposed here can be very useful for inferring the topology of small networks of coupled oscillators, when the oscillators can be approximately described as phase oscillators, because in this case UKF may provide better performance than MI or CC.

Part IV

Conclusion

7

Conclusion and final remarks

In this thesis, we investigated two topics, first the stability of synchronized states and second network inference. The connection between these two topics comes from the large amount of systems in nature that can be described as complex networks. In these systems, synchronization often occurs, and since the underlying network structure is unknown, understanding the phenomena becomes a rather trivial task. On the analytical side, we applied the master stability function formalism to study the stability of synchronized solutions in networks of Izhikevich neurons.

The first motivation to study the Izhikevich (IM) model comes from the ability of this model to display many neuronal patterns while being computationally efficient. In addition to it, the original paper by Izhikevich, where the model was introduced, accumulates more than five thousand citations. Similarly, the paper that introduced the Master Stability Function, by Pecora and Carroll, has received almost three thousand. Nevertheless, even twenty years after the publication of these works, our study marks the first application of the MSF to the IM. This stems from the challenges associated with calculating Lyapunov exponents in systems with discontinuities, like the IM. To overcome this, we applied the formalism of Saltation matrices to evaluate the Lyapunov exponents associated with the synchronized solutions.

With this framework (MSF + SM), we first analyzed the stability of total synchronized states, considering electrical and chemical couplings between neurons. To quantify the synchronization, we used the synchronization error (Err), i.e., the mean difference between the trajectories of the x variables of each neuron. By varying the coupling strength, we found that the synchronization error aligns well with MSF analysis when only one type of coupling is taken into account. While the network of electrically coupled neurons reached synchronization, the chemically one did not. However, introducing electrical coupling to a network solely connected chemically leads to synchronization. In this last case, we found that near the threshold for synchronization predicted by the MSF, a complex basin of attraction, also known as riddled. This leads to a coexistence of synchronized and non-synchronized solutions in this region, and as the coupling strength increased, this basin vanished, and all the solutions ended up synchronized.

Continuing with MSF analysis, we studied cluster synchronized states, where similar results were obtained. Nevertheless, when we considered the action of both types of coupling, on average, high-quality synchronization (Err ≈ 0) was not achieved in the range of coupling strength studied. We expected that synchronized solutions would be observed for coupling strengths $g \geq g_{th}$, instead, they only appear for higher coupling strengths. Similarly to the case of total synchronization, we found a riddled basin of attraction, characterized by a small uncertainty exponent.

These results underscore that the MSF is not a definitive diagnosis about the stability of synchronized solutions. Being dependent on a linear approximation, it is susceptible to such discrepancy. In resume, obtaining a negative MLE for the synchronized state is essential but does not assure its existence. On top of that its application to real-world systems is difficult since it is based on the assumption of identical oscillators, the absence of noise, and that usually we do not know the network of the system under study.

In the second part of this thesis, we tackled the last of the problems mentioned: network inference. To do so, we applied the Unscented Kalman filter (UKF) to the IM. As a warm-up to the network inference, we tested whether the UKF was capable of inferring the parameter of an isolated Izhikevich neuron. For the case where the x variable was measured at the same rate as the sampling time, the UKF proved to be very accurate for this task for all parameters, even in the case of a varying input current. Next, we considered networks of Izhikevich neurons with only electrical coupling and electrical + chemical couplings. In both situations, we quantified the precision of the UKF by measuring the distance between the real matrix and the estimated one. In both cases, the UKF was capable of inferring the networks.

Building upon these results, we decided to analyze UKF in inferring the connectivity structure of coupled oscillators based on event timing. To employ the UKF in this case, we associated a phase with timing events and then attempted to assimilate it into the Kuramoto model. Utilizing simulated neural spike times and experimental data from chaotic electronic circuits, we compared the efficacy of UKF with that of mutual information (MI) and cross-correlation (CC). Results on synthetic data reveal that averaging UKF predictions over multiple instances achieves perfect coupling topology reconstruction, outperforming MI and CC. However, this enhanced performance of UKF is accompanied by a considerable computational cost, rendering it impractical for large networks. In real-world experimental data, neither method fully recovered the network, with UKF and MI exhibiting comparable performance, while CC lagged significantly. Both UKF and MI benefit from averaging, with UKF excelling at weak coupling and MI at higher coupling.

Future work will be devoted to searching for a theoretical foundation to better understand the UKF performance in the case of strong coupling, for which not only the phase but also the amplitude dynamics may have to be considered. In addition, we plan to test the UKF's ability to infer directed pulsed interactions such as chemical couplings. It would also be interesting to analyze whether a more detailed, tailored phase model—instead of the generic Kuramoto model—or if a more advanced phase-extraction procedure (for example, using the Hilbert phase) could improve performance. It will also be interesting to consider whether other methods to analyze the set of inferred coupling coefficients (rather than k-means clustering) could lead to improved performance.

Part V

Supplementary Materials

A

Supplementary Material to Chapter 3

A.1 Derivation of MSF for the chemical coupling

Starting from Eq. 3.12 we define the 2×2 matrices

$$\mathbf{H} = \begin{bmatrix} h & 0 \\ 0 & 0 \end{bmatrix} \quad \text{and} \quad \mathbf{C} = \begin{bmatrix} \zeta & 0 \\ 0 & 0 \end{bmatrix} , \tag{A.1}$$

where h and ζ are nonlinear operators

$$hx = h(x) = x - v_s , \tag{A.2}$$

$$\zeta x = \zeta(x) = [1 + \exp(-\epsilon(x - \theta))]^{-1} , \tag{A.3}$$

and an operator $\mathbf{Dg}$, that returns a diagonal matrix whose elements are the components of the vector on which it acts. For example, for $\mathbf{x}$:

$$\mathbf{Dg}(\mathbf{x}) = \mathbf{Dg} \begin{bmatrix} x^1 \\ y^1 \\ \vdots \\ x^N \\ y^N \end{bmatrix} = \begin{bmatrix} x^1 & 0 & \dots & 0 & 0 \\ 0 & y^1 & \dots & 0 & 0 \\ \vdots & \vdots & \ddots & \vdots & \vdots \\ 0 & 0 & \dots & x^N & 0 \\ 0 & 0 & \dots & 0 & y^N \end{bmatrix} , \tag{A.4}$$

where in this notation $\mathbf{Dg}(\mathbf{x})$ reads $\mathbf{Dg}$ acts on $\mathbf{x}$. We can write the vector encoding the synaptic coupling of a network of N nodes as

$$\mathbf{Dg}[(\mathbf{I}_N \otimes \mathbf{H})(\mathbf{x})](A \otimes \mathbf{C})(\mathbf{x}) . \tag{A.5}$$

Moreover, it is convenient to introduce the matrices

$$\mathbf{T} = \mathbf{Dg}(\mathbf{I}_N \otimes \mathbf{H}) \tag{A.6}$$

$$\mathbf{K} = \mathbf{Dg}(\mathbf{I}_N \otimes \mathbf{C}) . \tag{A.7}$$

With this notation, the dynamics of a network coupled through chemical synapses reads

$$\dot{\mathbf{x}} = \mathbf{F}(\mathbf{x}) - g_c \mathbf{T}\mathbf{x}[(A \otimes \mathbf{C})(\mathbf{x})] \,. \tag{A.8}$$

For example, if $N = 1$,

$$\begin{aligned} \mathbf{T}\mathbf{x} = \mathbf{D}\mathbf{g}\left[\left(\mathbf{I}_1 \otimes \begin{bmatrix} h & 0 \\ 0 & 0 \end{bmatrix}\right)\begin{bmatrix} x^1 \\ y^1 \end{bmatrix}\right] &= \mathbf{D}\mathbf{g}\begin{bmatrix} h(x^1) \\ 0 \end{bmatrix} \\ &= \begin{bmatrix} x^1 - v_s & 0 \\ 0 & 0 \end{bmatrix} \end{aligned} \tag{A.9}$$

If we consider a network with $N = 2$ neurons and adjacency matrix given by

$$A = \begin{bmatrix} 0 & 1 \\ 1 & 0 \end{bmatrix} \,, \tag{A.10}$$

the coupling term reads

$$\begin{aligned} \mathbf{T}\mathbf{x} = \mathbf{D}\mathbf{g}\left(\begin{bmatrix} 1 & 0 \\ 0 & 1 \end{bmatrix} \otimes \begin{bmatrix} h & 0 \\ 0 & 0 \end{bmatrix}\right)\begin{bmatrix} x^1 \\ y^1 \\ x^2 \\ y^2 \end{bmatrix} &= \mathbf{D}\mathbf{g}\begin{bmatrix} h & 0 & 0 & 0 \\ 0 & 0 & 0 & 0 \\ 0 & 0 & h & 0 \\ 0 & 0 & 0 & 0 \end{bmatrix}\begin{bmatrix} x^1 \\ y^1 \\ x^2 \\ y^2 \end{bmatrix} \\ \mathbf{T}\mathbf{x} = \mathbf{D}\mathbf{g}\begin{bmatrix} h(x^1) \\ 0 \\ h(x^2) \\ 0 \end{bmatrix} &= \begin{bmatrix} h(x^1) & 0 & 0 & 0 \\ 0 & 0 & 0 & 0 \\ 0 & 0 & h(x^2) & 0 \\ 0 & 0 & 0 & 0 \end{bmatrix} \end{aligned} \tag{A.11}$$

times

$$(A \otimes \mathbf{C})(\mathbf{x}) = \begin{bmatrix} 0 & 0 & \zeta & 0 \\ 0 & 0 & 0 & 0 \\ \zeta & 0 & 0 & 0 \\ 0 & 0 & 0 & 0 \end{bmatrix}\begin{bmatrix} x^1 \\ y^1 \\ x^2 \\ y^2 \end{bmatrix} = \begin{bmatrix} \zeta(x^2) \\ 0 \\ \zeta(x^1) \\ 0 \end{bmatrix} \tag{A.12}$$

yielding

$$\mathbf{T}(\mathbf{x})[(A \otimes \mathbf{C})(\mathbf{x})] = \begin{bmatrix} h(x^1) & 0 & 0 & 0 \\ 0 & 0 & 0 & 0 \\ 0 & 0 & h(x^2) & 0 \\ 0 & 0 & 0 & 0 \end{bmatrix}\begin{bmatrix} \zeta(x^2) \\ 0 \\ \zeta(x^1) \\ 0 \end{bmatrix} \tag{A.13}$$

$$\mathbf{T}(\mathbf{x})[(A \otimes \mathbf{C})(\mathbf{x})] = \begin{bmatrix} h(x^1)\zeta(x^2) \\ 0 \\ h(x^2)\zeta(x^1) \\ 0 \end{bmatrix} \,. \tag{A.14}$$

Following the Pecora-Carroll analysis, the master stability function can be obtained via the variational equation for $\delta\mathbf{x}^i = \mathbf{x}^i - \mathbf{x}^s$. So first, we derive the synchronized solution $\mathbf{x}^s$, where $\mathbf{x}^i = \mathbf{x}^j, \forall\, i, j$. If we take an adjacency matrix equal to Eq. 3.16, we have

$$\dot{\mathbf{x}}^s = \mathbf{F}(\mathbf{x}^s) - g_c \mathbf{T}(\mathbf{x}^s)[(A \otimes \mathbf{C})(\mathbf{x}^s)] \,, \tag{A.15}$$

the second term reads

$$\mathbf{Dg}\left\{\left(\begin{bmatrix}1&0&0&0\\0&1&0&0\\0&0&1&0\\0&0&0&1\end{bmatrix}\otimes\begin{bmatrix}h&0\\0&0\end{bmatrix}\right)\begin{bmatrix}x^s\\y^s\\\vdots\\x^s\\y^s\end{bmatrix}\right\}\left\{\left(\begin{bmatrix}0&1&0&1\\1&0&1&0\\0&1&0&1\\1&0&1&0\end{bmatrix}\otimes\begin{bmatrix}\zeta&0\\0&0\end{bmatrix}\right)\begin{bmatrix}x^s\\y^s\\\vdots\\x^s\\y^s\end{bmatrix}\right\} \tag{A.16}$$

which, after application of $\mathbf{Dg}$ becomes:

$$g_c\begin{bmatrix}h(x^s)&0&0&0&0&0&0&0\\0&0&0&0&0&0&0&0\\0&0&h(x^s)&0&0&0&0&0\\0&0&0&0&0&0&0&0\\0&0&0&0&h(x^s)&0&0&0\\0&0&0&0&0&0&0&0\\0&0&0&0&0&0&h(x^s)&0\\0&0&0&0&0&0&0&0\end{bmatrix}\left(\begin{bmatrix}0&1&0&1\\1&0&1&0\\0&1&0&1\\1&0&1&0\end{bmatrix}\otimes\begin{bmatrix}\zeta&0\\0&0\end{bmatrix}\begin{bmatrix}x^s\\y^s\\\vdots\\x^s\\y^s\end{bmatrix}\right) \tag{A.17}$$

simplifying we obtain:

$$g_c\begin{bmatrix}h(x^s)&0&0&0&0&0&0&0\\0&0&0&0&0&0&0&0\\0&0&h(x^s)&0&0&0&0&0\\0&0&0&0&0&0&0&0\\0&0&0&0&h(x^s)&0&0&0\\0&0&0&0&0&0&0&0\\0&0&0&0&0&0&h(x^s)&0\\0&0&0&0&0&0&0&0\end{bmatrix}\begin{bmatrix}\zeta(x^s)+\zeta(x^s)\\0\\\zeta(x^s)+\zeta(x^s)\\0\\\zeta(x^s)+\zeta(x^s)\\0\\\zeta(x^s)+\zeta(x^s)\\0\end{bmatrix} \tag{A.18}$$

which is symply

$$g_c k_n \mathbf{T}(\mathbf{x}^s)\mathbf{C}(\mathbf{x}^s) \tag{A.19}$$

where in this case, the number of links that each node has is $k_n = 2$. Now, we linearize $\mathbf{x}^i$ around the synchronized state $\mathbf{x}^s$

$$\mathbf{x}^i \approx \mathbf{F}(\mathbf{x}^s) + D\mathbf{F}\big|_{\mathbf{x}^s}\delta\mathbf{x}^i - g_c D\Big[\mathbf{T}(\mathbf{x}^i)\sum_j a_{ij}\mathbf{C}(\mathbf{x}^j)\Big]\delta\mathbf{x}^k\,, \tag{A.20}$$

where $k=(i,j)$ depending on whether the Jacobian matrix D acts on a function of $\mathbf{x}^i$ or $\mathbf{x}^j$. Evaluating the last term yields

$$D[\mathbf{T}(\mathbf{x}^i)\sum_j a_{ij}\mathbf{C}(\mathbf{x}^j)]\delta\mathbf{x}^k = D\begin{bmatrix}h(x^i)\sum_j a_{ij}\zeta(x^j)\\0\end{bmatrix}\delta\mathbf{x}_k \tag{A.21}$$

$$=\begin{bmatrix}\frac{\partial h(x^i)}{\partial x^i}\sum_j a_{ij}\zeta(x^j)&0\\0&0\end{bmatrix}\delta\mathbf{x}^i + \begin{bmatrix}h(x^i)\sum_j a_{ij}\frac{\partial\zeta(x^j)}{\partial x^i}&0\\0&0\end{bmatrix}\delta\mathbf{x}^j \tag{A.22}$$

$$= \begin{bmatrix} \frac{\partial h(x^i)}{\partial x^i} k_n \zeta(x^j) & 0 \\ 0 & 0 \end{bmatrix} \Bigg|_{\mathbf{x}^s} \delta\mathbf{x}^i + \begin{bmatrix} h(x^i) \sum_j a_{ij} \frac{\partial \zeta(x^j)}{\partial x^i} & 0 \\ 0 & 0 \end{bmatrix} \Bigg|_{\mathbf{x}^s} \delta\mathbf{x}^j \tag{A.23}$$

which is

$$g_c k_n D\mathbf{H}\big|_{\mathbf{x}^s} \mathbf{K}(\mathbf{x}^s)\delta\mathbf{x}^i - g_c \mathbf{T}(\mathbf{x}^s) \sum_j a_{ij} D\mathbf{C}\big|_{\mathbf{x}^s} \delta\mathbf{x}^j \; . \tag{A.24}$$

Then, we can write $\delta\mathbf{x}^i$ as

$$\delta\mathbf{x}^i = D\mathbf{F}\big|_{\mathbf{x}^s} - g_c k_n D\mathbf{H}\big|_{\mathbf{x}^s} \mathbf{K}(\mathbf{x}^s)\delta\mathbf{x}^i - g_c \mathbf{T}(\mathbf{x}^s) \sum_j a_{ij} D\mathbf{C}\big|_{\mathbf{x}^s} \delta\mathbf{x}^j \; . \tag{A.25}$$

and finally, we write $\delta\mathbf{x} = [\delta\mathbf{x}^1, ..., \delta\mathbf{x}^N]^T$ as

$$\delta\dot{\mathbf{x}} = \{[\mathbf{I}_N \otimes D\mathbf{F}\big|_{\mathbf{x}^s} - g_c k_n D\mathbf{H}\big|_{\mathbf{x}^s} \mathbf{K}(\mathbf{x}^s))] - g_c A \otimes \mathbf{T}(\mathbf{x}^s) D\mathbf{C}\big|_{\mathbf{x}^s}\}\delta\dot{\mathbf{x}} \; . \tag{A.26}$$

The diagonalization of A leads to the desired block diagonalized variational equation:

$$\dot{\eta} = \{[\mathbf{I}_N \otimes (D\mathbf{F}\big|_{\mathbf{x}^s} - g_c k_n D\mathbf{H}\big|_{\mathbf{x}^s} \mathbf{K}(\mathbf{x}^s))] - g_c \Gamma \otimes \mathbf{T}(\mathbf{x}^s) D\mathbf{C}\big|_{\mathbf{x}^s}\}\eta \; . \tag{A.27}$$

B Supplementary Material to Chapter 4

B.1 Selection and properties of the sigma points

For a system with N_x state variables, the mean and covariance of the sigma points are given by [149]:

$$\mu = \sum_{i=0}^{2N_x} w_i^m \psi_i \tag{B.1}$$

$$\Sigma = \sum_{i=0}^{2N_x} w_i^c (\psi_i - \mu)(\psi_i - \mu)^T \,. \tag{B.2}$$

These points are attained to the following constraints:

$$1 = \sum_i w_i^m \tag{B.3}$$

$$1 = \sum_i w_i^m \tag{B.4}$$

$$\mu = \sum_i w_i^m f(\chi)_i \tag{B.5}$$

$$\Sigma = \sum_i w_i^c (f(\chi)_i - \mu)(f(\chi)_i - \mu)^t \tag{B.6}$$

For a system with N_x state variables, we calculate $2n + 1$ sigma points with

$$\chi_0 = \mu \tag{B.7}$$

$$\chi_i = \mu + (\sqrt{N_x \Sigma})_i \quad \text{for } i = 1, 2, \ldots, n \tag{B.8}$$

$$\chi_{n+i} = \mu - (\sqrt{N_x \Sigma})_i \quad \text{for } i = 1, 2, \ldots, n \tag{B.9}$$

where $(\sqrt{N_x \Sigma})_i$ is the ith row of the matrix square root of $N_x \Sigma$) [113].

C Supplementary Material to Chapter 5

C.1 Topologies and synchronization quantification

The network topologies considered when studying electrical coupling between nodes are presented in Fig. C.1. The black links represent undirected connections between nodes, so the resulting adjacency matrices are symmetric ($A = A^T$). The simulated time evolution of the membrane potentials of all nodes for each network topology is also shown in Fig. C.1 on the right side, together with two synchronization measures, the Kuramoto order parameter [13]R and the synchronization error Err.

To evaluate the Kuramoto order parameter, we assign a phase ϕ for each neuron time series that grows linearly at each spike with a gain of 2π as defined in Ivanchenko et al. [144]. The Kuramoto order parameter is given by

$$R = \frac{\left\langle \left| \sum_{j=1}^{N} e^{i\phi_j(t)} \right| \right\rangle_t}{N} , \tag{C.1}$$

where N is the number of oscillators considered in the measure and the average is taken over time. For totally synchronized systems, $R = 1$. For totally unsynchronized systems, $R \approx 0$.

Likewise, the synchronization error gives us an idea of how synchronized the system is, we apply it directly to the time series. First, we calculate the average membrane potential $\bar{x}$ of all oscillators in the network. Then, we compute how much each oscillator deviates from $\bar{x}$. Thus, the synchronization error is computed as

$$Err = \left\langle \frac{\sum_{i=1}^{N} |x_i(t) - \bar{x}(t)|}{N} \right\rangle_t . \tag{C.2}$$

Hence, $Err = 0$ in the case of total synchronization, where $x_i = x_j, \forall\ (i, j) \in [1, N]$. While for unsynchronized systems, Err may assume large values.

When both electrical and chemical coupling between nodes are considered, we use the topologies presented in Fig. C.2. The adjacency matrices are not symmetric ($A \neq A^T$), and

all the networks are heterogeneous, meaning that the nodes have a different number of connections. The simulated time evolution of the membrane potentials of all nodes for each network topology is also shown in Fig. C.2 on the right side.

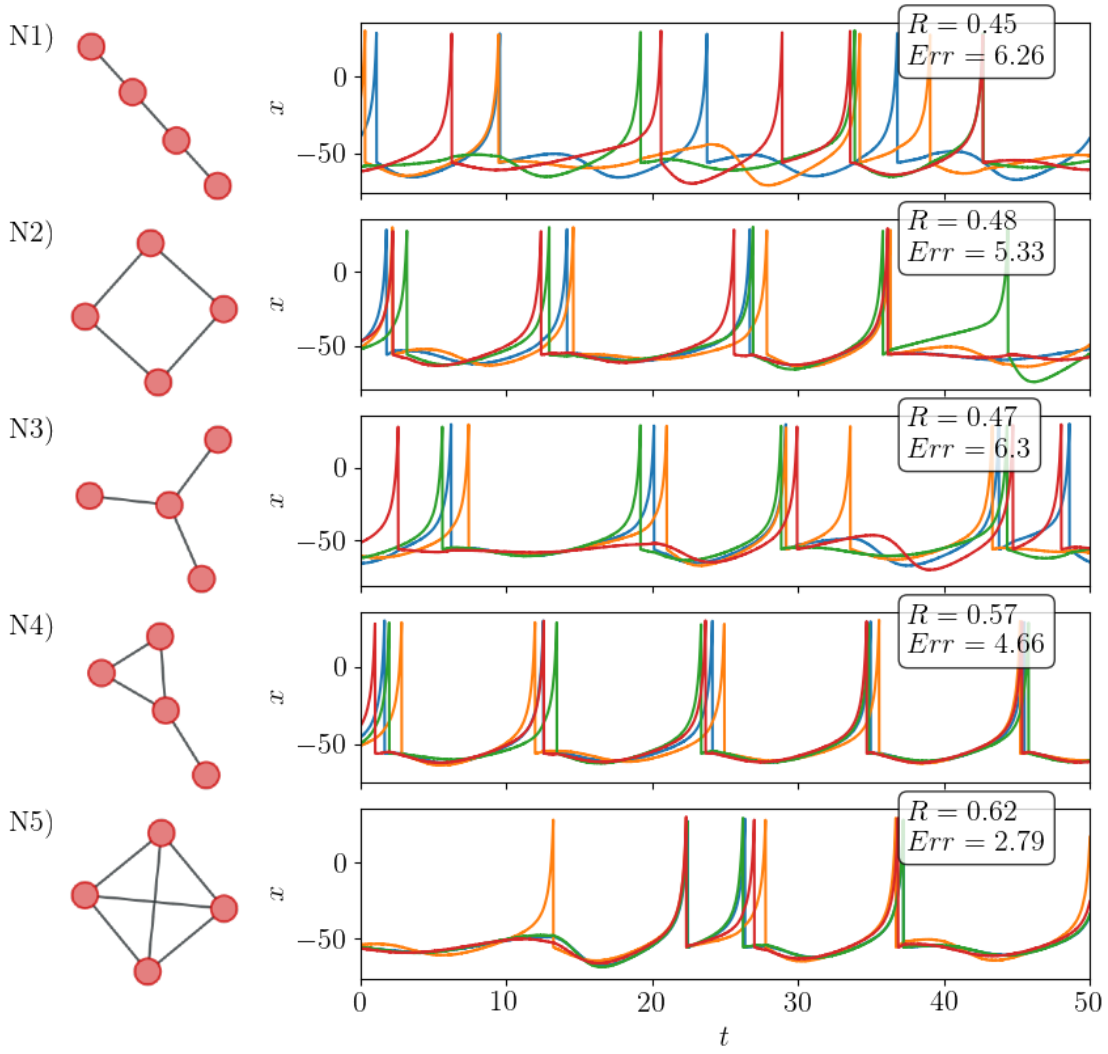

Figure C.1: The five network topologies used when considering only electrical coupling (Eqs. (3.1) and (6.3)). The links between nodes are represented by black lines. For each case, we show the network's dynamics with $g_e = 0.05$. The insets show the Kuramoto order parameter R and the synchronization error Err.

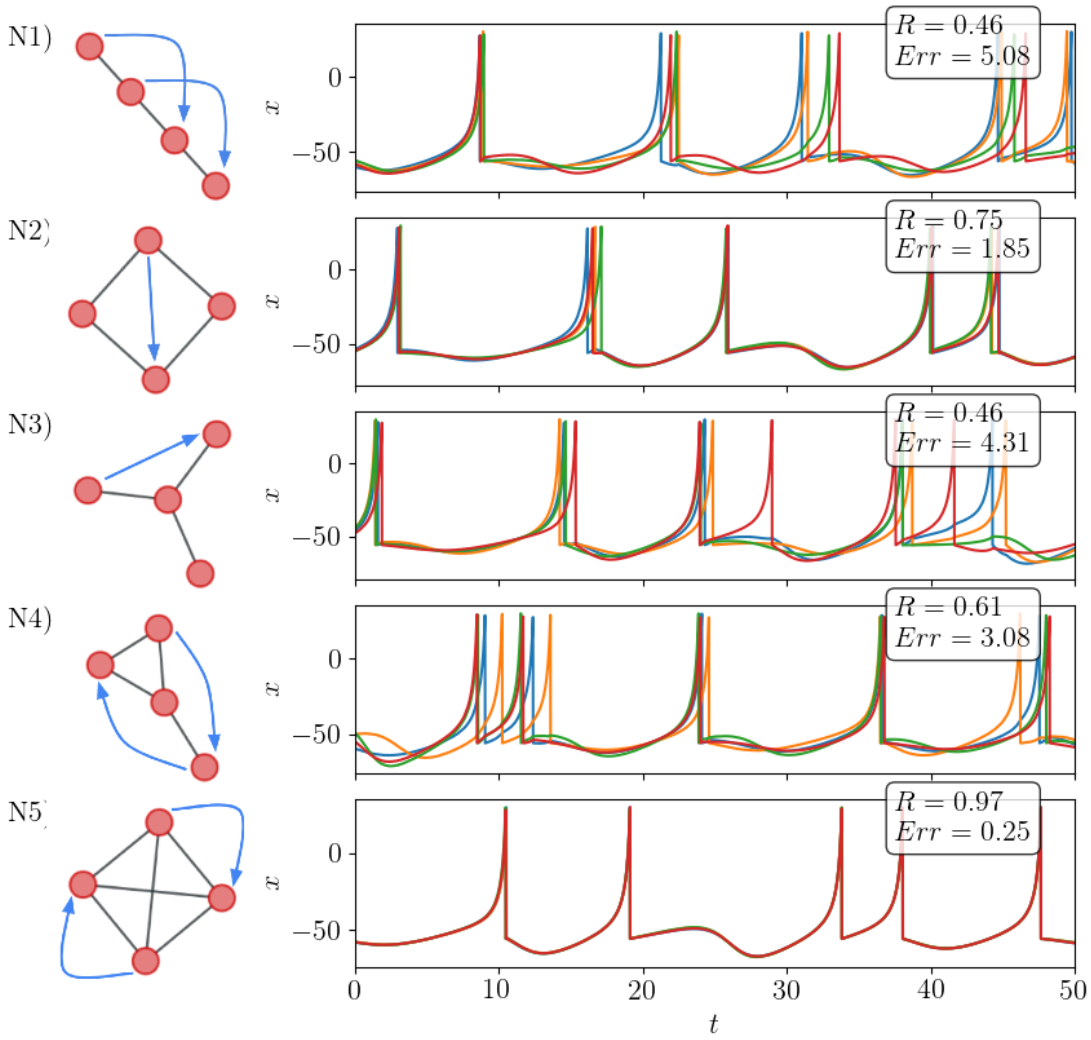

Figure C.2: The five network topologies used when considering both electrical and chemical coupling (Eqs. (3.1), (6.3), and (5.4)), the undirected links are electrical, and the directed links are chemical. The left column displays the network's dynamics with $g_e = 0.10$ and $g_c = 0.05$. The insets show the Kuramoto order parameter R and the synchronization error Err.

D

Supplementary Material to Chapter 6

D.1 Estimation of the average frequency $\bar{\omega}$

As explained in the main text, Sec. 6.2.4, we aim to assimilate the phase time series to the Kuramoto model (Eq. (6.5)) and an important step is to select the natural frequency of the oscillators, $\bar{\omega}$. Here we discuss three methods to estimate $\bar{\omega}$ from the data and how they impact the final result of the network inference.

Method 1. For each coupling strength K_m, we estimate $\bar{\omega}$ as $\bar{\omega}_{K_m} = \bar{\phi}(t_f)/t_f$, where $\bar{\phi}(t)$ represents the average phase of the N oscillators at time t_f.

This method was used in Sec. 6.3.1 with the Izhikevich neurons data and partially with the experimental data in Sec. 6.3.2. As discussed in the main text, for the Rössler data, this approach only works for small coupling. We verified this in Fig. D.1(a), where we measure the reconstruction accuracy in terms of AUC. As we can see, the algorithm performance decreases as the coupling strength increases beyond $K = 11$. On the contrary, in the case of the Izhikevich neurons (b), the method displays good performance.

An inspection of the distribution of the average inter-event intervals (spikes or crossings) allows us to better understand why the UKF method does not perform for high coupling in the electronic circuits. As we see in Fig. D.2(a), in the case of electronic circuits, for high coupling, the intervals become nearly identical. Thus, all circuits have approximately the same frequency, there is no need for the coupling term $\sum_{j=1}^{N} m_{ij} \sin(\phi_j - \phi_i)$. In other words, when the oscillators have very similar frequencies, the model $\dot{\phi} = \bar{\omega}$ is sufficient for the assimilation of the data. In contrast, for a network of $N = 6$ Izhikevich neurons with 8 links, Fig. D.2(b), the distribution of the average inter-spike intervals remains broad in the range of coupling values considered. Hence, the coupling term $\sum_{j=1}^{N} m_{ij} \sin(\phi_j - \phi_i)$ is needed to assimilate the phase time series to the Kuramoto model. The same behavior was observed in other neural networks. This interplay between the level of synchronization and the performance of the network inference was also found in [150] where it was verified that synchronization can deteriorate the network inference.

Method 2. We select $\bar{\omega}$ as the average frequency computed from the dynamics of the

uncoupled oscillators ($K = 0$). As we see in Fig. D.1, for low couplings the UKF performance is not as good as with Method 1, but it is stable around AUC $= 0.75$ for high coupling. The drawback of this method is that it requires the availability of data with no coupling. However, one can always estimate $\bar{\omega}$ from the lowest coupling available.

Method 3. We assume that all the oscillators have a natural frequency $\bar{\omega} = 0$. This means that Eq. (6.5) is reduced to the coupling term. We see in Fig. D.1 that this method performs similarly as Method 2, being slightly worse for high coupling values.

Taken together, the results in Figs. D.1 and D.2 show that, if the nodes (the neurons or the chaotic circuits) have not identical frequencies, the UKF approach, estimating $\bar{\omega}$ either with Methods 1, 2, or 3, generally outperforms the results of using both cross-correlation (CC) and mutual information (MI).

As a final remark, $\bar{\omega}$ could have been an additional parameter to estimate using UKF, with the governing equation given by $d\bar{\omega}/dt = 0$. However, we found that this approach did not improve the performance.

D.2 Influence of the network size and link density

Here we compare the results of the network inference using UKF, MI, and CC for different network sizes $N = [6, 10, 16, 28]$ and link densities $p = [0.5, 0.5, 0.25, 0.15]$. For each set (N, p) we generated 50 random networks and simulated the Izhikevich model with a coupling strength K such that the networks have a similar level of synchronization, as measured by the average Kuramoto order parameter, $\bar{R} = 0.85$. For each network, we calculated the F_1 and averaged the result over the different networks. As the computational cost of the UKF algorithm grows rapidly (see Sec. D.4), we did not repeat the simulations to estimate the F_1 statistics.

The results are displayed in Fig. D.3. Although UKF yields better results for all network sizes considered, we see that the performance of all three methods decreases as N increases.

Regarding the role of the link density, p, we show in Fig. D.4 the average F_1 score for networks with low and higher p. For $p = 0.25$, for low coupling $K < 0.03$, the three methods have poor performance, with the MI yielding the best results. For higher coupling, both UKF and MI yield a generally good F_1 score, with UKF being the best method across the coupling range. For $p = 0.75$, given the higher number of links (11), to be detected even the CC yields a good result. It also comes as a result of the clustering algorithm, which sets the highest values as links. Again, here for weak coupling MI yields the best results, while for higher coupling, UKF yields the best performance.

D.3 Influence of the length of the time series

In the main text, for Izhikevich neurons, we presented results of the analysis of time series of $L = 40000$ data points. Here, we report the results for shorter time series, and therefore, for a smaller number of spikes. To do so, we considered the same networks, coupling

strengths, and transient as in the main text, the only difference being the length of the time series analyzed.

Figure D.5 display the F_1 score (averaged over 50 simulations) for $L = 20000$ (a) and for $L = 10000$ (b). In both cases, the UKF algorithm yields better results for $K \geq 0.03$.

D.4 Computational costs

Here we report a brief analysis of the computational cost (tested on Intel Xeon Processor Skylake - 2.2GHz) of the network inference for different network sizes. The results are shown in Fig. D.6, where for each network size N, 20 networks with link density $p = 0.5$ were generated, and their dynamics were recorded in time series of length $L = 40000$ points. The time spent by each algorithm (UKF, MI, CC) to analyze the time series (without counting the binarization of the output) was measured using the *Python* library *time*. As expected, CC and MI, have a much smaller computational cost, since they only measure pairwise relations between the $N(N-1)/2$ pairs of time series. Meanwhile, UKF analyzes N time series simultaneously, assimilating them to a model in order to obtain the best fit for each model's parameters. For this reason, it requires a significantly longer time than the other two algorithms.

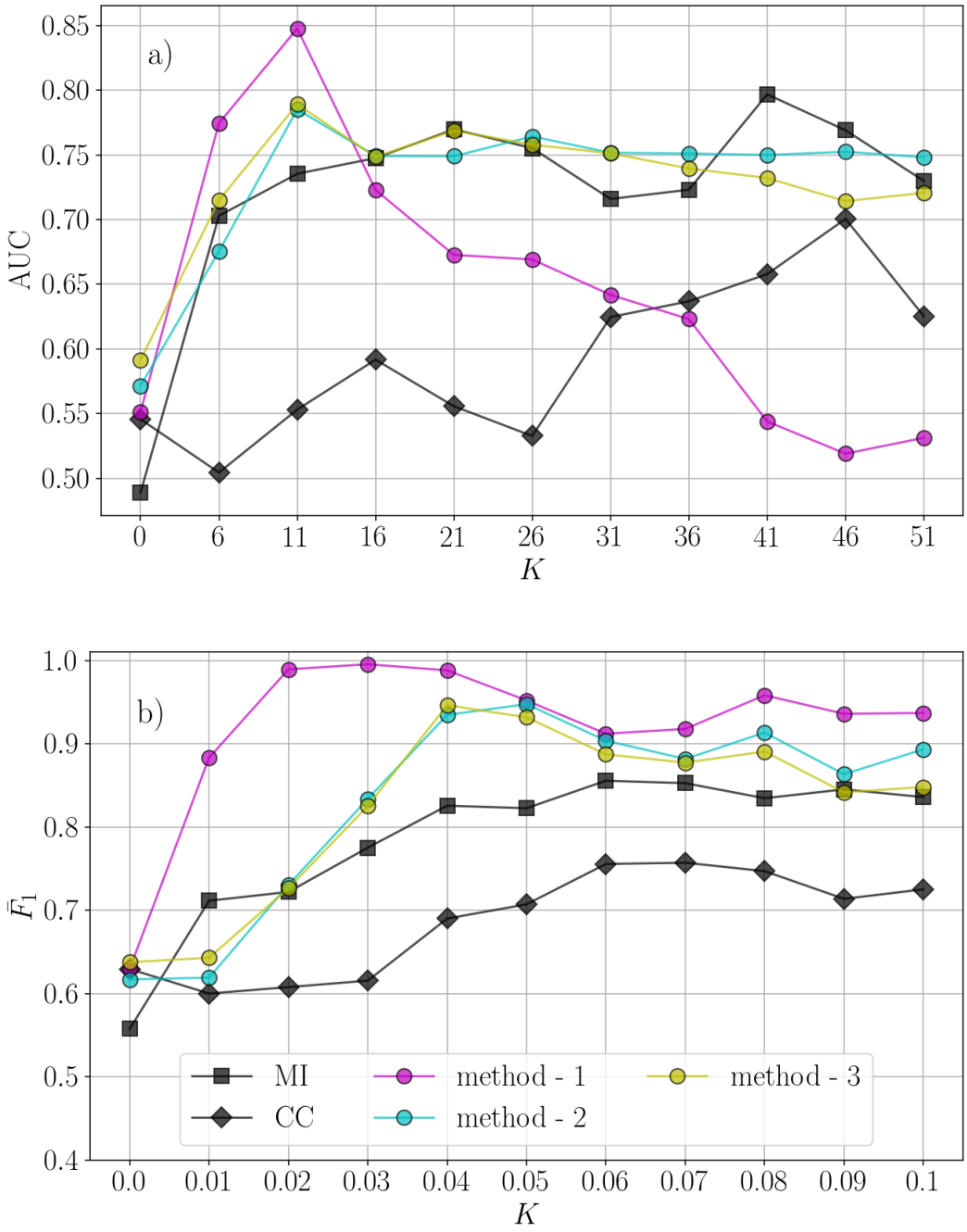

Figure D.1: Comparison of the UKF performance with three methods for estimating the average frequency $\bar{\omega}$, in colored lines. The grey lines display the MI and CC performances. (a) For the electronic circuits, AUC is used to quantify performance. (b) For the Izhikevich neurons, F_1 is used to quantify performance.

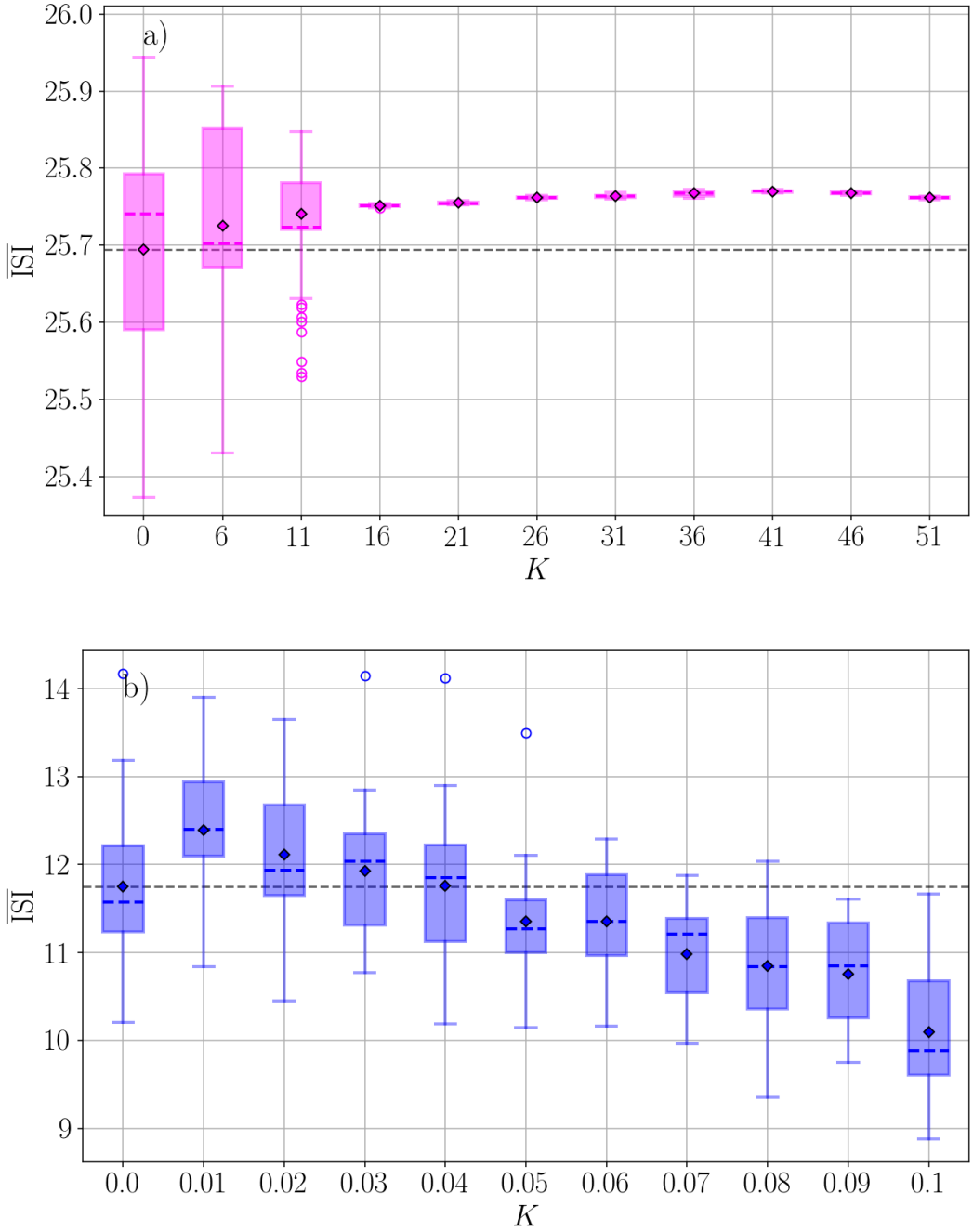

Figure D.2: Distribution of average inter-event-intervals of the electronic circuits (a) and average inter-spike-intervals of a network of $N = 6$ Izhikevich neurons with 8 links (b) as a function of the coupling strength K. The horizontal dashed line marks the average value at zero coupling.

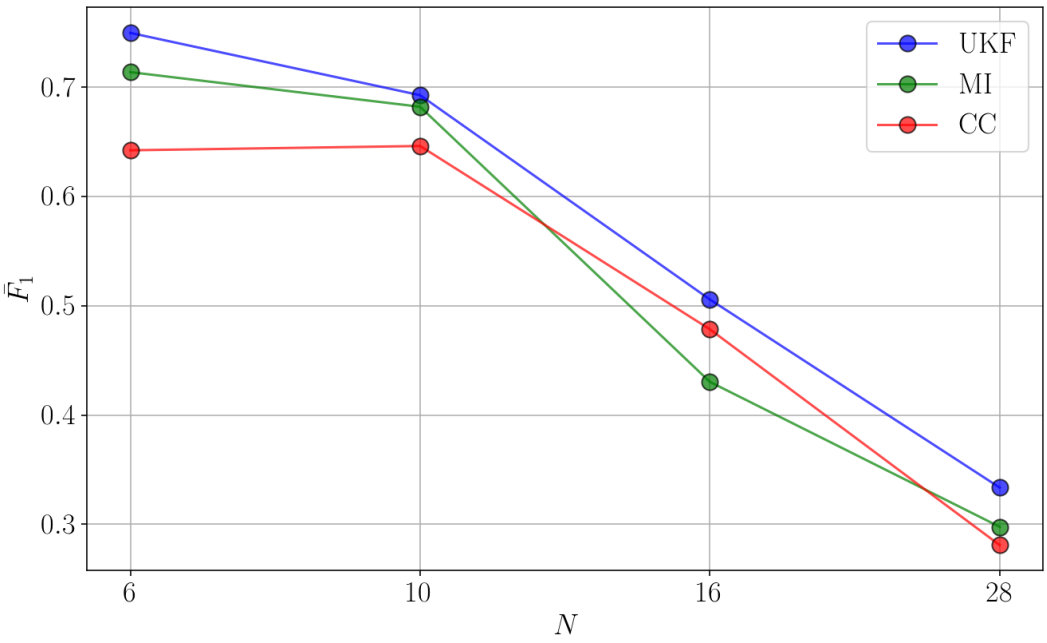

Figure D.3: Performance of UKF, MI, and CC for Izhikevich neurons, considering different network sizes. The values of p and K are such that, for each network size N, the average Kuramoto order parameter is $\bar{R} = 0.85$.

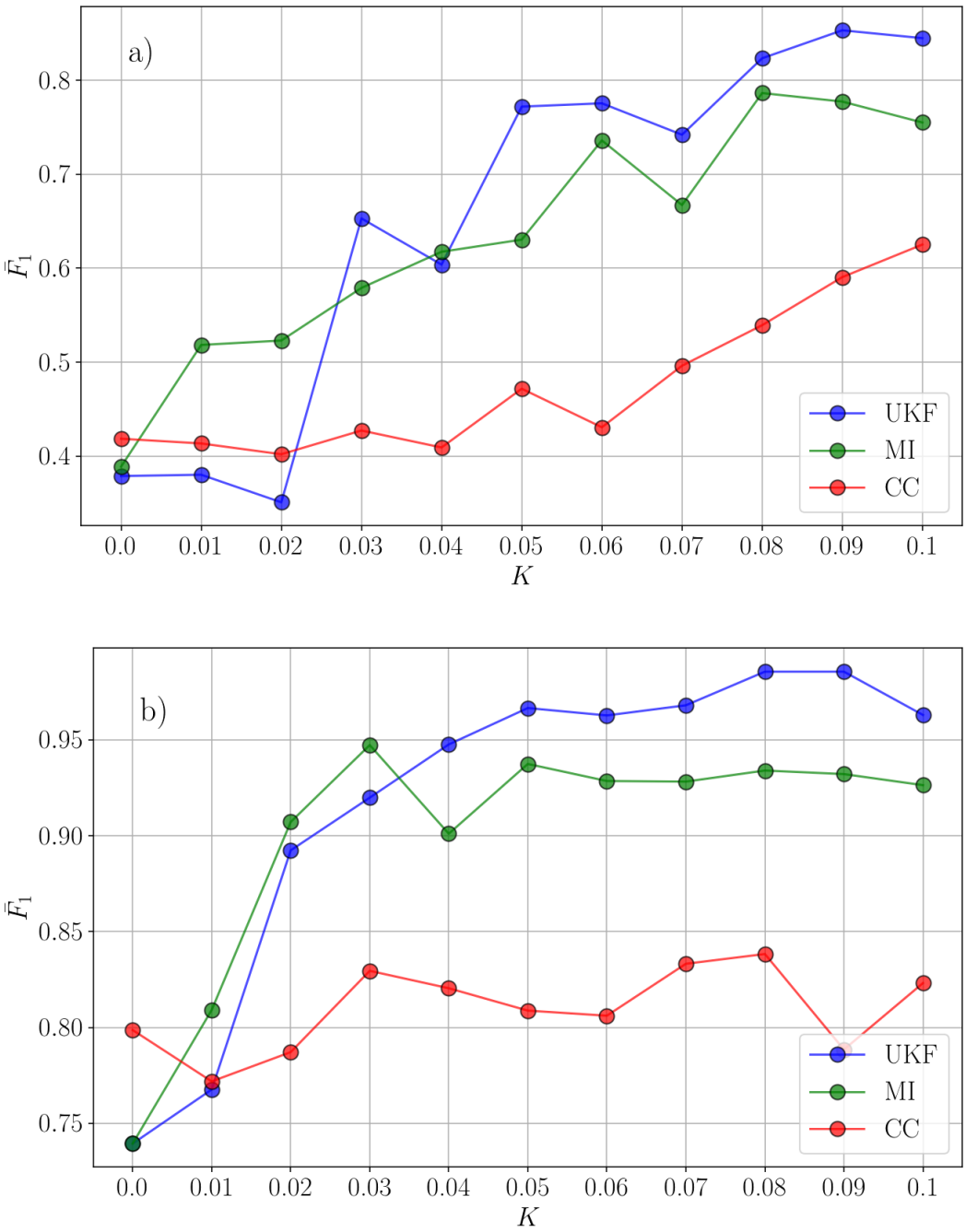

Figure D.4: Performance of UKF, MI, and CC algorithms for two link densities as a function of the coupling strength. Each curve represents the F_1 score averaged over the different networks and different trials. (a) Results for link density $p = 0.25$ and 7 networks, (b) for $p = 0.75$ and 9 networks.

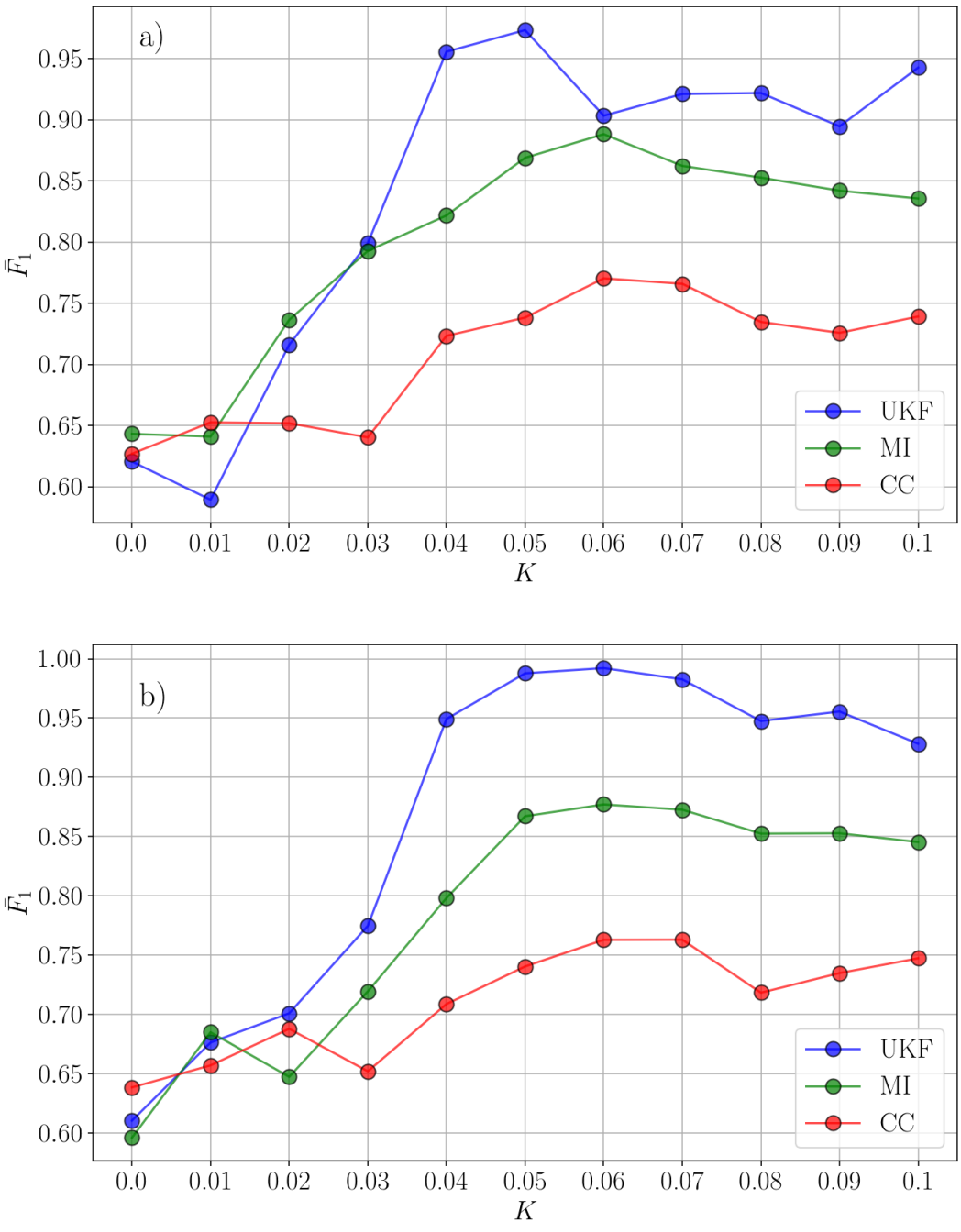

Figure D.5: Performance of UKF, MI, and CC as a function of the coupling strength K for networks of $N = 6$ Izhikevich neurons, when the time series length is (a) $L = 10000$, (b) $L = 20000$.

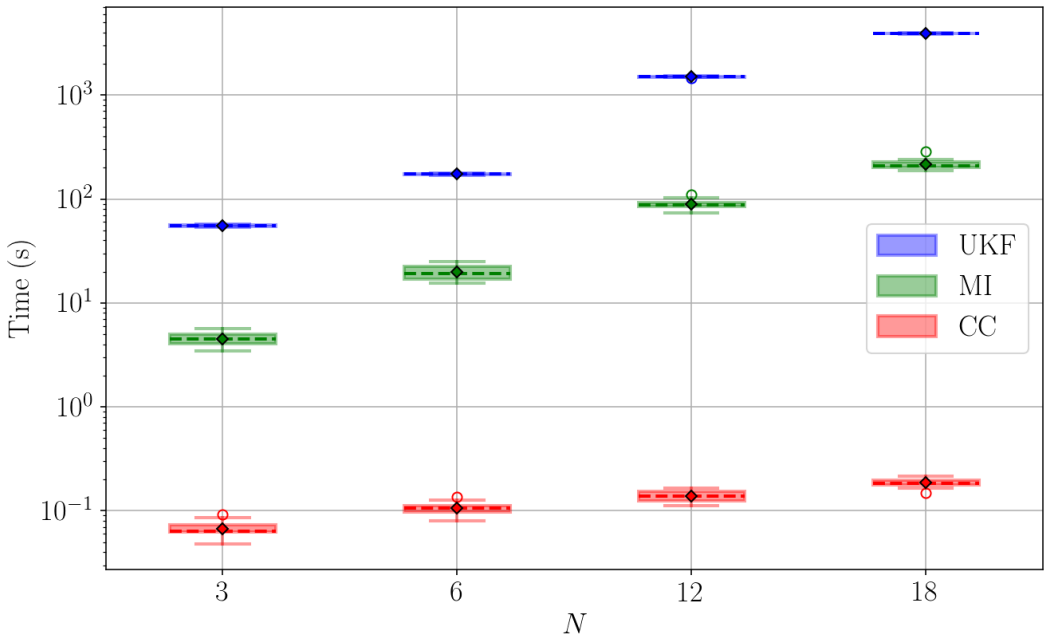

Figure D.6: Comparison of the computational time of UKF, MI and CC algorithms for three network sizes, N. For each N, 20 networks with link density $p = 0.5$ were used. Each boxplot represents the CPU time required to infer m_{ij}, MI_{ij}, and CC_{ij}.

Bibliography

[1] D. Purves et al. *Neuroscience*. Oxford University Press, 2009.

[2] A. L. Hodgkin and A. F. Huxley. "A Quantitative Description of Membrane Current and Its Application to Conduction and Excitation in Nerve". In: *J. Physiol.* 117.4 (1952), p. 500.

[3] E. M. Izhikevich. "Simple Model of Spiking Neurons". In: *IEEE Trans. Neural Netw.* 14.6 (2003), p. 1569.

[4] E. M. Izhikevich and G. M. Edelman. "Large-Scale Model of Mammalian Thalamocortical Systems". In: *Proc. Natl. Acad. Sci. U.S.A.* 105.9 (2008), p. 3593.

[5] J. Modolo, E. Mosekilde, and A. Beuter. "Synchronization of Coupled Neurons with Heterogeneous Time Delays". In: *J. Physiol. Paris* 101.1 (2007), p. 56.

[6] G. Buzsáki. *Rhythms of the Brain*. Oxford University Press, 2006.

[7] A. Pikovsky, M. Rosenblum, and J. Kurths. *Synchronization: A Universal Concept in Nonlinear Sciences*. Cambridge University Press, 2001.

[8] Michael Rosenblum and Arkady Pikovsky. "Synchronization: From pendulum clocks to chaotic lasers and chemical oscillators". In: *Contemporary Physics* 44.5 (2003), pp. 401–416.

[9] Christopher P. Fall et al. *Computational Cell Biology*. Springer Science & Business Media, 2007.

[10] A. T. Winfree. "Biological rhythms and the behavior of populations of coupled oscillators". In: *Journal of Theoretical Biology* 16 (1967), pp. 15–42.

[11] Renato E. Mirollo and Steven H. Strogatz. "Synchronization of Pulse-Coupled Biological Oscillators". In: *SIAM Journal on Applied Mathematics* 50.6 (1990), pp. 1645–1662.

[12] Y. Kuramoto. "Self-entrainment of a population of coupled non-linear oscillators". In: *International Symposium on Mathematical Problems in Theoretical Physics, Lecture Notes in Physics* 39 (1975), p. 420.

[13] Y. Kuramoto. *Chemical oscillations, waves and turbulence*. Springer, New York, 1984.

[14] L. M. Pecora and T. L. Carroll. "Synchronization in Chaotic Systems". In: *Phys. Rev. Lett.* 80.10 (1998), p. 2109.

[15] W. Singer. "Neuronal Synchrony: A Versatile Code for the Definition of Relations?" In: *Neuron* 24 (1999), p. 49.

[16] P. Fries. "Neuronal Gamma-Band Synchronization as a Fundamental Process in Cortical Computation". In: *Annu. Rev. Neurosci.* 32 (2009), pp. 209–224.

[17] J. R. Cohen and M. D'Esposito. "The Segregation and Integration of Distinct Brain Networks and Their Relationship to Cognition". In: *J. Neurosci.* 36.48 (2016), p. 12083.

[18] N. Axmacher et al. "Memory Formation by Neuronal Synchronization". In: *Brain Res. Rev.* 52.1 (2006), p. 170.

[19] P. Uhlhaas and W. Singer. "Neural Synchrony in Brain Disorders: Relevance for Cognitive Dysfunctions and Pathophysiology". In: *Neuron* 52 (2006), pp. 155–168.

[20] P. Uhlhaas and W. Singer. "Neuronal Dynamics and Neuropsychiatric Disorders: Toward a Translational Paradigm for Dysfunctional Large-Scale Networks". In: *Neuron* 52 (2006), p. 155.

[21] P. Jiruska et al. "Synchronization and desynchronization in epilepsy: controversies and hypotheses". In: *J. Physiol.* 594.4 (2013), pp. 787–797.

[22] N. Lainscske C.and Rungratsameetaweemana, S. S. Cash, and T. J. Sejnowski. "Cortical chimera states predict epileptic seizures". In: *Chaos* 29 (2019), p. 121106.

[23] R. J. Meinhold and N. D. Singpurwalla. "Understanding the Kalman Filter". In: *Am. Stat.* 37.2 (1983), pp. 123–127.

[24] F. Takens. "Detecting strange attractors in turbulence". In: *Symposium on Dynamical Systems and Turbulence*. Ed. by D. A. Rand and L. S. Young. Springer-Verlag, 1981, pp. 366–381.

[25] Ethan R Deyle and George Sugihara. "Generalized theorems for nonlinear state space reconstruction". In: *PLoS One* 6.3 (2011).

[26] Riet De Smet and Kathleen Marchal. "Advantages and limitations of current network inference methods". In: *Nature Reviews Microbiology* 8 (2010), pp. 717–729.

[27] Caroline Siegenthaler and Rudiyanto Gunawan. "Assessment of Network Inference Methods: How to Cope with an Underdetermined Problem". In: *PLOS ONE* 9.3 (2014), e90481.

[28] Ivan Brugere, Brian Gallagher, and Tanya Y. Berger-Wolf. "Network Structure Inference, A Survey: Motivations, Methods, and Applications". In: *ACM Computing Surveys* 51.2 (2018), 24:1–24:39.

[29] L. Peel, T. P. Peixoto, and M. De Domenico. "Statistical inference links data and theory in network science". In: *Nat. Comm.* 13 (2022), p. 6794.

[30] E. Adar and L.A. Adamic. "Tracking information epidemics in blogspace". In: *The 2005 IEEE/WIC/ACM International Conference on Web Intelligence (WI'05)*. 2005, pp. 207–214.

[31] Lucy M Aplin et al. “Social networks predict patch discovery in a wild population of songbirds”. In: *Proceedings of the Royal Society B* 279.1730 (2012), pp. 4199–4205.

[32] Munmun De Choudhury et al. “Inferring Relevant Social Networks from Interpersonal Communication”. In: *Proceedings of the 19th International Conference on World Wide Web*. New York, NY, USA: Association for Computing Machinery, 2010, pp. 301–310.

[33] D. Marbach et al. “Wisdom of crowds for robust gene network inference”. In: *Nature Methods* 9 (2016), p. 796.

[34] J. F. Donges et al. “Complex networks in climate dynamics”. In: *Eur. Phys. J. ST* 174 (2009), pp. 157–179.

[35] H. A. Dijkstra et al. *Networks in Climate*. Cambridge University Press, 2019.

[36] V. M. Eguiluz et al. “Scale-free brain functional networks”. In: *Phys. Rev. Lett.* 94 (2005), p. 018102.

[37] E. Bullmore and O. Sporns. “Complex brain networks: graph theoretical analysis of structural and functional systems”. In: *Nat. Rev. Neurosci.* 10 (2009), p. 186.

[38] Danielle S Bassett and Olaf Sporns. “Network neuroscience”. In: *Nature neuroscience* 20.3 (2017), pp. 353–364.

[39] Federico Battiston et al. “Networks beyond pairwise interactions: structure and dynamics”. In: *Physics Reports* 874 (2020), pp. 1–92.

[40] Amitava Banerjee et al. “Using machine learning to assess short term causal dependence and infer network links”. In: *Chaos* 29 (2019), p. 121104.

[41] Amitava Banerjee et al. “Machine Learning Link Inference of Noisy Delay-Coupled Networks with Optoelectronic Experimental Tests”. In: *Phys. Rev. X* 11 (3 2021), p. 031014.

[42] Amitava Banerjee, Sarthak Chandra, and Edward Ott. “Network inference from short, noisy, low time-resolution, partial measurements: Application to C. elegans neuronal calcium dynamics”. In: *PNAS* 120 (12 2023), e2216030120.

[43] T. P. Peixoto. “Network Reconstruction and Community Detection from Dynamics”. In: *Phys. Rev. Lett.* 123 (2019), p. 128301.

[44] Sach Mukherjee and Terence P. Speed. “Network inference using informative priors”. In: *PNAS* 105 (38 2008), pp. 14313–14318.

[45] Furito Mori and Hiroshi Kori. “Noninvasive inference methods for interaction and noise intensities of coupled oscillators using only spike time data”. In: *PNAS* 19 (6 2022), e2113620119.

[46] M. Rosenblum and A. Pikovsky. “Inferring connectivity of an oscillatory network via the phase dynamics reconstruction”. In: *Front. Netw. Physiol.* 3 (2023), p. 1298228.

[47] Siyang Leng, Ziwei Xu, and Huanfei Ma. “Reconstructing directional causal networks with random forest: Causality meeting machine learning”. In: *Chaos* 29 (2019), p. 093130.

[48] J. Casadiego, D. Maoutsa, and M. Timme. “Inferring Network Connectivity from Event Timing Patterns”. In: *Phys. Rev. Lett.* 121 (2018), p. 054101.

[49] Emily S. C. Ching, Pik-Yin Lai, and C. Y. Leung. “Reconstructing weighted networks from dynamics”. In: *Phys. Rev. E* 91 (3 2015), p. 030801.

[50] N. Rubido et al. “Exact detection of direct links in networks of coupled maps”. In: *New J. of Phys.* 16 (2014), p. 093010.

[51] Marc Timme. “Revealing Network Connectivity from Response Dynamics”. In: *Phys. Rev. Lett.* 98 (22 May 2007), p. 224101.

[52] Jie Sun, Dane Taylor, and Erik M. Bollt. “Causal Network Inference by Optimal Causation Entropy”. In: *SIAM Journal on Applied Dynamical Systems* 14.1 (2015), pp. 73–106.

[53] T. Rings, T. Bröhl, and K. Lehnertz. “Network structure from a characterization of interactions in complex systems”. In: *Sci. Rep.* 12 (2022), p. 11742.

[54] M. Zanin et al. “Optimizing Functional Network Representation of Multivariate Time Series”. In: *Sci. Rep.* 2 (2012), p. 630.

[55] F. Hassanibesheli and R.V. Donner. “Network inference from the timing of events in coupled dynamical systems”. In: *Chaos* 29 (2019), p. 083125.

[56] O. Fajardo-Fontiveros, R. Guimera, and M. Sales-Pardo. “Node Metadata Can Produce Predictability Crossovers in Network Inference Problems”. In: *Phys. Rev. X* 12 (2022), p. 011010.

[57] Mark A. Kramer et al. “Network inference with confidence from multivariate time series”. In: *Phys. Rev. E* 79 (6 June 2009), p. 061916.

[58] Jakob Runge et al. “Escaping the Curse of Dimensionality in Estimating Multivariate Transfer Entropy”. In: *Phys. Rev. Lett.* 108 (25 June 2012), p. 258701.

[59] M. J. Panaggio et al. “Model reconstruction from temporal data for coupled oscillator networks”. In: *Chaos* 29 (2019), p. 103116.

[60] E. Forero-Ortiz et al. “Inferring the connectivity of coupled chaotic oscillators using Kalman filtering”. In: *Sci. Rep.* 11 (2021).

[61] R. E. Kalman. “A new approach to linear filtering and prediction problems”. In: *Journal of Basic Engineering* 82 (1960), p. 35.

[62] O. E. Rössler. “An Equation for Continuous Chaos”. In: *Physics Letters* 57A.5 (1976), pp. 397–398.

[63] J. F. Heagy, T. L. Carroll, and L. M. Pecora. In: *Physical Review E* 50.3 (1994), pp. 1874–1885.

[64] M. Lyapunova. *Problkme G ndral de la Stabilit du Mouve- ment (transl. from Russian).* Vol. 9. Reproduced in Ann. Math. Study, vol. 17, Princeton 1947. 1907, pp. 203–475.

[65] Arkady Pikovsky and Antonio Politi. *Lyapunov Exponents: A Tool to Explore Complex Dynamics.* Cambridge University Press, 2016.

[66] H. Fujisaka and T. Yamada. In: *Progress of Theoretical Physics* **69**.1 (1983), pp. 32–47.

[67] E. E. Shnöl. In: *Prikl. Mat. Mekh.* **51**.9 (1987).

[68] K. Kaneko. "Relevance of dynamic clustering to biological networks". In: *Physica D: Nonlinear Phenomena* **75**.1-3 (1994), pp. 55–73.

[69] J. R. Terry et al. "Synchronization of chaos in an array of three lasers". In: *Physical Review E* **59**.4 (1999), pp. 4036–4043.

[70] T. Nishikawa and A. E. Motter. "Comparative Analysis of Existing Models for Power-Grid Synchronization". In: *Phys. Rev. E* 73.6 (2006), p. 065106.

[71] J. Sun, E. M. Bollt, and T. Nishikawa. "Master Stability Functions for Coupled Nearly Identical Dynamical Systems". In: *Europhys. Lett.* 73.6 (2009), p. 60011.

[72] L. M. Pecora et al. "Cluster synchronization and isolated desynchronization in complex networks with symmetries". In: *Nat. Commun.* 5.4079 (2014).

[73] F. Della Rossa et al. "Critical Transitions in a Game of Opponent, Random, and Social Influence". In: *Nat. Commun.* 11.3179 (2020).

[74] H. V. Henderson, F. Pukelsheim, and S. R. Shayle. "On the history of the kronecker product". In: *Linear and Multilinear Algebra* 14.2 (1983), pp. 113–120.

[75] S. Boccaletti et al. "Complex networks: Structure and dynamics". In: *Physics Reports* 424.4–5 (2006), pp. 175–308.

[76] G. Benettin et al. "Lyapunov Characteristic Exponents for smooth dynamical systems and for hamiltonian systems; a method for computing all of them. Part 1: Theory". In: *Meccanica* 15.1 (1980), p. 9.

[77] P. Checco, M. Biey, and L. Kocarev. "Synchronization in random networks with given expected degree sequences". In: *Chaos, Solitons Fractals* 35.3 (2008), p. 562.

[78] H. Sachs. "Über Teiler, Faktoren und Charakteristische Polynome von Graphen, Teil I". In: *Wiss. Z. TH Ilmenau* 12 (1966), pp. 7–12.

[79] H. Sachs. "Über Teiler, Faktoren und Charakteristische Polynome von Graphen, Teil II". In: *Wiss. Z. TH Ilmenau* 13 (1967), pp. 405–412.

[80] A. J. Schwenk. "Computing the characteristic polynomial of a graph". In: *Graphs and Combinatorics*. Ed. by R. Bari and F. Harary. Springer, 1974, pp. 153–172.

[81] M.T. Schaub et al. "Graph partitions and cluster synchronization in networks of oscillators". In: *Chaos* 26 (2016), p. 094821.

[82] D. M. Cardoso, C. Delorme, and P. Rama. "Laplacian eigenvectors and eigenvalues and almost equitable partitions". In: *Eur. J. Comb.* 28.3 (2007), p. 665.

[83] N. O'Clery et al. "Observability and coarse graining of consensus dynamics through the external equitable partition". In: *Phys. Rev. E* 88.3 (2007), p. 393.

[84] Y. Zhang, V. Latora, and A. E. Motter. "Unified treatment of synchronization patterns in generalized networks with higher-order, multilayer, and temporal interactions". In: *Commun. Phys.* 4.195 (2021).

[85] T. Maehara and K. Murota. "Algorithm for error-controlled simultaneous block-diagonalization of matrices". In: *SIAM Journal on Matrix Analysis and Applications* 32 (2011), pp. 605–620.

[86] J. C. Alexander et al. “Riddled Basins”. In: *Int. J. Bifurc. Chaos* 2.4 (1992), p. 795.

[87] L. Huang et al. “Generic behavior of master-stability functions in coupled nonlinear dynamical systems”. In: *Phys. Rev. E* 80.3 (2009), p. 036204.

[88] S. Nobukawa et al. “Analysis of chaotic resonance in Izhikevich neuron model”. In: *PLOS ONE* 10 (2015).

[89] I. Shimada and T. Nagashima. “A Numerical Approach to Ergodic Problem of Dissipative Dynamical Systems”. In: *Prog. Theor. Phys.* 61.6 (1979), p. 1605.

[90] A. Wolf et al. “Determining Lyapunov exponents from a time series”. In: *Phys. D.* 16.3 (1985), p. 285.

[91] F. Bizzari, A. Brambilla, and G. S. Gajani. “Lyapunov exponents computation for hybrid neurons”. In: *J. Comput. Neurosci.* 35.2 (2013), p. 201.

[92] M. di Bernardo et al. *Piecewise-smooth dynamical systems: theory and applications*. Springer, 2008, p. 106.

[93] D. H. Perkel, B. Mulloney, and R. W. Budelli. “Quantitative methods for predicting neuronal behavior”. In: *Neuroscience* 6.5 (1981), p. 823.

[94] D. Somers and N. Kopell. “Rapid synchronization through fast threshold modulation”. In: *Biol. Cybern.* 68.5 (1993), p. 393.

[95] D. H Root et al. “Single rodent mesohabenular axons release glutamate and GABA”. In: *Nat. Neurosci.* 17.11 (2014), p. 1543.

[96] K. A. Pelkey et al. “Paradoxical network excitation by glutamate release from VGluT3$^+$ GABAergic interneurons”. In: *eLife* 9 (2020), e51995.

[97] P. Checco et al. In: *IEEE Trans. Circuits Syst. II* 55.12 (2008), p. 1274.

[98] M. D. Shrimali et al. “The nature of attractor basins in multistable systems”. In: *Int. J. Bifurc. Chaos* 18.6 (2008), p. 1607.

[99] Edward Ott and John C. Sommerer. “Blowout bifurcations: the occurrence of riddled basins and on-off intermittency”. In: *Physics Letters A* 188.1 (1994), pp. 39–47.

[100] Steven W. McDonald et al. “Fractal basin boundaries”. In: *Physica D: Nonlinear Phenomena* 17.2 (1985), pp. 125–153.

[101] Celso Grebogi et al. “Exterior dimension of fat fractals”. In: *Physics Letters A* 110.1 (1985), pp. 1–4.

[102] Ujjwal SR et al. “Driving-induced multistability in coupled chaotic oscillators: Symmetries and riddled basins”. In: *Chaos* 26.6 (2016), p. 063111.

[103] L. M. Pecora et al. “Complete characterization of the stability of cluster synchronization in complex dynamical networks”. In: *Sci. Adv.* 2.4 (2016).

[104] E. H. Moore. “On the Reciprocal of the General Algebraic Matrix”. In: *Bull. Amer. Math. Soc* 26 (1920), p. 394.

[105] R. Penrose. “A Generalized Inverse for Matrices.” In: *Math. Proc. Camb. Philos. Soc.* **51**.3 (1955), p. 406.

[106] Daniel J. Gauthier and Joshua C. Bienfang. "Intermittent Loss of Synchronization in Coupled Chaotic Oscillators: Toward a New Criterion for High-Quality Synchronization". In: *Phys. Rev. Lett.* 77 (1996), p. 1751.

[107] Paul Zarchan and Howard Musoff. *Progress in Astronautics and Aeronautics: Fundamentals of Kalman Filtering - A Practical Approach*. Vol. 232. AIAA, 2009.

[108] Robert H. Shumway and David S. Stoffer. "An Approach to Time Series Smoothing and Forecasting Using the EM Algorithm". In: *Journal of Time Series Analysis* 3.4 (1982), pp. 253–264.

[109] DSc Eli Brookner. *Tracking and Kalman Filtering Made Easy*. John Wiley & Sons, Inc., 1998.

[110] Roger R. Labbe. *Kalman and Bayesian Filters in Python*. https://github.com/rlabbe/Kalman-and-Bayesian-Filters-in-Python. Accessed: 10-10-2023. 2015.

[111] H. Masnadi-Shirazi, A. Masnadi-Shirazi, and M.-A. Dastgheib. "A Step by Step Mathematical Derivation and Tutorial on Kalman Filters". In: *arXiv* (2019). arXiv: 1910.03558.

[112] Simon J. Julier and Jeffrey K. Uhlmann. "New extension of the Kalman filter to nonlinear systems". In: *Signal Processing, Sensor Fusion, and Target Recognition VI*. Ed. by Ivan Kadar. Vol. 3068. International Society for Optics and Photonics. SPIE, 1997, pp. 182–193.

[113] S.J. Julier and J.K. Uhlmann. "Unscented filtering and nonlinear estimation". In: *Proceedings of the IEEE* 92.3 (2004), pp. 401–422.

[114] C. M. Trudinger et al. "Using the Kalman filter for parameter estimation in biogeochemical models". In: *Environmetrics* 19 (8 2008), p. 849.

[115] B Y Hugh L Bryant and Josr P Segundo. "Spike Initiation by Transmembrane Current: A White-Noise Analysis". In: *The Journal of Physiology* 260 (1976), pp. 279–314.

[116] David Sterratt et al. *Principles of Computational Modelling in Neuroscience*. Cambridge University Press, 2011.

[117] M. Goodfellow et al. "What models and tools can contribute to a better understanding of brain activity?" In: *Frontiers in Network Physiology* 2 (2022), p. 907995.

[118] J. Bechhoefer. *Control Theory for Physicists*. Cambridge University Press, 2021.

[119] E. R. Kalman. "A New Approach to Linear Filtering and Prediction Problem". In: *J. Basic Eng.* 82 (1960), pp. 35–45.

[120] S. Haykin. *Neural Networks and Learning Machines*. Pearson Education, Inc., 2009, p. 906.

[121] C.M. Bishop. *Pattern Recognition and Machine Learning*. Information Science and Statistics. Springer New York, 2016.

[122] Steven L. Brunton and J. Nathan Kutz. *Data-driven science and engineering: machine learning, dynamical systems, and control*. Cambridge University Press, 2019.

[123] Z. Li et al. "Unscented Kalman Filter for Brain-Machine Interfaces". In: *Plos One* 4 (2009), e6243.

[124] J. L. Contreras-Vidal et al. "Neural Decoding of Robot-Assisted Gait During Rehabilitation After Stroke". In: *Am. J. of Phys. Med. & Rehab.* 97 (2018), pp. 541–550.

[125] S. R. Nason et al. "Real-time linear prediction of simultaneous and independent movements of two finger groups using an intracortical brain-machine interface". In: *Neuron* 109 (2021), pp. 3164–3177.

[126] Matthew J. Moye and Casey O. Diekman. "Data Assimilation Methods for Neuronal State and Parameter Estimation". In: *J. of Math. Neuroscience* 8 (2018), p. 11.

[127] O. J. Walch and M. C. Eisenberg. "Parameter identifiability and identifiable combinations in generalized Hodgkin-Huxley models". In: *Neurocomputing* 199 (2016), pp. 137–143.

[128] M. Lankarany, W. P. Zhu, and M. N. S. Swamy. "Joint estimation of states and parameters of Hodgkin-Huxley neuronal model using Kalman filtering". In: *Neurocomputing* 136 (2014), pp. 289–299.

[129] K. Campbell, L. Staugler, and A. Arnold. "Estimating Time-Varying Applied Current in the Hodgkin-Huxley Model". In: *Applied Sciences* 10 (2020), p. 2.

[130] J. A. M. Valle and A. L. Madureira. "Parameter Identification Problem in the Hodgkin-Huxley Model". In: *Neural Computation* 34 (2022), pp. 939–970.

[131] S J Schiff. *Neural Control Engineering: The Emerging Intersection Between Control Theory and Neuroscience*. Computational neuroscience. Cambridge, MA: MIT Press, 2012, p. 361.

[132] E. M. Izhikevich. "Simple Model of Spiking Neurons". In: *IEEE Trans. Neural Net.* 14 (2003), p. 1569.

[133] E. M. Izhikevich. *Dynamical Systems in Neuroscience*. MIT Press, 2007.

[134] Rodrigo A. García et al. "Small-worldness favours network inference in synthetic neural networks". In: *Scientific Reports* 10 (2020), p. 2296.

[135] E.A. Wan and R. Van Der Merwe. "The unscented Kalman filter for nonlinear estimation". In: *Proceedings of the IEEE 2000 Adaptive Systems for Signal Processing, Communications, and Control Symposium (Cat. No.00EX373)*. 2000, p. 153.

[136] J. Collens et al. "Dynamics and bifurcations in multistable 3-cell neural networks". In: *Chaos* 30 (2020), p. 072101.

[137] R. Labbe. *FilterPy*. https://filterpy.readthedocs.io/en/latest/index.html. Accessed: 10-10-2023. 2015.

[138] T. Fawcett. "An introduction to ROC analysis". In: *Pattern Recognition Letters* 27.8 (2006), pp. 861–874.

[139] P. Holme and J. Saramäki. "Temporal networks". In: *Physics Reports* 519 (2012), p. 97.

[140] A. Citri and R. Malenka. "Synaptic plasticity: multiple forms, functions, and mechanisms". In: *Neuropsychopharmacol* 33 (2008), p. 18.

[141] R. Cestnik and M Rosenblum. "Reconstructing networks of pulse-coupled oscillators from spike trains". In: *Phys. Rev. E* 96 (2017), p. 012209.

[142] R. P. Aristides et al. "Parameter and coupling estimation in small groups of Izhikevich's neurons". In: *Chaos* 33 (2023), p. 043123.

[143] V. P. Vera-Ávila et al. "Experimental datasets of net- works of nonlinear oscillators: Structure and dynamics during the path to synchronization". In: *Data Brief* (28 2020), p. 105012.

[144] M. V. Ivanchenko et al. "Phase synchronization in ensembles of bursting oscillators". In: *Phys. Rev. Lett.* 93 (13 2004), p. 134101.

[145] S. Lloyd. "Least squares quantization in PCM". In: *IEEE Transactions on Information Theory* 28.2 (1982), pp. 129–137.

[146] F. Pedregosa et al. "Scikit-learn: Machine Learning in Python". In: *Journal of Machine Learning Research* 12 (2011), pp. 2825–2830.

[147] C. J. Van Rijsbergen. *Information Retrieval*. Butterworths, London, 1979.

[148] H. Kantz and T. Schreiber. *Nonlinear Time Series Analysis*. Cambridge University Press, 1997.

[149] J. K. Uhlmann. *Simultaneous map building and localization for real time applications*. Transfer thesis. University of Oxford, 1994.

[150] Nicolás Rubido and Cristina Masoller. "Impact of lag information on network inference". In: *The European Physical Journal Special Topics* 227 (2018), pp. 1243–1250.

Research Activites

Publications covered in this thesis

- Master Stability Functions for Networks of Izhikevich Neurons
  R. P. Aristides and Cerdeira, H. A.
  2022 *under revision in* Physical Review E

- Parameter and Coupling Estimation in Small Networks of Izhikevich Neurons
  R. P. Aristides, A. J. Pons, H. A. Cerdeira, C. Masoller, and G. Tirabassi
  2023 Chaos, Volume 33, Issue 4

- Inferring the Connectivity of Coupled Oscillators from Event Timing Analysis
  R. P. Aristides, H. A. Cerdeira, C. Masoller, and G. Tirabassi
  2023 *submitted to* Chaos, Solitons and Fractals

Talks and Posters

- ENREDANDO - Escuela Iberoamericana y Workshop de redes y sistemas complejos
  Master Stability Functions for Networks of Izhikevich Neurons
  Universidad del Pacífico, Lima, Peru
  July 18 - 22, 2022

- X COMPLEXITAT Day
  Parameter and Coupling Estimation in Small Networks of Izhikevich Neurons
  La Lleialtat Santsenca, Barcelona, Spain
  December 4 - 8, 2023

- Perspectives in Nonlinear Dynamics - PNLD 2023
  Master Stability Functions for Networks of Izhikevich Neurons
  IIT - Madras, Chennai, India
  December 4 - 8, 2023

Secondments

- Universitat Politècnica de Catalunya · Barcelona Tech
  Terrassa, Barcelona, Spain
  September, 2022-2023
  Prof. Cristina Masoller

Schools and workshops

- Second School on Data Science and Machine Learning
  Scientific Computing Center - NCC - UNESP, São Paulo
  December 4 - 8, 2023

- Neuromatch Academy - Online
  https://academy.neuromatch.io/
  July 13-31, 2020

- VIII Latin American School on Computational Neuroscience
  NeuroMat - USP, São Paulo
  January 6 – 31, 2020

Outreach activites

- Curso de Inverno ICTP-SAIFR para Jovens Físicos
  Introdução ao Python com física
  https://outreach.ictp-saifr.org/curso-de-inverno-2022/
  Instituto de Física Teórica - UNESP, São Paulo
  July 8-12, 2022
  Monitor

- ICTP-SAIFR Complex Systems & Statistical Mechanics Webinars
  Instituto de Física Teórica - UNESP, São Paulo
  https://ictp-saifr-cssm.github.io/
  2021 - 2022
  Organizer

- Congresso Paulo Leal Ferreira
  Instituto de Física Teórica - UNESP, São Paulo
  http://professores.ift.unesp.br/congressoPauloLealFerreira/
  October 26-30, 2020
  Organizer

In the end, lies the beginning.